

**Application of Microfibrous Materials in Air Filtration  
for Improving Indoor Air Quality**

by

Yanli Chen

A dissertation submitted to the Graduate Faculty of  
Auburn University  
in partial fulfillment of the  
requirements for the Degree of  
Doctor of Philosophy

Auburn, Alabama  
August 4, 2012

Keywords: microfibrous entrapped sorbent/catalyst materials,  
initial pressure drop, energy efficiency, dirt loading capacity

Copyright 2012 by Yanli Chen

Approved by

Bruce J. Tatarchuk, Chair, Professor of Chemical Engineering  
Steve R. Duke, Associate Professor of Chemical Engineering  
Mario R. Eden, Professor of Chemical Engineering  
Daniel Harris, Associate Professor of Mechanical Engineering

## Abstract

The growing emphasis on indoor air quality has resulted in the need for more stringent air filtration requirements in heating, ventilation, and air conditioning (HVAC) systems. The typical filtration system consists of a pre-filter for removing coarse particles, a high-efficiency particulate air (HEPA) filter for removing fine particles, and a separate adsorptive system for removing molecular contaminants as necessary. However, the design of current filtration systems has two major drawbacks: the more space requirement caused by three filtration units and the high energy consumption.

The studies described in this dissertation focused primarily on the development of an innovative dual-functional filtration unit that can simultaneously remove both particulate and molecular contaminants with significantly low energy cost. The dual-functional filtration unit used a class of special filter media known as microfibrous materials (MFM) that are made of sorbent/catalyst particles immobilized within sinter-locked three-dimensional matrices of microfibers, and employed a special filter packing design known as multi-element structured arrays (MESA).

The studies of the design and optimization of pleated MFM filters and MFM MESA units were conducted by applying two previously developed semi-empirical pressure drop models. The results demonstrated that the design parameters have dramatic impact upon initial pressure drop across single MFM pleated filters and MFM MESA units. A comparison in a performance index of carbon loading capacity divided by initial pressure drop at 500 fpm between the optimal MFM MESA unit and a commercially available honeycomb carbon filter

(HCF) has revealed a substantial improvement of the optimal MFM MESA unit. In addition, the experimental results on single HCF, V-shaped HCF MESA unit and W-shaped HCF MESA unit further confirmed the significant benefits of the MESA design. Therefore, it can be used as a platform for commercially available filters with high resistance.

The impact of design parameters on the initial pressure drop across various MESA units that contained commercially available pleated filters for particle removal was experimentally investigated. A comparison of energy consumption between a single pleated filter and a V-shaped MESA unit indicated that the MESA design has the great potential for increasing the energy efficiency and saving the cost in HVAC systems.

To better understand the dust loading behavior for extending the filter service life, the pressure drop evolution of pleated filters subjected to polydiserpsed particles was studied. An empirical model was proposed to predict the pressure drop of pleated filter during the dust loading process. The agreement between the dust loading experimental results and the model results demonstrated that the developed empirical model can accurately predict the pressure drop during the dust loading process. The present studies provided insights into novel approaches for improving and enhancing the filtration performance of future media and filter designs.

## Acknowledgments

First of all, I would like to express my sincerest gratitude to my research advisor, Dr. Bruce J. Tatarchuk, for his guidance and support during this research. His unique research perspective and tremendous knowledge has definitely enriched my learning experience during my time at Auburn University. I would like to acknowledge the US Army Tank Automotive Research, Development and Engineering Center (TARDEC) for providing financial support for the research presented in this dissertation. I would like to thank Dr. Steve R. Duke, Dr. Mario R. Eden and Dr. Daniel Harris for their time and effort by serving as committee members; their constructive suggestions have been very helpful. I am grateful to Dr. Dong-Joo Lim for serving as the university reader for this dissertation.

I would like to thank Mr. Troy Barron for his help and efforts during the reconstruction of the ASHRAE 52.2 standard filter test rig in the new lab. I am thankful to Mr. Ron Putt for his valuable suggestions and hands-on help in the new lab. I would like to thank all of current and past members of the Center for Microfibrous Materials Manufacturing (CM<sup>3</sup>) for making many helpful and insightful discussions. In particular, I would like to acknowledge Dr. Ryan Sothen for his lab training and research guidance.

I would like to express my deep appreciation to the following faculty and staff members for their assistance with some academic and non-academic related issues: Dr. Donald Cahela, Dr. Wenhua Zhu, Mr. Dwight Cahela, Ms. Kimberly Dennis, Ms. Sue Ellen Abner, Ms. Karen Cochran and Mr. Brian Scweiker.

I have special thanks for my family. My parents Peiwen Chen and Ailan Song have given me unconditional love and support throughout my life. My gradation will be bitter sweet, because my father cannot be here to share this special event. My big “little” sister Yanzheng Chen has encouraged me to be the trail blazer; I am the first person in my family tree to obtain a graduate degree. I wish to thank my husband Heping Liu, for his love and support to make this research complete. The last person is my lovely daughter Lucy Jiayun Liu; through her unconditional love she has encouraged me to be a strong mother.

Last, but by no means least, I wish to thank some dear friends. I would like to thank my friend, Dr. Shirlaine Koh, for her consistent encouragement. In addition, I would like to thank Dr. Fred Strickland and Mrs. Sharyn Stickland for making my stay in Auburn feel like a home.

## Table of Contents

Abstract .....	ii
Acknowledgments.....	iv
List of Tables .....	xi
List of Figures .....	xiii
Nomenclature .....	xvii
Chapter 1 Introduction .....	1
1.1 Motivation .....	1
1.2 Microfibrous Sorbent Supported Media (MSSM) .....	2
1.3 Objectives.....	5
Chapter 2 Literature Review .....	7
2.1 Indoor Air Pollution and Its Health Effect.....	7
2.1.1 Particulate matter.....	9
2.1.2 Carbon dioxide .....	11
2.1.3 Carbon monoxide .....	12
2.1.4 Nitrogen dioxide.....	13
2.1.5 Sulfur dioxide.....	13
2.1.6 Radon .....	14
2.1.7 Formaldehyde.....	15
2.1.8 Volatile organic compounds (VOCs).....	16
2.1.9 Ozone .....	18

2.1.10 Indoor biological pollutants .....	19
2.1.11 Sick building syndrome (SBS) .....	21
2.2 Particulate Air Filtration .....	23
2.2.1 Particulate air filters .....	24
2.2.2 Mechanisms for particulate air filtration .....	25
2.2.3 Standards for determining and measuring particulate filter performance .....	29
2.3 Molecular Filtration .....	32
2.3.1 Sorbents for molecular filtration .....	32
2.3.2 Mechanisms for gaseous contaminant removal .....	36
Chapter 3 Experimental Apparatus and Test Procedure .....	41
3.1 Introduction .....	41
3.2 Experimental Set-up .....	42
3.2.1 Small-scale media test rig .....	43
3.2.2 Full-scale filter test rig .....	44
3.3 Test Procedure .....	52
3.3.1 Initial pressure drop test .....	52
3.3.2 Removal efficiency test .....	53
3.3.3 Dirt loading test .....	54
Chapter 4 Fundamental Design of Microfibrous Materials as Pleated Filter Media .....	57
4.1 Introduction .....	57
4.2 Model Description .....	58
4.3 Media Preparation .....	61
4.4 Media Thickness and Constants .....	64

4.5 Application of Model for MFM Filters Design .....	68
4.5.1 Effect of pleat number .....	68
4.5.2 Effect of filter depth .....	73
4.5.3 Effect of media thickness .....	77
4.5.4 Effect of media constants .....	80
4.6 Conclusions .....	82
Chapter 5 Influence of Design Parameters on Filtration Performance of MESA.....	83
5.1 Introduction .....	83
5.2 Material .....	85
5.2.1 Construction of MESA unit.....	85
5.2.2 Tested filter information.....	86
5.3 Experimental Set-up and Test Procedure.....	87
5.4 Results and Discussion.....	87
5.4.1 Comparison of MESA unit and single filter.....	87
5.4.2 Effect of element alignment within a MESA .....	89
5.4.3 Effect of element count within a MESA .....	90
5.4.4 Effect of element depth within a MESA .....	93
5.4.5 Effect of pleat numbers within a MESA .....	95
5.4.6 Effect of fairings within a MESA .....	98
5.4.7 Estimations of useful lifetime and power consumption .....	100
5.6 Conclusions .....	102
Chapter 6 Pressure Drop Evolution of Pleated Filter During Dirt Loading Process .....	104
6. 1 Introduction.....	104



6.2 Previous Research .....	105
6.2.1 Davies .....	106
6.2.2 Bergman et al. ....	106
6.2.3 Kanaoka and Hiragi.....	107
6.2.4 Novick et al. ....	107
6.2.5 Thomas et al. ....	109
6.2.6 Song et al. ....	109
6.3 Experimental Methods .....	111
6.3.1 Testing protocol for flat media samples.....	111
6.3.2 Testing protocol for full-size filters .....	112
6.4 Results and Discussion.....	113
6.4.1 Dirt loading capacity of full-size filters .....	113
6.4.2 Model development and verification.....	117
6.4.3 Effect of loading velocity.....	123
6.4.4 Enhanced removal efficiencies.....	126
6.4.5 Layer penetration.....	127
6.4.6 Variations in deposition patterns.....	129
6.5 Conclusions .....	132
Chapter 7 Design of Microfibrous Materials in Multi-Element Structured Arrays.....	134
7.1 Introduction .....	134
7.2 Model Description.....	135
7.3 Results and Discussion.....	138
7.3.1 Utilization of MESA pressure drop model.....	138

7.3.2 Optimization of MFM MESA units regarding to initial pressure drop.....	140
7.3.3 Carbon loading capacity of MFM MESA units .....	142
7.3.4 Comparison of packed bed and MFM MESA units.....	144
7.4 Conclusions .....	147
Chapter 8 Conclusions and Future Work.....	149
8.1 Conclusions .....	149
8.2 Recommendations for Future Work.....	151
8.2.1 Lab tests and field tests of MFM filtration units .....	151
8.2.2 Development of comprehensive filtration system.....	151
8.2.3 CFD Analysis .....	153
References.....	154

## List of Tables

Table 2.1	Major indoor pollutants and emission sources.....	8
Table 2.2	Selected indoor air pollutants and their potential health effects .....	10
Table 2.3	Sources of common volatile organic compounds in indoor air.....	18
Table 2.4	Diseases and disease syndromes associated with exposure to bacteria and fungi ..	20
Table 2.5	ASHRAE Standard 52.2 MERV parameters and application guidelines .....	31
Table 2.6	Gases and respective removal media .....	33
Table 3.1	Average velocity and coefficient of variation within the test rig .....	49
Table 4.1	Composition of three MFM samples .....	64
Table 4.2	Summary of MFM media characterization .....	67
Table 4.3	Critical parameters of filters employed.....	70
Table 4.4	Optimal pleat numbers and corresponding filtration area for MFM No. 1 pleated filters with different depth .....	73
Table 4.5	Summary of normal and treated MFM samples characterization .....	77
Table 4.6	Model predicted optimal pleat numbers different MFM filters at 500 fpm.....	79
Table 5.1	Critical parameters of filters utilized .....	87
Table 5.2	Initial pressure drop at 500 fpm .....	88
Table 5.3	Estimated lifetime costs for single filter, V-shaped MESA unit .....	102
Table 6.1	Dirt loading results of full-scale filters .....	115
Table 6.2	Dirt loading characterization of different MERV rank filters .....	121
Table 7.1	Characteristic parameters of MFM No.1 .....	138

Table 7.2	Comparison of initial pressure drop at 500 fpm of different MFM filtration units .....	140
Table 7.3	Optimal pleat count of different MFM filtration units.....	142
Table 7.4	Effect of filtration unit structures on carbon loading capacity.....	144
Table 7.5	Comparison of various configurations of honeycomb carbon filter .....	146
Table 7.6	Comparison of MFM MESA units and HCF MESA units.....	147

## List of Figures

Figure 1.1	Two-inch sorbent panels .....	2
Figure 1.2	SEM image of microfibrus entrapped catalyst (MFEC).....	3
Figure 2.1	Common air contaminants and their relative sizes.....	25
Figure 2.2	Sieving mechanism for particle capture .....	26
Figure 2.3	Inertial impaction mechanism for particle capture .....	26
Figure 2.4	Interception mechanism for particle capture .....	27
Figure 2.5	Diffusion mechanism for particle capture .....	27
Figure 2.6	Electrostatic attraction mechanism for particle capture .....	28
Figure 2.7	Fractional collection efficiency versus particle diameter for a mechanical filter .....	29
Figure 2.8	Scanning electron microscope image of activated carbon pores.....	34
Figure 3.1	Illustration of pressure drop measurement .....	41
Figure 3.2	Illustration of removal efficiency measurement.....	42
Figure 3.3	Schematic of small-scale filter media test rig.....	44
Figure 3.4	Picture of small-scale media test rig.....	44
Figure 3.5	Schematic of full-scale filter test rig .....	45
Figure 3.6	Blower and four-tap configuration .....	46
Figure 3.7	Schematic of TSI 8108 large particle generator .....	48
Figure 3.8	ASHRAE dust size distribution.....	48
Figure 3.9	Alignment and clamping system .....	50

Figure 3.10	Upstream picture of filter test rig .....	51
Figure 3.11	Downstream picture of filter test rig.....	51
Figure 3.12	Picture of Solair 3100 <sup>+</sup> particle counter .....	54
Figure 3.13	Loading tray with leveling tool .....	55
Figure 4.1	Typical “U” pleating curve .....	58
Figure 4.2	Proposed flow pattern.....	59
Figure 4.3	Illustration of filter dimensions .....	61
Figure 4.4	Illustration of pleat dimensions .....	61
Figure 4.5	Picture of 8" × 8" sheet making equipment in our lab.....	63
Figure 4.6	Picture of MFM media sample No. 2.....	63
Figure 4.7	Picture of thickness measurement equipment .....	66
Figure 4.8	General schematic of media test rig .....	66
Figure 4.9	Picture of media test set-up .....	67
Figure 4.10	Media resistance curve for three MFM samples .....	68
Figure 4.11	Pleating curves of commercial MERV 8 filters with different depth .....	71
Figure 4.12	Effect of pleat numbers on initial pressured drop for MFM No.1 pleated filters .....	<b>Error! Bookmark not defined.</b>
Figure 4.13	Optimal pleat numbers for MFM No.1 pleated filters with different depth.....	73
Figure 4.14	Effect of filter depth on initial pressure drop for MFM No.1 pleated filters .....	<b>Error! Bookmark not defined.</b>
Figure 4.15	Initial pressure drop of MFM No. 1 pleated filters with different depth at 500 fpm.....	76
Figure 4.16	Comparison of pleat pitch of 1", 2" and 4" filters.....	76
Figure 4.17	Effect of media thickness on initial pressure drop for MFM filters .....	79
Figure 4.18	Optimal pleat numbers for filters with different media thickness at 500 fpm.....	80

Figure 4.19	Effect of media constants on initial pressure drop for MFM filters .....	81
Figure 5.1	Schematic of multi-element structured array housing.....	86
Figure 5.2	Comparison of initial pressure drop across single filter, V-shaped MESA and W-shaped MESA .....	88
Figure 5.3	Horizontally-oriented (left) & vertically-oriented (right) banks .....	89
Figure 5.4	Effect of pleat alignment on initial pressure drop for V-shaped MESA.....	90
Figure 5.5	Different MESA configurations .....	92
Figure 5.6	Effect of element count on initial pressure drop for 2 inch deep MESA units.....	93
Figure 5.7	Effect of element depth on contribution .....	94
Figure 5.8	Effect of element depth on initial pressure drop for V-shaped MESA.....	95
Figure 5.9	Pleating curves for 1, 2 and 4 inch deep filters (experimental results) .....	96
Figure 5.10	Initial pressure drop curve for single filters and W-shaped MESA units with different pleat numbers.....	97
Figure 5.11	Pictures of the tested MESA unit with fairings .....	99
Figure 5.12	Effect of fairings on initial pressure drop of WV-shaped MESA unit.....	100
Figure 6.1	A typical loading curve.....	105
Figure 6.2	Effect of pleat count on initial pressure drop and overall dirt loading of Set A and C filters .....	116
Figure 6.3	Effect of pleat count on initial pressure drop and overall dirt loading of Set B and D filters .....	117
Figure 6.4	Dirt loading curve of MERV 8 pleated filter .....	118
Figure 6.5	Dirt loading curve of MERV 11 pleated filter .....	119
Figure 6.6	Dirt loading curve of MERV 13 pleated filter .....	11920
Figure 6.7	Comparison of experimental and model results for MERV 8 24" × 24" × 1" filter with 20 pleats.....	122
Figure 6.8	Comparison of experimental and model results for MERV 8 24" × 24" × 4" filter with 10 pleats.....	123

Figure 6.9	Effect of loading velocity for media type 1 .....	125
Figure 6.10	Dirt penetration and aging rates of model filter media.....	128
Figure 6.11	SEM image of the top layer of model media loaded at different face velocity after the 2 <sup>nd</sup> dirt load.....	131
Figure 6.12	SEM image of the top layer of model media loaded at different face velocity after the 6 <sup>th</sup> dirt load .....	131
Figure 6.13	SEM image of the top layer of model media loaded at different face velocity after the final dirt load .....	131
Figure 7.1	General schematic of a MESA unit .....	135
Figure 7.2	Proposed flow pattern.....	136
Figure 7.3	Comparison of initial pressure drop of single MFM filter and various MESA configurations.....	139
Figure 7.4	Comparison of initial pressure drop of different MFM filtration units .....	141
Figure 7.5	Effect of filtration unit structures on carbon loading capacity .....	143
Figure 7.7	Picture of 1" deep commercial honeycomb carbon filter .....	145
Figure 7.8	Comparison of initial pressure drop of various configurations of honeycomb carbon filter .....	146
Figure 8.1	Schematic of comprehensive filtration system.....	152



## Nomenclature

$a_f$	Packing density of the filter media (volume occupied by fibers of the total filter media volume), dimensionless
$a_p$	Packing density of the loaded particles (volume occupied by loaded particles of the total filter media volume), dimensionless
$\mu$	Viscosity, lb/ft/s [cP]
$\rho_p$	Particle density, lb/ft <sup>3</sup> [g/m <sup>3</sup> ]
$m$	Dust load in a unit filter volume, lb/ft <sup>3</sup> [g/m <sup>3</sup> ]
$t$	Time, s
$x$	Depth from filter inlet, ft [m]
$A$	Filtration area, ft <sup>2</sup> [m <sup>2</sup> ]
$C_c$	Cunningham correction factor, dimensionless
$C_D$	Drag coefficient
$D_f$	Fiber diameter, ft [m]
$D_p$	Particle diameter, ft [m]
$F$	Form drag coefficient, dimensionless
$K$	Arbitrary constant, dimensionless
$L_1$	Dirt loading coefficient 1, "H <sub>2</sub> O (ft• min/g) <sup>3</sup> [Pa (m• min/g) <sup>3</sup> ]
$L_2$	Dirt loading coefficient 2, "H <sub>2</sub> O (ft• min/g) <sup>2</sup> [Pa (m• min/g) <sup>3</sup> ]
$L_3$	Dirt loading coefficient 3, "H <sub>2</sub> O (ft• min/g) [Pa (m• min/g) <sup>3</sup> ]
$M$	Mass loaded, g
$M_C$	Total mass challenged, g
$\Delta P$	Pressure drop, "H <sub>2</sub> O [Pa]
$\Delta P_0$	Initial pressure drop, "H <sub>2</sub> O [Pa]
$\Delta P_F$	End-of-life pressure drop, "H <sub>2</sub> O [Pa]
$\Delta P_W$	Pressure drop window, "H <sub>2</sub> O [Pa]
$R$	Glass fibers mean radius, ft [m]
$E$	Removal efficiency, %
$St$	Stokes number, dimensionless
$V$	Velocity, ft/s [m/s]
$V_C$	Ratio of particle packing density and fiber packing density, dimensionless
$V_F$	Face velocity, ft/s [m/s]
$V_M$	Media velocity, ft/s [m/s]
$Z$	Media thickness, ft [m]

## Subscripts

m dirt loaded  
f fiber  
P particle  
J the layer J

# Chapter 1 Introduction

## 1.1 Motivation

With the increase of health problems related to indoor air pollutants, indoor air quality has become a great concern over the past decade. Growing emphasis on indoor air quality has resulted in the need for more stringent air filtration requirements in heating, ventilation, and air conditioning (HVAC) systems. The standard configuration for a building is a pre or dust filter followed by a high efficiency particulate air (HEPA) filter. The dust filter would remove coarser particles from the air flow. The HEPA filter would remove 99.97% of 0.3 $\mu$ m diameter particulates, the most penetrating particle size.

However, gas-phase contaminants such as carbon dioxide (CO<sub>2</sub>), carbon monoxide (CO), formaldehyde (HCHO), radon (Rn), acid gases, or volatile organic compounds (VOCs) cannot be removed by HEPA filters. Therefore, a separate adsorptive system is in a need for many high-threat buildings, such as hospitals, clean rooms, semiconductor environments, and chemical factories. Carbon adsorbent filters are commonly used for this purpose. Figure 1.1 shows a two-inch sorbent panel from Camfil Farr, Inc. This filter can be used to control odors or limit VOC exposure created by contaminants. However, high pressured drop of the adsorbent filters can result in large energy consumption of HAVAC systems. Novel housing or packaging designs have been shown as an effective way to increase available filtration area and to reduce pressure drops (Sothorn, 2009).

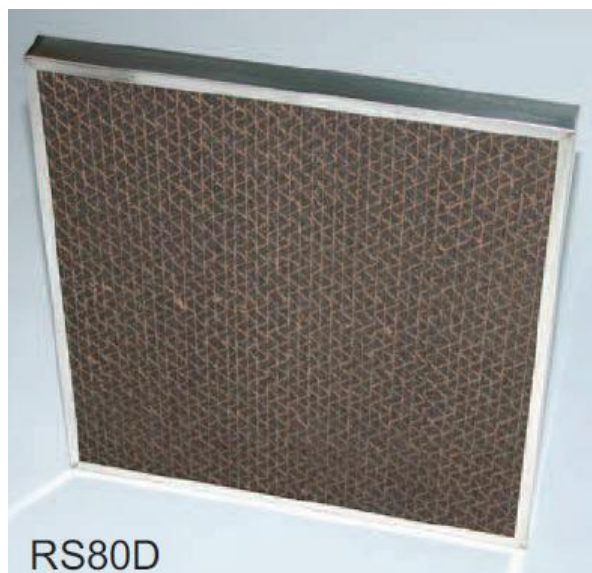


Figure 1.1 Two-inch sorbent panels (Camfil Farr, Inc.)

As a dual-functional material, microfibrous media has the potential to remove both particulate matters and airborne molecular contaminants simultaneously. For example, Kennedy (2007) and Queen (2005) employed microfibrous materials in cathode air filters and fire masks for the successful removal of VOCs. Kalluri (2008) investigated the ability of microfibrous media to remove ozone from a polluted air stream, and showed that microfibrous media with a higher pleat factor exceeds the performance of the monoliths and packed beds. In addition to the great benefit of removing undesirable materials, Karanjikar (2005) successfully achieved catalytic oxidation of carbon monoxide to the more benign carbon dioxide through the use of microfibrous media.

## **1.2 Microfibrous Sorbent Supported Media (MSSM)**

Microfibrous media was developed in 1987 for chemical and electrochemical applications by the Department of Chemical Engineering and the Space Power Institute at Auburn University. This media is manufactured through a traditional wet lay paper manufacturing process. Micron-diameter fibers, pre-pulped cellulose, and sorbent/catalyst

particles are combined in an aqueous solution and dispersed onto a wire mesh to form a sheet. The resulting composite sheet is subsequently heated in a continuous hydrogen-sintering furnace at about 1000 °C, which removes the cellulose and causes the fibers to sinter-bond at their junctures for a robust structure of up to 98% void volume (Harris et al., 2001). Microfibrous materials can be constructed with metal, ceramic, or polymer fibers depending upon the requirements of the reaction/adsorption process under consideration. When sorbent particles are incorporated into a sheet, the resulting composite structures are known as Microfibrous Sorbent-Supported Media (MSSM) (Harris et al., 2001). Figure 1.2 is a micrograph image of sorbent particles (180-210  $\mu\text{m}$  aluminum oxide particles) entrapped in 8  $\mu\text{m}$  nickel fibers. As shown in Figure 1.2, the sorbent or catalyst particles are held in place by a three-dimensional sinter-locked network of fibers with diameters typically ranging between two and twenty microns. High surface area catalyst/sorbent particles between 50 and 300  $\mu\text{m}$  can be embedded. However, support particles with average diameters between 100 to 200  $\mu\text{m}$  are preferred (Murrell et al., 2000).

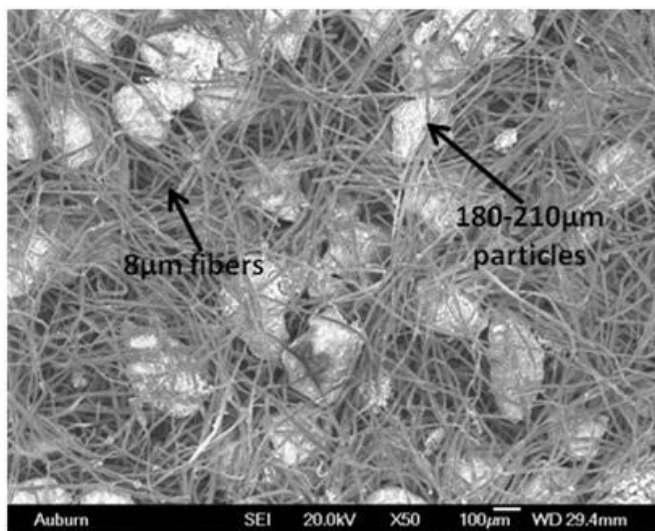


Figure 1.2 SEM image of microfibrous entrapped catalyst (MFEC) (180-210  $\mu\text{m}$  aluminum oxide particles entrapped in 8  $\mu\text{m}$  nickel fibers)

The ability to be wet-laid and entrap microscopic particles of microfibrinous media enhances its utility in adsorption and catalytic processes. The wet lay process allows for customizable void volumes ranging from 30% to 98% (Marrion et al., 1994). The high void volume of the MSSM can facilitate intralayer heat and mass transfer (Harris et al., 2001). The extremely small particle size in the MSSM allows molecules to diffuse into a sorbent's innermost structure at a higher rate leading to greater utilization, smaller mass transfer zones, and shorter critical bed depths compared to packed beds and monoliths (Harris et al., 2001; Kalluri, 2008). In turn, a smaller quantity of costly catalytic material is needed to achieve the same performance. The wet lay process creates a homogeneous material that reduces channeling effects typically associated with the use of sub-millimeter particulate supports (Kalluri, 2008). This assists with preventing the premature breakthrough of the pollutant through the filter system.

Although MSSM possesses high contacting efficiency and material utilization, there are two drawbacks as filtration media. The first drawback is its large pressure drop. The second drawback is its relatively low loading capacity of adsorbent material. The large resistance of the media is the result of the combined effects of air flow through the porous structure and of drag forces present on the embedded particles. Equation 1.1 illustrates that the pressure drop of a media is directly proportional to the thickness (h) and the packing density (c), and it possesses an inverse quadratic relationship in regard to the fiber diameter ( $D_f$ ) (Brown, 1993).

$$\Delta P = 4\eta chV / D_f^2 \xi \quad (1.1)$$

When smaller fibers and particles are employed in making the MSSM, the pressure drop should be very high. The capacity of the media remains low due to the thinness of the material and the low concentration of support within the matrix. Although the thickness and the support

concentration could be adjusted to increase the capacity, each would cause the pressure drop of the media to increase as described in Eq. 1.1.

A higher pressure drop or resistance is undesirable since this would increase the energy consumption of a filtration system (Arnold et al., 2005). Lower loading capacity of adsorbent material is also detrimental since it would shorten the life-time of a filter and as a result, the operational cost would increase. The higher pressure drop and the lower loading capacity issues could be solved by using an innovative housing design, multi-element structured arrays (MESAs) (Sothen, 2009).

### **1.3 Objectives**

The main objective of this research is to systematically investigate the filtration characteristics of microfibrous media as dual-functioning filter media, such as pressure drop, removal efficiency, loading capacity, and breakthrough capacity. The investigation will use both experimental and model simulation methods.

MESA design will be studied for a better understanding of the effects of varying design parameters (such as element number, element depth, pleat numbers, element alignment and fairings application) on filtration performance.

Sothen et al. (2008, 2009) had successfully developed semi-empirical pressure drop models for a single pleated filter and for a MESA unit. However, these models are only for clean filters and do not account for the increase in resistance due to the dirt loading sustained during the lifetime of a filter. Dirt capture significantly increases the resistance of a filter by lowering the permeability of the media. Thus any attempt to maximize the useful lifetime or estimate the energy consumption of a filter must account for the impact of dirt loading. In this

work, pressure drop models during the dirt loading process for a single pleated filter will be developed in order to maximize the useful life time.

It is expected that this work can bring some insights to improve air filtration system design with enhanced filtration performance and energy efficiency.



## **Chapter 2 Literature Review**

### **2.1 Indoor Air Pollution and Its Health Effect**

During the last two decades there has been increasing concern over indoor air quality and the health effect of poor indoor air quality (Jones, 1999; Bruce et al., 2000; Brunekreef and Holgate, 2002; Zhang and Smith, 2003; Craig et al., 2008). Acceptable indoor air quality (IAQ) is defined as “air in which there are no known contaminants at harmful concentrations as determined by cognizant authorities and with which a substantial majority (80 percent or more) of the people exposed do not express dissatisfaction” (ASHRAE Standard 62-1989). With a much greater use of synthetic building materials, indoor pollutants can emanate from a range of sources. The foremost indoor air pollutants are carbon dioxide, carbon monoxide, nitrogen oxides, ozone, volatile organic compounds (VOCs), and particulate matter less than 10 microns in diameter (Liu and Lipták, 2000). The major indoor pollutants and their emission sources are summarized in Table 2.1 (Jones, 1999). As reflected in this table, the sources of indoor pollutants may be broadly classified as activities of building occupants, as biological sources, as the combustion of products for heating or fuel, and as the emissions from building materials. Infiltration from outside of a building either through water, air, or soil, can be a significant source for some contaminants.

Air pollution is pervasive throughout the world, and represents one of the most widespread environmental threats to the population’s health. In recent years, the United States

Environmental Protection Agency (USEPA) and its Science Advisory Board (SAB) have performed comparative risk studies that have consistently ranked indoor air

Table 2.1 Major indoor pollutants and emission sources (Jones, 1999)

<b>Pollutant</b>	<b>Major emission sources</b>
Allergens	House dust, domestic animals, insects
Asbestos	Fire retardant, materials, insulation
Carbon dioxide	Metabolic activity, combustion activities, motor vehicles in garages
Carbon monoxide	Fuel burning, boilers, stoves, gas or kerosene heaters, tobacco smoke
Formaldehyde	Particleboard, insulation, furnishings
Micro-organisms	People, animals, plants, air conditioning systems
Nitrogen dioxide	Outdoor air, fuel burning, motor vehicles in garages
Organic substances	Adhesives, solvents, building materials, volatilization, combustion, paints, tobacco smoke
Ozone	Photochemical reactions
Particles	Re-suspension, tobacco smoke
Polycyclic aromatic hydrocarbons	Fuel combustion, tobacco smoke
Pollens	Outdoor air, trees, grass, weeds, plants
Radon	Soil, building construction materials (concrete, stone)
Fungal spores	Soil, plants, foodstuffs, internal surfaces
Sulfur dioxide	Outdoor air, fuel combustion

pollution among the top five environmental risks to public health (Zhang, 2005). Bruce et al. (2000) pointed out that indoor air pollution is a major global public health threat that will require greatly increased efforts in the areas of research and policy-making. Numerous other studies have reported on the association between exposure to various indoor air pollutants and related diseases (Guneser et al., 1994; Maier et al., 1997; Ritz and Yu, 1999; Jones, 1999; Bruce et al., 2000; Brunekreef and Holgate, 2002; Davidson et al., 2005; Craig et al., 2008). Table 2.2 summarizes selected indoor air pollutants and their potential health effects. As shown in this table, numerous serious diseases have been proven to be related to poor indoor air quality, such as respiratory illnesses, cancers, tuberculosis, poor perinatal outcomes (mainly low birth

weight), and eye diseases. In the following sections, we will discuss in greater detail certain key indoor air pollutants and their health effects.

### **2.1.1 Particulate matter**

Particulate matter is small particles consisting of solid or liquid droplets suspended in the air. Primary particles are emitted directly from a source whereas secondary particles are formed from gaseous emissions. Both natural and anthropogenic (human activities) sources are responsible for particle emission. For example, a natural emission could be gaseous sulfur from volcanoes or from decaying vegetation which can form secondary sulfate particles in the atmosphere. Anthropogenic sources could come from mining, oil refining, manufacturing, or fossil fuel combustion; examples are coal and oil acids, element carbon, heavy metals, and organic species (Davidson et al., 2005). According to the studies conducted by USEPA, the largest source category averaged over the entire United States (US) for particulate matter emission is utility fuel combustion which is mainly coal burning for electricity production (USEPA, 2004a).

Preliminary studies seem to indicate that regardless of the source of particulate matter, there are risks to human health. Particles with diameters below 10 microns ( $PM_{10}$ ), and particularly those less than 2.5 microns in diameter ( $PM_{2.5}$ ), can penetrate deeply into the lungs and appear to have the greatest potential for damaging health (USEPA, 2004b). The National Ambient Air Quality Standards (NAAQS) of USEPA for 24-hour average  $PM_{10}$  and  $PM_{2.5}$  concentrations are  $150 \mu\text{g}/\text{m}^3$  and  $65 \mu\text{g}/\text{m}^3$ , respectively (USEPA, 2004b).

Table 2.2 Selected indoor air pollutants and their potential health effects  
(Bruce et al, 2000)

<b>Pollutant</b>	<b>Mechanism</b>	<b>Potential health effects</b>
Particles (small particles less than 10 microns, and particularly less than 2.5 microns aerodynamic diameter)	<ul style="list-style-type: none"> <li>• Acute: bronchial irritation, inflammation and increased reactivity</li> <li>• Reduced mucociliary clearance</li> <li>• Reduced macrophage response and reduced local immunity</li> <li>• Fibrotic reaction</li> </ul>	<ul style="list-style-type: none"> <li>• Wheezing, exacerbation of asthma</li> <li>• Respiratory infections</li> <li>• Chronic bronchitis and chronic obstructive pulmonary disease</li> <li>• Exacerbation of chronic obstructive pulmonary disease</li> </ul>
Carbon monoxide	<ul style="list-style-type: none"> <li>• Binding with hemoglobin to produce carboxy hemoglobin, which reduces oxygen delivery to key organs and the developing fetus.</li> </ul>	<ul style="list-style-type: none"> <li>• Low birth weight ( fetal carboxy hemoglobin 2-10% or higher)</li> <li>• Increase in perinatal deaths</li> </ul>
Polycyclic aromatic hydrocarbons	<ul style="list-style-type: none"> <li>• Carcinogenic</li> </ul>	<ul style="list-style-type: none"> <li>• Lung cancer</li> <li>• Cancer of mouth, nasopharynx and larynx</li> </ul>
Nitrogen dioxide	<ul style="list-style-type: none"> <li>• Acute exposure increase bronchial reactivity</li> <li>• Longer term exposure increases susceptibility to bacterial and viral lung infections</li> </ul>	<ul style="list-style-type: none"> <li>• Wheezing and exacerbation of asthma</li> <li>• Respiratory infections</li> <li>• Reduced lung function in Children</li> </ul>
Sulfur dioxide	<ul style="list-style-type: none"> <li>• Acute exposure increases bronchial reactivity</li> <li>• Longer term: difficult to dissociate from effects of particles</li> </ul>	<ul style="list-style-type: none"> <li>• Wheezing and exacerbation of asthma</li> <li>• Exacerbation of chronic obstructive pulmonary disease, cardiovascular disease</li> </ul>
Biomass smoke condensates including polycyclic aromatics and metal ions	<ul style="list-style-type: none"> <li>• Absorption of toxins into lens, leading to oxidative changes</li> </ul>	<ul style="list-style-type: none"> <li>• Cataract</li> </ul>

Inhaled particles may result in airway constriction. There is growing evidence that smoke may be associated with respiratory illness, particularly among vulnerable groups such as children and patients. Koenig et al. (1993) reported that infants exposed to wood smoke were more likely to develop asthma symptoms, and Abbey et al. (1998) observed a reduction in lung function when non-smokers were exposed to high concentrations of indoor particles over a period of 20 years.

### **2.1.2 Carbon dioxide**

Carbon dioxide (CO<sub>2</sub>) is a colorless, odorless gas. Since humans continuously exhale CO<sub>2</sub> as a byproduct of the body's metabolic processes, the primary source of CO<sub>2</sub> in office buildings is the occupants' respiration. In addition, CO<sub>2</sub> is the main combustion product from carbon based (gas, kerosene, and wood or coal) fueled heating appliances (Moriske et al., 1996). Typical indoor CO<sub>2</sub> concentrations range between 700 and 2,000 ppm, but can exceed 3,000 ppm when unvented appliances are used (Arashidani et al., 1996). The American Society of Heating, Refrigerating and Air-Conditioning Engineers, Inc. (ASHRAE) states that "comfort (odor) criteria with respect to human bioeffluents are likely to be satisfied if the ventilation results in indoor CO<sub>2</sub> concentrations less than 700 ppm above the outdoor air concentration. Outdoor CO<sub>2</sub> concentration is regarded as acceptable when in the range between 300 to 500 ppm" (ASHRAE Standard 62-1999).

Carbon dioxide is a simple asphyxiant, and can also act as a respiratory irritant (Maroni et al., 1995). If indoor carbon dioxide levels are more than 1,000 ppm, then people may begin to complain with headaches, fatigue, eye irritation, and throat irritation. When the levels are above 15,000ppm, some people may experience respiratory difficulties. When the levels are above 30,000 ppm, some people may experience headaches, dizziness, and nausea

(Schwarzberg, 1993). Seppänen et al. (1999) reported that about one-half of the 22 sick building syndrome (SBS) symptoms studies found that increased indoor CO<sub>2</sub> levels were positively correlated with a statistically significant increase in the prevalence of one or more SBS symptoms.

### **2.1.3 Carbon monoxide**

Carbon monoxide (CO) is a toxic colorless and odorless gas that appears when combustion is incomplete. Potential indoor sources of CO include carbon based heating systems, carbon based stoves, gas hot water heaters, tobacco smoke, and portable kerosene heaters. Another source of CO is dichloromethane (DCM or methylene chloride), which is used as a solvent for stripping paint, for removing grease, for processing food, for aerosol spray propellant, and for specialized low boiling point uses.

When DCM is inhaled, it is metabolized to form CO. Since the human body does not discharge CO, a person could slowly accumulate a significant dosage even in a well-ventilated room and experience CO poisoning (Gold, 1992). The toxic properties of CO are largely related with its high affinity for oxygen-carrying proteins such as hemoglobin and myoglobin (Coultas and Lambet, 1991) with the result that it has the most toxic acute effect on those organs with high oxygen requirements. CO exposure in levels as low as 35 ppm may cause mild fatigue. Adverse health effects such as headache and dizziness may occur after a two-hour exposure to CO levels as low as 100 ppm (Ritz and Yu, 1999).

The USEPA has published the eight-hour average CO standard to be 9 ppm (USEPA, 1997). In contrast, the CO mean 24-hour level in developing countries' homes using biomass fuels for heating is in the range 2-50 ppm and during cooking the values of 10-500 ppm have been reported (Bruce et al., 2000).

#### **2.1.4 Nitrogen dioxide**

Nitrogen dioxide (NO<sub>2</sub>) is a water-soluble red to brown gas with a pungent acrid odor. It is produced during the incomplete combustion of natural gas or other fuels. Possible indoor sources of NO<sub>2</sub> are associated with the operation of gas appliances, kerosene heaters, and wood burning stoves, as well as tobacco smoke. Additionally, outdoor air can act as an important source for indoor NO<sub>2</sub> pollution in some areas (Chan et al., 1990). As one of the six principal pollutants, the USEPA has set the NAAQS for NO<sub>2</sub> over a 1-hour period as 100 ppb and annual level as 53 ppb (USEPA, 2010a).

Nitrogen dioxide is an oxidizing agent that can be very irritating to the mucous membranes and the lungs (Spengler, 1993). Evidence from experimental research suggests that exposure to NO<sub>2</sub> may increase respiratory infections and thus adversely affect lung function (Frampton et al., 1991). Exposure to NO<sub>2</sub> may act as a trigger for asthma (Jones, 1997). USEPA has reported that short-term NO<sub>2</sub> exposures, ranging from 30 minutes to 24 hours can result in adverse respiratory effects including airway inflammation in healthy people and increased respiratory symptoms in people with asthma (USEPA, 2010a).

#### **2.1.5 Sulfur dioxide**

Sulfur dioxide (SO<sub>2</sub>) is a colorless gas with a strong pungent odor that can be detected at about 0.5 ppm. It is readily soluble in water and can be oxidized within airborne water droplets (Maroni et al., 1995). Sulfur dioxide is produced by the oxidation of sulfur impurities during the burning of coal and other fuels that contain sulfur. Hence, the indoor SO<sub>2</sub> sources include kerosene heaters, coal appliances, gas stoves, and so on. In 2010, USEPA strengthened the primary NAAQS for SO<sub>2</sub> to improve public health protection. Specifically, USEPA replaced the existing annual and 24-hour primary SO<sub>2</sub> standards with a new 1-hour SO<sub>2</sub> standard set at 75

ppb to better protect public health by reducing people's exposure to high short-term ( 5 minutes to 24 hours) concentrations of SO<sub>2</sub> (USEPA, 2010b).

From a health effects viewpoint, two substances are under consideration; the SO<sub>2</sub> itself and the acid aerosols resulting from its oxidation with other compounds in the atmosphere. Those two substances are linked with a number of adverse effects on the respiratory system. Exposure to extreme concentrations of SO<sub>2</sub> and acid aerosols can precipitate an acute reduction in lung functions (Islam and Ulmer, 1979). USEPA reported that scientific evidences show that short-term exposures to SO<sub>2</sub>, ranging from 5 minutes to 24 hours can result in an array of adverse respiratory effects including bronchoconstriction and increased asthma symptoms (USEPA, 2010b). In China where the domestic burning of coal is still widespread, research studies have found that the exposure to SO<sub>2</sub> has impaired lung function and a range of other respiratory symptoms (Qin et al., 1993).

### **2.1.6 Radon**

Radon is an invisible, odorless radioactive gas. It is formed by the breakdown of radium which is produced when uranium decays in the soil and rock. Radon gas enters buildings through cracks, crawlspaces, basement drains, and other openings in foundations or concrete slabs. According to the USEPA, acceptable average indoor levels of radon should be around 1.3 picoCuries per liter (pCi/L) and mitigation is required when the radon levels exceed 4 pCi/L (USEPA, 1996).

Radon itself is inert and causes little damage. However, the progeny, Po-218 and Po-214 are electrically charged and can be inhaled either directly or through their attachment to airborne particles (Cohen, 1998). Once inhaled, they tend to remain in the lungs where they may eventually cause cancer (Polpong and Bovornkitti, 1998). The USEPA has reported that radon



is the second leading cause of lung cancer in the US and the leading cause of lung cancer among non-smokers (USEPA, 1996). In addition to being linked to lung carcinogenesis, radon exposure has also been associated with the development of acute myeloid and acute lymphoblastic leukemia (Jones, 1999).

### **2.1.7 Formaldehyde**

Formaldehyde (HCHO) is a colorless, pungent-smelling gas and is the most widespread aldehyde found in the environment. Sources of formaldehyde in households include building materials, smoking, household products, and the use of un-vented, fuel-burning appliances. Of these, the primary source is widely used building materials, such as particle board, hardwood plywood paneling, medium density fiberboard, resins, furniture, adhesives, carpeting and water-based paints (Jones, 1999; Zhang et al., 2005). Therefore, the concentration of formaldehyde within a given indoor space will be dependent upon the presence of important emission sources. In the US, average concentrations in older homes without urea-formaldehyde foam insulation (UFFI) are generally well below 0.1 ppm. In homes with significant amounts of new pressed wood products, levels can be greater than 0.3 ppm. Recently, a new federal law for regulating formaldehyde emission, the “Formaldehyde Standards for Composite Wood Products Act (FSA),” was signed into law by President Obama on July 7, 2010 to establish limits for formaldehyde emissions from composite wood products.

Adverse health effects from formaldehyde exposure may arise from inhalation or direct contact. When present in the air at concentrations of less than 1 ppm, formaldehyde can cause watery eyes; burning sensations in the eyes, nose and throat; nausea; coughing; chest tightness; wheezing; skin rashes; and allergic reactions (Jones, 1999; Sekine and Nishimura, 2001; Sekine, 2002). High concentrations may trigger attacks in people with asthma. There is conclusive

evidence that formaldehyde can cause cancer in animals (Morgan, 1997; Litto, 2010). It may cause cancer in humans if humans are exposed to concentrations of formaldehyde that exceed safe limits for an extended length of time (Zhang et al., 2009; Wang, 2009; Litto, 2010). Vaughan et al. (1986) reported a significant correlation between formaldehyde exposure and nasopharyngeal cancer in mobile home residents.

### **2.1.8 Volatile organic compounds (VOCs)**

USEPA defines a volatile organic compound (VOC) as a carbon-containing chemical compound that participates in atmospheric photochemical reactions, excluding carbon monoxide, carbon dioxide, carbonic acid, metallic carbides or carbonates, and ammonium carbonate (Spengler et al., 2000). The World Health Organization has a more precise definition: a VOC is an organic compound which has a melting point below room temperature and a boiling point that ranges between 50 °C and 260 °C (Maroni et al., 1995; Spengler et al., 2000). A large number of VOCs are emitted into indoor air from building materials, furnishings, cleaning compounds, office equipment, air fresheners, pesticides, people (such as personal care products and tobacco smoking), and unvented combustion processes (such as cooking with gas stoves) (Jones, 1999; Spengler et al., 2000). Table 2.3 lists sources of common VOCs found in indoor air. VOCs are also produced indoors from chemical reactions of indoor ozone with other VOCs, semi-volatile organic compounds (SVOCs), or materials (such as carpeting) (Weschler, 2004). VOCs also enter buildings with outdoor air; however, for many types of VOCs and SVOCs, indoor air concentrations far exceed outdoor air concentrations.

The phrase "total volatile organic compound" or "TVOC" refers to the resulting concentration of multiple airborne VOCs; however, different sampling and analytic methods can result in obtaining substantially different TVOC concentrations for identical VOC mixtures.

The most common sampling and analytic techniques include collection of the VOCs on a solid sorbent, thermal desorption or solvent extraction, and analysis by a gas chromatograph equipped with a mass spectrometer or flame ionization detector (Spengler et al., 2000). TVOC concentrations typically range from 50 to 1,000  $\mu\text{g}/\text{m}^3$  and can reach hundreds of  $\text{mg}/\text{m}^3$  for periods of minutes to hours. The long-term concentrations can result from the presence of a wide variety of synthetic and natural products and human activities. The high short-term concentrations are most commonly reached when solvent-laden coatings are being applied during building construction or renovations and when certain personal care products, hobby materials, or cleaning agents are used.

Exposure to VOCs can result in both acute and chronic health effects. Most reported TVOC-concentrations in non-industrial indoor environments are below 1  $\text{mg}/\text{m}^3$  and few exceed 25  $\text{mg}/\text{m}^3$ . Over this range, some sensory effects including sensory irritation, dryness, and inflammatory irritation in eyes, nose, airways, and skin irritation may increase. At high concentrations, many VOCs are potent narcotics and can depress the central nervous system (Maroni et al., 1995). At concentrations as high as 188  $\mu\text{g}/\text{m}^3$ , VOCs such as toluene may cause symptoms of lethargy, dizziness, and confusion. These symptoms may progress to coma, convulsions, and possibly death when the VOC concentrations are in excess of 35,000  $\mu\text{g}/\text{m}^3$  (Sandmeyer, 1982). Because of the similar symptoms, exposure to VOCs has frequently been attributed as a cause of sick building syndrome (SBS), discussed later.

Table 2.3 Sources of common volatile organic compounds in indoor air  
(Spengler et al., 2000)

<b>Compound</b>	<b>Categories of indoor sources with reported emissions data</b>
Acetaldehyde	Floor materials, HVAC systems and components, machines, wood products
Benzene	Furnishings, paints and coatings, wood products
Carbon tetrachloride	Pesticides
Chloroform	Furnishings, pesticides
Ethylbenzene	Floor materials, insulation products, machines, paints and coatings
Formaldehyde	Cabinetry, floor materials, furnishings, HVAC systems and components, indoor air reactions, insulations products, miscellaneous materials, paints and coatings, space heating and cooking equipment, wall and ceiling materials, wood products
Hexane	Floor materials, furnishings, paints and coatings, wood products
Methylene chloride	Furnishings
Naphthalene	Pesticides (moth crystals)
Paradichlorobenzene	Pesticides, floor materials
Styrene	Cabinetry, floor materials, insulation products, machines, miscellaneous materials, paints, and coatings, wood products
Tetrachloroethylene	Caulks and sealants, miscellaneous materials
Toluene	Adhesives, caulks and sealants, floor materials, furnishings, machines, paints and coatings, wall and ceiling materials, wood products
Trichloroethylene	Furnishings
Xylenes (o, m, p)	Floor materials, furnishings, machines, paints and coatings, wall and ceiling materials

### 2.1.9 Ozone

Ozone (O<sub>3</sub>) is a strong oxidizing agent. Sources of indoor ozone include photocopiers and laser printers, electrostatic air purifiers and ionizers, and other high voltage electrical equipment. In addition, penetration from outdoors is another important source of indoor ozone.

Ozone has been found to be an irritant of the mucous membranes and the lungs. Exposure to O<sub>3</sub> may cause breathing problems, reduce lung function, exacerbate asthma, irritate

eyes and nose, reduce resistance to colds and other infections, and speed up aging of lung tissue (Zhang and Smith, 2003). The USEPA (1993) reported that exposure to O<sub>3</sub> at relatively low concentrations had been found to significantly reduce lung function, accompanied by symptoms of chest pain, coughing, sneezing, and pulmonary congestion. Long-term repeated exposure to high levels of O<sub>3</sub> can reduce lung function or aggravate existing respiratory conditions, such as asthma or bronchitis. Importantly, as a strong oxidizing agent, indoor O<sub>3</sub> can drive chemical reactions among chemical species present indoors, generating secondary pollutants that may be of greater health concern compared to primary pollutants (Weschler, 2000, 2001). Results from epidemiological research suggested that reactions between indoor O<sub>3</sub> and VOCs could produce irritant substances that could cause SBS (Groes et al., 1996).

#### **2.1.10 Indoor biological pollutants**

Besides chemical pollutants, pollution from biological sources can also pose serious health problems since a large variety of biological materials is present in indoor environments. Biological contaminants include fungi, bacteria, molds, mildew, viruses, animal dander (skin flakes) and cat saliva, house dust mites, pollen and so on (Jones, 1999; Liu and Lipták, 2000). There are many sources of these pollutants. House dust mites, the source of one of the most powerful biological allergens, grow in damp, warm environments. Viruses are transmitted by people and animals. Bacteria are carried by people, animals (saliva and dander), soil and plant debris (pollens and other items); and household pets (such as dogs and cats). In addition, the outdoor air is another major source for fungi, bacteria and pollen, especially during spring and autumn.

Indoor biological contaminants can cause numerous health effects. Some biological contaminants can trigger allergic reactions, including hypersensitivity pneumonitis, allergic

rhinitis, and some types of asthma. Infectious illnesses, such as influenza, measles, and chicken pox are transmitted through the air. Molds and mildews release disease-causing toxins. Symptoms of health problems caused by biological pollutants include sneezing, watery eyes, coughing, shortness of breath, dizziness, lethargy, fever, and digestive problems. Table 2.4 provides information on a number of well-defined disease and disease syndromes associated with exposure to bacteria and fungi. Therefore, it is very important to reduce exposure to biological contaminants through all kinds of methods, such as good housekeeping, adequate ventilation, good air distribution, and better air filtration systems.

Table 2.4 Diseases and disease syndromes associated with exposure to bacteria and fungi (IEH, 1996)

<b>Disease/Syndrome</b>	<b>Examples of causal organisms cited</b>
Rhinitis (and other upper respiratory symptoms)	<i>Alternaria, Cladosporium, Epicoccum</i>
Asthma	Various aspergilli and penicillia, <i>Alternaria, Cladosporium, Mucor, Stachybotrys, Serpula</i> (dry rot)
Humidifier fever	Gram-negative bacteria and their lipopolysaccharide endotoxins, Actinomycetes and fungi
Extrinsic allergic alveolitis	<i>Cladosporium, Sporobolomyces, Aureobasidium, Acremonium, Rhodotorula, Trichosporon, Serpula, Penicillium, Bacillus</i>
Atopic dermatitis	<i>Alternaria, Aspergillus, Cladosporium</i>

### **2.1.11 Sick building syndrome (SBS)**

The phrase “sick building syndrome” (SBS) is used to describe situations in which building occupants experience acute health and comfort effects that appear to be linked to time spent in a building but for which no specific illness or cause can be identified (Redlich et al., 1997; Jones, 1999). The complaints may be localized in a particular room or zone or may be widespread throughout the building. SBS has been reported with increasing frequency since the 1970s, as older, naturally ventilated buildings have been replaced by more energy efficient, “airtight” buildings (Redlich et al., 1997). Surveys conducted in the U. S. and in Europe suggested that 20% or more of occupants in office buildings without knowing it have frequently experienced SBS symptoms (Zweers et al., 1992; Mendell et al., 1996)

Common symptoms of SBS include the following (Wallace, 1997):

- Headache and nausea
- Nasal congestion (runny/stuffy nose, sinus congestion, sneezing)
- Chest congestion (wheezing, shortness of breath, chest tightness)
- Eye problem (dry, itching, tearing, or sore eyes, blurry vision, burning eyes, problems with contact lenses)
- Throat problems (sore throat, hoarseness, dry throat)
- Fatigue (unusual tiredness, sleepiness, or drowsiness)
- Chills and fever
- Muscle pain (aching muscles or joints, pain or stiffness in upper back, pain or stiffness in lower back, pain or numbness in shoulder/neck, pain or numbness in hands or wrists)
- Neurological symptoms (difficulty remembering or concentrating, feeling depressed, tension, or nervousness)

- Dizziness
- Dry skin

SBS reduces worker productivity and may also increase absenteeism. While specific causes of SBS are still unknown, chemical contaminants, biological contaminants, and inadequate ventilation have been cited as contributing factors (Redlich et al., 1997; Jones, 1999).

#### 1) Chemical contaminants

Chemical contaminants from indoor and outdoor sources have been regarded as one of the major causes of SBS. Particularly, the presence of VOCs was thought to play an important role for the causes of SBS for some years (Redlich et al., 1997; Jones, 1999). This view was based on numerous research results. Studies in environmental chambers with simple mixtures of VOCs at high total concentrations (5-25 mg/m<sup>3</sup>) suggest that the exposure to high concentrations can induce SBS symptoms (Møhlhave et al., 1986; Kjaergaard et al., 1989). In a cross-sectional study of SBS symptoms among 147 office workers, Hodgson et al. (1991) found that VOC concentrations in the breathing zone of the building occupants were good predictors of mucous membrane irritation and central nervous system complaints. Brinke et al. (1998) developed a new VOC exposure metric by using data from 22 office areas in 12 California buildings. However, there are numerous studies that have been unable to find any association between VOC exposures and SBS outbreaks (Redlich et al., 1997; Jones, 1999).

#### 2) Biological contaminants

Biological contaminants (such as bacteria, viruses, molds, pollen and dander) can breed in moist areas that are often fed by condensation on evaporator coils in building cooling systems, by stagnant water in vaporizers and humidifiers, in water condensation pans, in building ventilation



ducts, or by water that has collected on ceiling tiles, on insulation, or in carpet. Biological contaminants cause people to develop fever, chills, cough, congestion, chest tightness, muscle aches, and allergic reactions.

### 3) Inadequate ventilation

The 1970s oil embargo caused building designers to make buildings more airtight with less outdoor air ventilation in order to improve energy efficiencies. Having less ventilation in these older buildings has been found to be a primary cause for SBS (Redlich et al., 1997; Jones, 1999). Studies have shown a relation between ventilation rate and SBS (Harrison et al., 1987; Vincent et al., 1997). In addition, inadequate ventilation is a factor for increasing concentrations of indoor pollutants which also have greatly contributed to SBS. In the US, the American Society for Heating, Refrigeration, and Air Conditioning Engineers (ASHRAE) developed a standard for office ventilation and the recommendation is for an input of 20 cubic feet per min (0.57 m<sup>3</sup>/min) of outside air per occupant (ASHRAE Standard 62-1999).

Physical factors (such as temperature and humidity) and psychosocial factors (such as stress and gender) are associated with SBS (Redlich et al., 1997; Jones, 1999; Burge, 2004). Thus SBS appears to have a multi-factorial etiology, in which chemical, physical, biological, and psychosocial factors all interact to produce symptoms and discomfort. One of the effective solutions to SBS is to provide better building filtration service to improve indoor air quality.

## **2.2 Particulate Air Filtration**

Filtration is one of the primary methods for improving indoor air quality in most buildings. Filtration is classified as particle air filtration and molecular filtration based on the types of air contaminants present. The purpose of particle air filtration is to remove particles,

including biological materials, from the air. A diagram of the relative sizes of common air contaminants (e.g., tobacco smoke, pollen, dust) is shown in Figure 2.1. For different particle sizes, there are different particulate air filters that may be used.

### **2.2.1 Particulate air filters**

Particulate air filters are classified as either mechanical filters or electrostatic filters (electrostatically enhanced filters). Although there are many important performance differences between the two filter types, both are fibrous media and both are used extensively in HVAC systems for particle removal. A fibrous filter is an assembly of fibers that are randomly laid perpendicular to the airflow. The fibers may range in size from less than 1  $\mu\text{m}$  to greater than 50  $\mu\text{m}$  in diameter. Filter packing density may range from 1% to 30%. Fibers may be made from cotton, fiberglass, polyester, polypropylene, or numerous other materials (Davies, 1973).

Fibrous filters of different designs (panel filters, pleated filters, pocket filters, and so on) are used for various applications. Flat-panel filters contain all of the media in the same plane. This design keeps the filter face velocity and the media velocity roughly the same. When pleated filters are used, additional filter media are added to reduce the air velocity through the filter media. This enables the filter to increase collection efficiency for a given pressure drop. With pocket filters, air flows through small pockets constructed of the filter media. These filters can consist of a single large pocket or multiple pockets. The multiple pocket design increases the collection surface area. As in pleated filters, the increased surface area reduces the velocity of the airflow through the filter media, allowing increased collection efficiency for a given pressure drop.

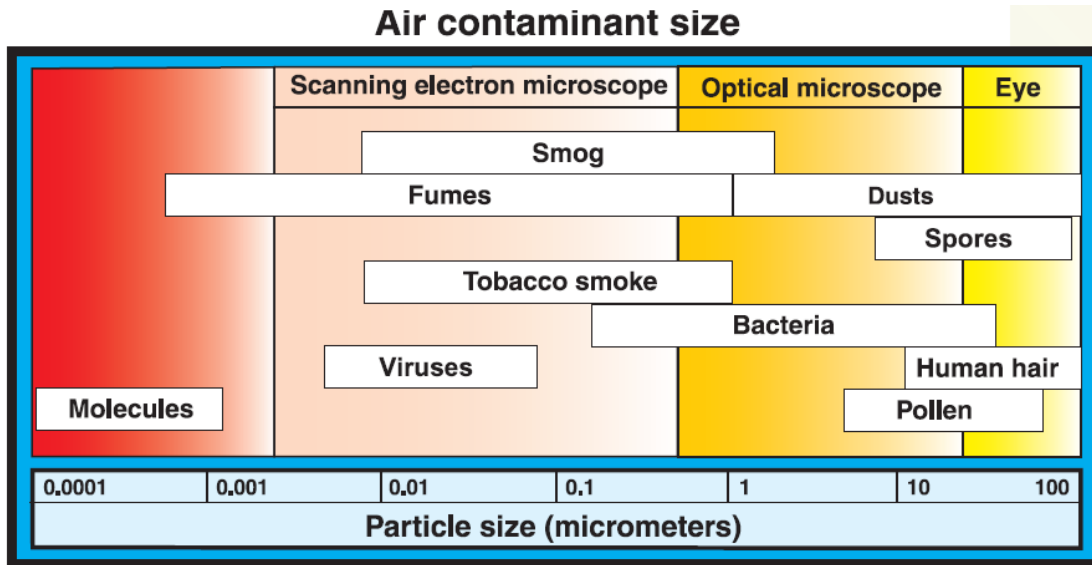


Figure 2.1 Common air contaminants and their relative sizes (Hinds, 1982)

### 2.2.2 Mechanisms for particulate air filtration

A filter's primary function is the removal of particulate matter from the air stream. The filter accomplishes this through a series of mechanisms that act in conjunction to capture particles on the filter media. These mechanisms are sieving, inertial impaction, interception, diffusion, and electrostatic attraction (Davis, 1973; Brown, 1993; Robinson and Ouellet, 1999).

Sieving occurs when the particle is larger than the opening between media fibers (Figure 2.2). Sieving is the dominant method of particle removal in low efficiency air filters.

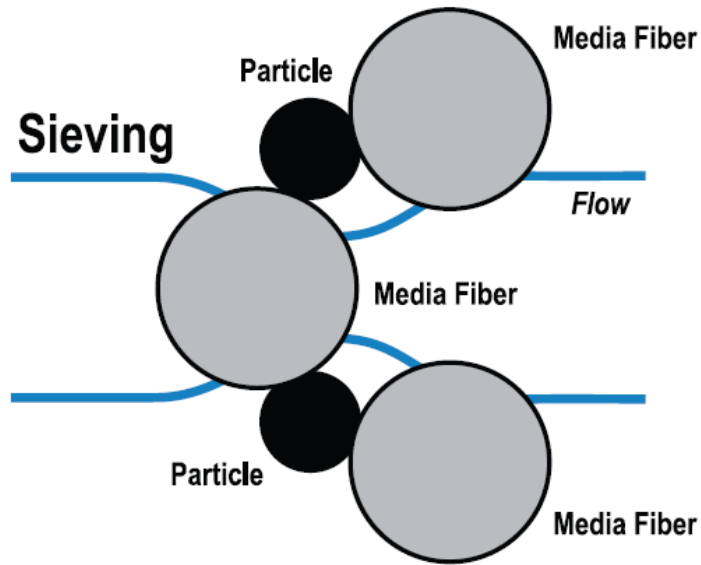


Figure 2.2 Sieving mechanism for particle capture

Inertial impaction occurs when a large, dense particle that is traveling in the air stream and passing around a fiber, deviates from the air stream (due to particle inertia) and collides with a fiber (Figure 2.3).

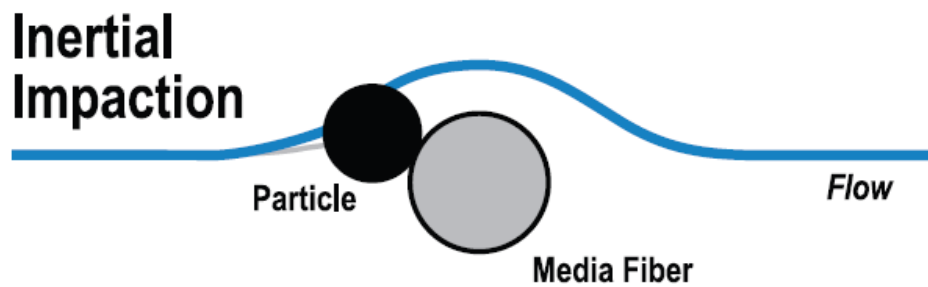


Figure 2.3 Inertial impaction mechanism for particle capture

Interception occurs when a large particle, because of its size, collides with a fiber in the filter that the air stream is passing through (Figure 2.4). Interception is the primary method of particulate removal for medium efficiency air filters.

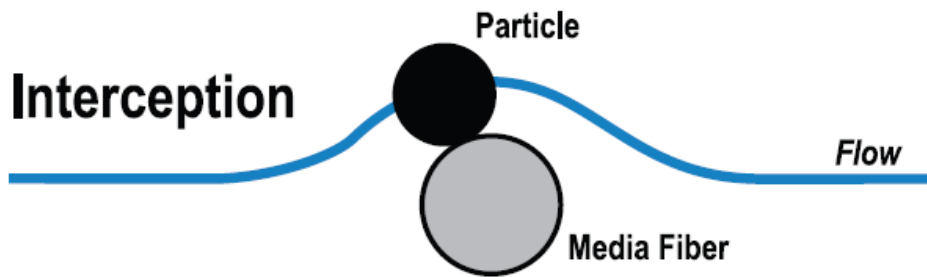


Figure 2.4 Interception mechanism for particle capture

Diffusion occurs when very small particles (Figure 2.5) in the air flow collide with the air molecules and move in a random motion (Brownian movement). This motion allows the small particles to come in contact with the media fibers and stay attached. The probability of capture increases with the increased density of fibers, with the decreased diameter of the fibers, and with the increased resident time within the fiber mesh (Brown, 1993). Particles will be deposited on all sides of the fiber when this mechanism is prevalent. Diffusion is the dominant method of particulate removal in high efficiency air filters.

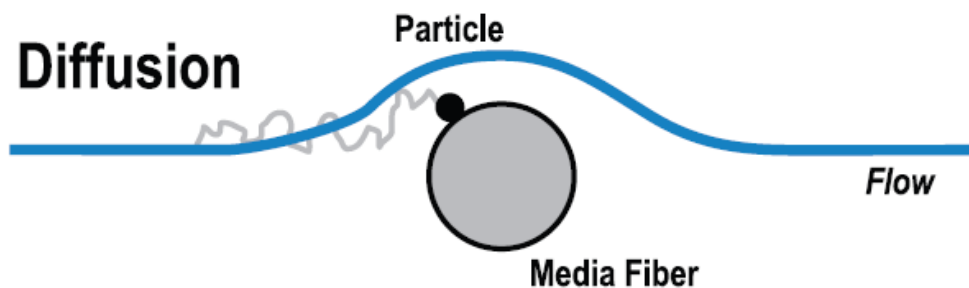


Figure 2.5 Diffusion mechanism for particle capture

Electrostatic attraction occurs when particles are attracted to and retained by the fibers using electrostatic forces (Figure 2.6). Electrostatic deposition is important in those filters that employ a charged surfactant coating for drawing particles out of the air stream. These filters are called electrostatic filters. Electrostatic filters lose their electrostatic charge over time because

the captured particles occupy the charged surface sites and thus neutralize the electrostatic charges for capturing more particles. Electrostatic attraction plays a very minor role in mechanical filtration and is beyond the scope of this research.

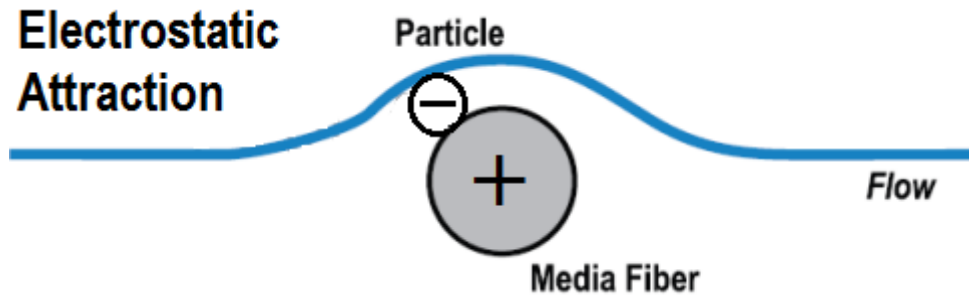


Figure 2.6 Electrostatic attraction mechanism for particle capture

Impaction, interception and diffusion mainly apply to mechanical filters and are influenced by particle size. Impaction and interception are the dominant collection mechanisms for particles greater than  $0.2 \mu\text{m}$ , whereas diffusion is dominant collection mechanism for particles less than  $0.2 \mu\text{m}$ . The combined effect of these three collection mechanisms results in the classic collection efficiency curve as shown in Figure 2.7. As mechanical filters are loaded with particles over time, their collection efficiency and the air flow resistance (pressure drop) typically increase. Eventually, the increased pressure drop would significantly inhibit airflow and the filters must be replaced. For this reason, pressure drop across mechanical filters is often monitored because it indicates when to replace filters.

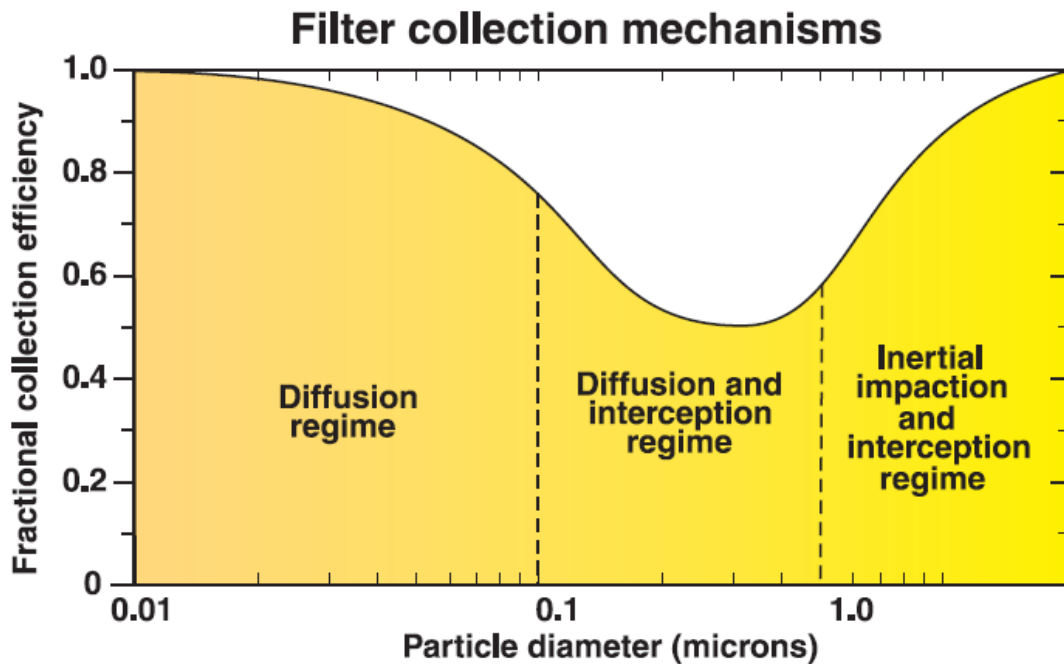


Figure 2.7 Fractional collection efficiency versus particle diameter for a mechanical filter (Lee and Liu, 1980)

### 2.2.3 Standards for determining and measuring particulate filter performance

Air filters are commonly described and rated based upon their collection efficiency, pressure drop, and particulate-holding capacity (dust loading capacity). Two filter test standards are currently used in the US (Robinson and Ouellet, 1999; ASHRAE Standard 52.1& 52.2):

1. ASHRAE Standard 52.1-1992, gravimetric and dust spot procedures for testing air cleaning devices used in general ventilation for removing particulate matter
2. ASHRAE Standard 52.2-1999, method of testing general ventilation air-cleaning devices for removal efficiency by particle size

ASHRAE Standard 52.1-1992 provides three important evaluation criteria, which are arrestance, dust spot efficiency, and dust holding capacity. Arrestance means the ability of a filter to capture a mass fraction of coarse test dust and is suited for describing low and medium

efficiency filters. Dust spot efficiency is a measure of the ability of a filter to remove large particles. Dust holding capacity is a measure of the total amount of dust a filter is able to hold during a dust loading test. This standard addresses the ability to protect machines and coils and the ability to remove staining size particles.

ASHRAE Standard 52.2 measures particle size efficiency (PSE). This standard quantifies the filtration efficiency for a clean filter and for an incrementally loaded filter and thus provides a composite efficiency value for different particle size ranges. This gives a better determination of a filter's effectiveness for capturing solid particulate as opposed to liquid aerosols. ASHRAE Standard 52.2 rates particle-size efficiency results as a Minimum Efficiency Reporting Value (MERV) between 1 and 20 and minimum PSE for three size ranges for each of the MERV numbers (see Table 2.5). Therefore, ASHRAE Standard 52.5 provides guidance for selecting an appropriate filter when the size of the expected particle contaminant is known. Most of our filter test experimental work in the following chapters is based on the ASHRAE Standard 52.2.



Table 2.5 ASHRAE Standard 52.2 MERV parameters and application guidelines (ASHRAE 52.2, 1999)

MERV	Particle size range, $\mu\text{m}$			Typical Air Filter Type	Typical Controlled Contaminant	Applications
	0.3 to 1.0	1.0 to 3.0	3.0 to 10.0			
1	–	–	< 20%	Panel Filter	> 10 $\mu\text{m}$ Particle Size	Minimum filtration, residential, window air conditioners
2	–	–	< 20%	Panel Filter		
3	–	–	< 20%	Panel Filter		
4	–	–	< 20%	Panel Filter		
5	–	–	20 - 35 %	Cartridge Filter	3.0-10 $\mu\text{m}$ Particle Size	Commercial buildings, better residential, industrial workplace, paint both inlets
6	–	–	35 - 50%	Cartridge Filter		
7	–	–	50 - 70%	Cartridge Filter		
8	–	–	> 70%	Pleated Filter		
9	–	< 50 %	> 85%	Pleated Filter	1.0-3.0 $\mu\text{m}$ Particle Size	Superior residential, better commercial buildings, hospital laboratories
10	–	50 - 60 %	> 85%	Pleated Filter		
11	–	65 - 80 %	> 85%	Box Filter		
12	–	> 80%	> 90%	Box Filter		
13	< 75%	> 90%	> 90%	Bag Filter	0.3-1.0 $\mu\text{m}$ Particle Size	Hospital inpatient care, general surgery, smoking loungers, superior commercial buildings
14	75 - 85%	> 90%	> 90%	Bag Filter		
15	85 - 95%	> 90%	> 90%	Bag Filter		
16	> 95%	> 95%	> 95%	Bag Filter		
17	$\geq 99.97\%$	–	–	HEPA Filter	$\leq 0.3\mu\text{m}$ Particle Size	Clean rooms, radioactive materials, pharmaceutical manufacturing, carcinogenic materials, orthopedic surgery
18	$\geq 99.99\%$	–	–	HEPA Filter		
19	$\geq 99.999\%$	–	–	ULPA Filter		
20	$\geq 99.9999\%$	–	–	ULPA Filter		

## **2.3 Molecular Filtration**

Although higher MERV rated filters excel at removing particulate matter, these filters cannot remove gaseous contaminants such as CO, CO<sub>2</sub>, NO<sub>2</sub>, O<sub>3</sub>, VOCs, and other airborne molecular contaminants. A second filtration system, such as a packed bed or monolith, must be employed in order to successfully remove the non-particulate contaminants.

### **2.3.1 Sorbents for molecular filtration**

Gas phase filters are typically deep bed filters loaded with materials such as activated carbon, activated alumina, silica gel, zeolites, molecular sieves, porous clay minerals, or other sorbents (such as engineered polymers). Once the materials are spent, gas phase filters must be replaced or regenerated by application of heat or other processes. Factors affecting gas phase filter life include removal capacity, sorbent weight, sorbent collection efficiency, airflow rates, molecular weight, and the concentration of the targeted contaminant.

Sorbent selection for an airborne contaminant is very important for gas phase filters to achieve high removal efficiency. The USEPA (1999) stated that “a well-designed adsorption system for industrial contaminant concentrations should have removal efficiencies ranging from 95% to 98% and a collection rate in the range of 500 to 2,000 ppm”. Such higher collection efficiencies are needed for dealing with high toxicity chemical, biological, or radiological agents. For different chemical agents, sorbents have different affinities, removal efficiencies, and saturation points depending on their various physicochemical properties (pore size and shape, surface area, pore volume and so on) and chemical inertness. Table 2.6 lists common gaseous contaminants and their corresponding sorbents used in gas phase filters. Some of the commonly used sorbents are described below.

Table 2.6 Gases and respective removal media (Parsons, 1991)

<b>Gas or Vapor</b>	<b>Removal Media</b>
Acid gases	Activated carbon
Carbon dioxide	Molecular sieves; lithium oxides, sodium oxides; potassium oxides
Carbon monoxide	Activated alumina impregnated with platinum or rhodium oxides
Formaldehyde	Activated alumina impregnated with compound consisting of copper chloride and palladium chloride
Hydrogen sulfide	Activated alumina impregnated with potassium permanganate
Mercury vapor	Activated carbon impregnated with iodide, silver, sulfur, or potassium iodide
Nitrogen dioxide	Activated carbon impregnated with sodium bicarbonate (baking soda)
Sulfur dioxide	Activated alumina impregnated with potassium permanganate
Water vapor	Silica gel
Radioactive iodine	Activated carbon impregnated with iodide or potassium trioxide
Ozone	Activated carbon
Organic vapors	Activated carbon, porous polymers
Polar organic compounds (alcohols, phenols, aliphatic and aromatic amines, etc.)	Activated alumina; activated bauxite; silica gel

### **Activated carbon**

Activated carbon is the most common sorbent used in HVAC systems and it is excellent for capturing most organic chemicals. Activated carbon is prepared from carbonaceous materials, such as wood, coal, bark, or coconut shells. Activation partially oxidizes the carbon to produce sub-micrometer pores and channels, which give the high surface area-to-volume ratio needed for a good sorbent (Figure 2.8).

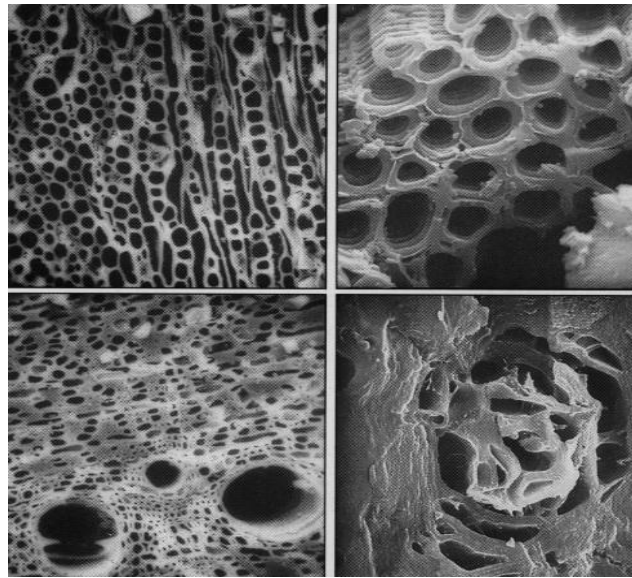


Figure 2.8 Scanning electron microscope image of activated carbon pores ([www.lowenergyairfilter.co.uk](http://www.lowenergyairfilter.co.uk))

Activated carbon often has surface areas in the range of 1,000 m<sup>2</sup> per gram (m<sup>2</sup>/g). The surface of activated carbon is highly irregular, and pore sizes range from 0.5 to 50 nm, enabling adsorption of many substances. Typically, activated carbon is prepared from coconut shells because of smaller pore sizes. Activated carbon produced from bituminous coal has larger pores. When the activated carbon has been spent, it may be regenerated by thermal methods or by using solvent extraction. Since activated carbon is nonpolar, some organic vapors cannot be captured, such as formaldehyde. In order to enhance the range of vapors that activated carbon can adsorb, chemical impregnation is commonly used. The impregnation optimizes the existing properties of the activated carbon by giving a synergism between the chemicals and the carbon. Reactive chemicals have been successfully impregnated into activated carbon for decomposing chemically high vapor pressure agents, such as the blood agent cyanogen chloride (CK) and hydrogen cyanide (AC) (Henning and Schäfer, 1993). A frequently used impregnated activated carbon is ASZM-TEDA carbon, a coal based activated carbon that has been impregnated with

copper, silver, zinc, and molybdenum compounds, as well as with triethylenediamine (TEDA) (Miller, 2002). Since ASZM-TEDA can provide a high level of protection against a wide range of chemical warfare agents, it has been used in US military nuclear, biological and chemical (NBC) filters since 1993 (Miller, 2002).

### **Silica gel**

Silica gel is a common inorganic sorbent that is used to trap polar compounds. Sorption takes place when the polar functional group of a contaminant molecule is attracted by hydrogen bonding or electron cloud interaction with oxygen atoms in the silica. Silica gels are inorganic polymers having a variety of pore sizes and surface areas. Silica gel adsorbs water in preference to hydrocarbons and wet silica gels do not effectively adsorb hydrocarbons. This property makes silica gel a poor sorbent for humid environments; however, amines and other inorganic compounds can be collected on silica gel.

### **Activated alumina**

Activated alumina is another common inorganic sorbent for trapping polar compounds. By changing the surface pH from acidic to basic, alumina can be modified to adsorb a wider polarity range than silica gel. It is prepared by dehydroxylating aluminium hydroxide. As a highly porous material, activated alumina has a pore size of approximately 5.8 nm and a surface area as high as 200 m<sup>2</sup>/g. Chemical impregnation may be used to enable removal of a wide range of airborne molecular contaminants. For example, potassium permanganate impregnated alumina is often used in conjunction with activated carbon or impregnated carbon to provide a very broad-spectrum gas-phase air filtration system.

## **Zeolites**

Zeolites are microporous, aluminosilicate minerals commonly used as commercial sorbents. They have crystalline structures with uniform pore sizes. Zeolites occur in fibrous and non-fibrous forms and may go through reversible selective adsorption. Different molecular structures result in pore sizes ranging from 3 to 30 angstroms. Zeolites are hydrophilic and may be chemically impregnated to improve performance. Zeolites are used for organic solvents and for volatile, low molecular weight halides, such as chlorinated fluorocarbons (CFCs). A primary issue related to the effective use of zeolites is the molecular size of the vapor compared to the pore size. Zeolites will not adsorb molecules larger than their pore sizes, nor will they capture compounds for which they have no affinity. Synthetic zeolites are made in crystals in sizes between 1  $\mu\text{m}$  to 1 mm and are bonded to large granules, reducing airflow resistance. They can be manufactured to have large pore sizes and to be hydrophobic for use in high relative humidity. Synthetic zeolites can be designed to adsorb specific contaminants by modification of pore sizes. Alumina-enriched zeolites have a high affinity for water and other polar molecules whereas silica-enriched zeolites have an affinity for non-polar molecules (USEPA, 1998).

### **2.3.2 Mechanisms for gaseous contaminant removal**

Adsorption, chemisorption, and catalysis are the primary mechanisms for gaseous contaminant removal. A general assessment of each mechanism is presented below.

#### **Adsorption**

Adsorption is a physical process that occurs when a gaseous contaminant adheres to the surfaces of or in the pores of a sorbent material. Due to the relatively weak forces holding the adsorbed gas on the sorbent, adsorption is totally reversible. Since the gaseous contaminant is

captured on the surface of a sorbent, the removal capacity depends on the total available surface area. Adsorbed water reduces the capacity of the sorbent to target the desired gases due to a reduction in the number of available adsorptive sites. Therefore, adsorption occurs more readily at lower humidity. In addition, the adsorptive capacity is also a function of the contaminant concentration; the higher the contaminant concentration, the greater the amount that will be adsorbed. There are other factors that can affect the removal of gaseous contaminants by physical adsorption, such as the type of sorbent, the resistance to airflow, the sorbent bed depth, the air velocity through the bed, the characteristics of the contaminant in the space around the adsorbent, and so on.

### **Chemisorption**

Chemisorption is a process related to physical adsorption, except that a chemical reaction occurs once the contaminant comes into contact with a reagent on the surface of adsorbent material. The sorbent forms a chemical bond with the contaminant or converts it into more benign chemical compounds. Because the stronger molecular (valence) forces are involved, chemisorption is usually considered to be an irreversible process. Therefore, desorption of target contaminants, once adsorbed and chemically reacted, does not occur. Chemisorption depends on the chemical nature of both the sorbent medium and the contaminants to be controlled. Some oxidation reactions have been shown to occur spontaneously on the surface of the adsorbent. However, a chemical impregnant is usually added to the adsorbent, which makes it more or less specific for a contaminant or group of contaminants. For example, activated carbon is impregnated with potassium hydroxide (KOH) for the removal of acid gases such as chlorine, hydrogen fluoride, and sulfur dioxide. Many of the same factors that affect the removal of gases by physical adsorption also affect their removal

by chemisorptions. Higher temperatures and humidity are favored during chemisorption, since higher temperature increases the rates of reaction and the extra water enhances the ability of the adsorbed gases to contact the chemical impregnant.

## **Catalysis**

Catalysis is a process in which the catalyst assists a chemical change in another substance. The change (usually inducing or accelerating a chemical reaction) removes the contaminant without the catalyst itself undergoing any change. Compared with adsorption and chemisorptions, catalysis usually works for one target gas contaminant due to the high selectivity of the catalyst.

Catalytic technologies have been widely used in the improvement of indoor air quality. For example, catalyst tablets are commercially available for eliminating smoke and odors that are produced when fish or meat is cooked on barbeque grills. Another commercially available catalyst is placed on top of an oil stove burner for eliminating the odor of aldehydes that come from imperfect combustion when a stove is extinguished (Nishino, 1991). Photocatalytic active titanium dioxide films can be used in reducing indoor air microbial contamination (Centi et al., 2002). Catalytic removal of  $\text{NO}_x$  from mobile and stationary sources has been widely investigated and low temperature catalysts have been developed. One use is  $\text{NO}_x$  reduction in diesel engine exhaust emissions (Armor, 1998; Centi et al., 2002; Garin, 2004). Catalytic oxidation for carbon monoxide removal can be achieved with a number of catalysts with the application and the conditions of use determining which one should be used (Viso et al., 1997; Lin et al., 2003). The conversion of VOC to  $\text{CO}_2$ ,  $\text{H}_2\text{O}$  and  $\text{HCl}/\text{Cl}_2$  can be achieved on different catalysts (Everaert and Baeyens, 2004). Low concentration of formaldehyde in indoor air can be completely converted into harmless  $\text{CO}_2$  and  $\text{H}_2\text{O}$  over supported catalysts at low temperature,



even room temperature (Álvarez-Galván et al, 2004; Zhang et al., 2005; Zhang et al, 2006; Zhang and He, 2007; Tang et al., 2008; Huang and Leung, 2011). A large number of catalysts have been examined from room temperature catalytic decomposition of O<sub>3</sub> (Ellis and Tometz, 1972; Ohtani et al., 1992; Hao et al., 2001; Subrahmanyam et al., 2005). Several valuable commercial applications have been developed, such as O<sub>3</sub> smog reducers (radiators coated with catalysts for converting O<sub>3</sub> to O<sub>2</sub>), O<sub>3</sub> converters in jet aircraft, and O<sub>3</sub> devices in office equipment (Centi et al., 2002). Similar technology has been applied to filters, to forced-air systems, to aircraft air conditioning ducts, to air conditioning condensers, and to heat pumps.

Development of novel catalysts with low cost will make the application of catalytic techniques in gas phase filtration economically more favorable. There are some important parameters that affect the performance of gas-phase air filtration, including breakthrough concentration, breakthrough time, challenge concentration, residence time, and mass transfer zone (critical bed depth).

Breakthrough concentration is the downstream contaminant concentration. This indicates the agent has broken through the sorbent. This parameter is a function of loading history, relative humidity, and other factors.

Breakthrough time is the elapsed time between the initial contact of the toxic agent at a reported challenge concentration on the upstream surface of the sorbent bed and the breakthrough concentration on the downstream side of the sorbent bed.

Challenge concentration refers to the airborne concentration of the gaseous contaminant entering the sorbent.

Residence time is the length of time that the contaminant spends in contact with the sorbent. This is calculated on the basis of the adsorbent bed volume and the volumetric flow rate.

Mass transfer zone or critical bed depth refers to the adsorbent bed depth required to reduce the chemical vapor challenge concentration to the breakthrough concentration. When applied to the challenge chemicals that are removed by chemical reaction, mass transfer is not a precise descriptor, but is often used in that context. The portion of the adsorbent bed not included in the mass transfer zone is often termed the capacity zone.

## Chapter 3 Experimental Apparatus and Test Procedure

### 3.1 Introduction

There are three primary parameters to evaluate filter performance. These are pressure drop, removal efficiency, and dirt holding capacity.

Pressure drop indicates the airflow resistance of a filter. Typically the initial and the final (terminal) pressure drop values are collected. Pressure upstream minus pressure downstream equals pressure drop, which is commonly referred to as Delta P, or  $\Delta P$  (Figure 3.1). This value is typically expressed in inches of water (" H<sub>2</sub>O), or Pascals (Pa). Pressure drop is related to the energy required to push the airflow through the filter. Filter life is usually based on the final pressure drop, therefore, some systems use it as the indicator for changing filters.

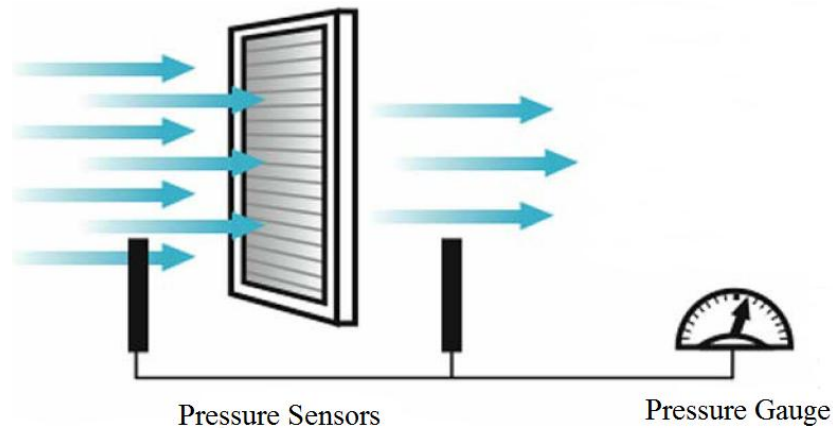


Figure 3.1 Illustration of pressure drop measurement

Removal efficiency is the ratio of particles captured by a filter over the total number of particles found in the upstream air of the filter. It can either be based on specific particle size ranges or based on the total number of particles of all sizes. Removal efficiency can be defined

by Equation 3.1, where  $G_1$  is an amount of penetrated particles and  $G_2$  is the total amount of particles upstream. And expression  $\frac{G_1}{G_2}$  is defined as penetration  $P$  (Equation 3.2). Filtration engineers use particle counters upstream and downstream of filters to count particles and measure fractional efficiency (Figure 3.2).

$$E = \left(1 - \frac{G_1}{G_2}\right) \times 100\% \quad (3.1)$$

$$P = \frac{G_1}{G_2} \times 100\% \quad (3.2)$$

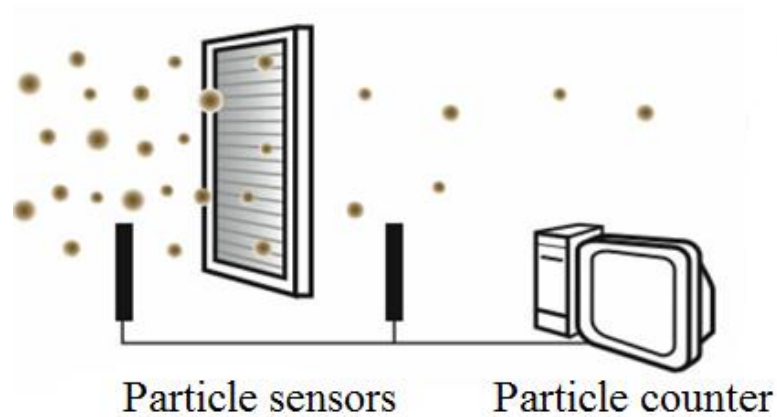


Figure 3.2 Illustration of removal efficiency measurement

Dirt holding capacity is the accumulated mass of dirt a filter can hold until its final pressure drop is reached, which is an indicator of filter lifetime. Larger dirt holding capacity means a longer filter lifetime. For filter designers, increasing dirt holding capacity means expanding the lifetime of filter and reducing the frequency of filter replacing, which will result in lower maintenance costs.

### 3.2 Experimental Set-up

Two separate test rigs were constructed and used to measure the pressure drop, the removal efficiency, and the dirt loading capacity across a media sample and across a filtration

system. A general description of test rigs, control runs, and equipment verification are provided in this section.

### **3.2.1 Small-scale media test rig**

A small-scale media test rig was designed and constructed in our laboratory to investigate the properties of various filter media samples. The media sample size is 5.5" × 5.5". A schematic for the rig is shown Figure 3.3.

Room air was introduced into the test rig by a New York Blower Co. 6-inch air handler at the maximum flow rate of 1,000 cfm. The small rig could incrementally load 0.05 grams of challenge dirt through the use of a 3 ft<sup>3</sup>/min (0.09 m<sup>3</sup>/min) Venturi pump. It was experimentally observed and numerically calculated that the flow was sufficiently turbulent under test conditions to prevent settling inside the test rig. The challenge dust was distributed throughout the duct work by a combinational orifice plate and perforated disc mixer. The orifice's pressure drop was used to calculate the system's volumetric flow. Pressure measurements were made at four pressure taps located ninety degrees apart from one another around the perimeter of the duct. The taps were tied together by a manifold to reduce potential spatial variations between the measurements. A second, identical set of taps was placed around the perimeter of the downstream duct. Pressure drop across the orifice and media sample were monitored by two Invensys IPO10 differential pressure transducers. The correlated flow was verified by comparing the full range of pressure drop measurements against the unit's blower curve as well as a nine-point velocity measurement. The velocity measurements were made with a vane anemometer and re-verified with a hot-wire anemometer. Figure 3.4 is a photograph of the small-scale media test rig.

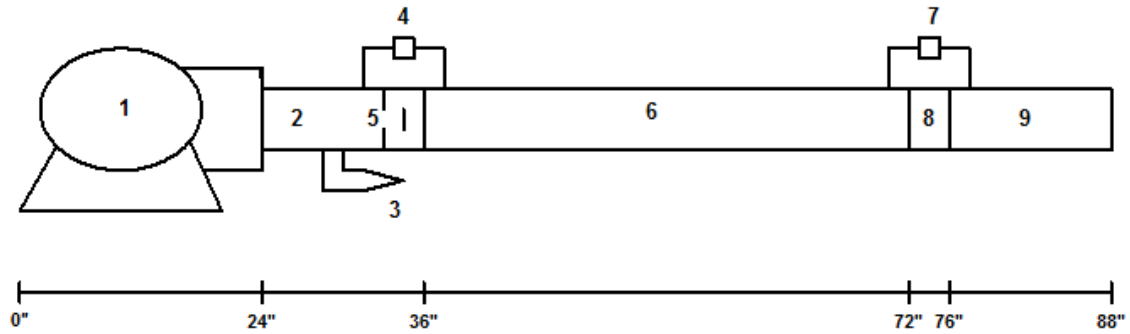


Figure 3.3 Schematic of small-scale filter media test rig

### Equipment and Segments

- |                         |                         |
|-------------------------|-------------------------|
| 1. Blower               | 6. Upstream Duct        |
| 2. Connector Sleeve     | 7. Pressure Transmitter |
| 3. Venturi Pump         | 8. Test Section         |
| 4. Pressure Transmitter | 9. Downstream Duct      |
| 5. Mixer                |                         |

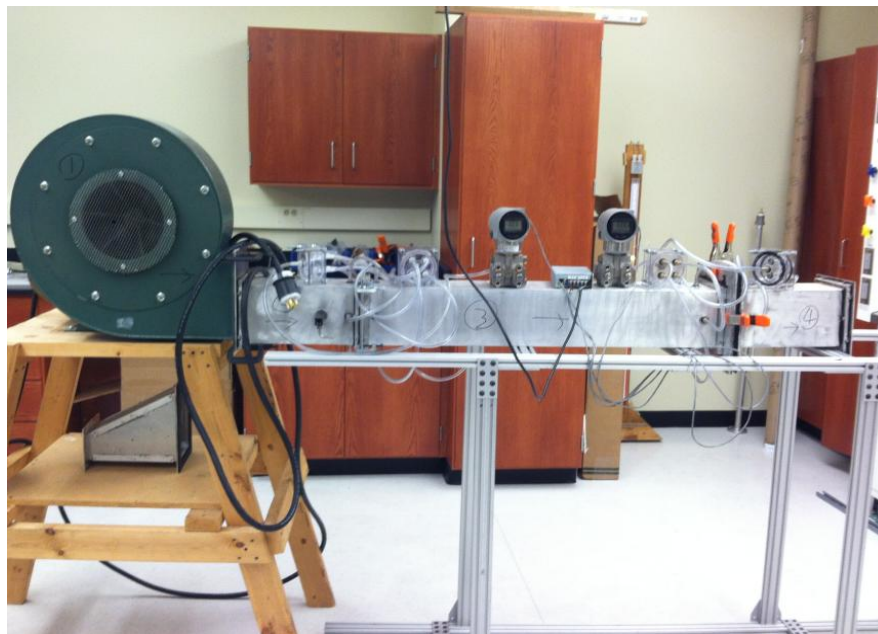


Figure 3.4 Picture of small-scale media test rig

### 3.2.2 Full-scale filter test rig

A full-scale filter test rig was constructed in our laboratory according to the ASHRAE 52.2 Standard (ASHRAE 2007). A general schematic is illustrated in Figure 3.5. Room air was

introduced into the test duct by a Dayton systems blower driven by a 3 HP Hitachi motor. The blower could deliver the required 2,000 cfm correlating to a 500 fpm face velocity with up to 4.4" H<sub>2</sub>O. The motor was controlled by a Hitachi SJ200 frequency drive with a range of 0 to 60 Hz at 0.1 Hz increments. The resistance across the blower was averaged by a four-tap configuration and measured by an Omega PX 154-010DI pressure transducer connected at the blower's outlet (Figure 3.6).

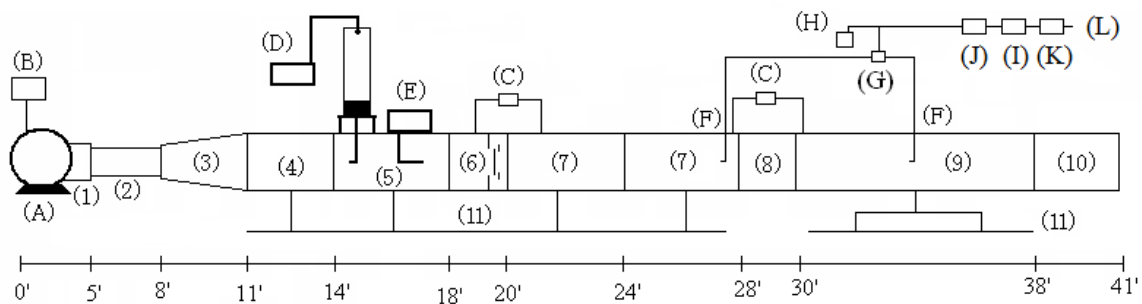


Figure 3.5 Schematic of full-scale filter test rig (Sothen, 2009)

### Equipment

- (A) Blower
- (B) Frequency Drive
- (C) Differential Pressure Transmitter
- (D) Aerosol Generator
- (E) Dirt Loader
- (F) Isokinetic Probe
- (G) Three-way Valve
- (H) Particle Counter
- (I) Inline HEPA Filter
- (J) Mass Flow Controller
- (K) Dessiccant
- (L) House Air

### Segments

- (1) Outlet Sleeve
- (2) Connector Sleeve
- (3) Upstream Expansion
- (4) Upstream Filter Box
- (5) Aerosol Inlet
- (6) Upstream Mixer
- (7) Upstream Duct
- (8) Test Section
- (9) Downstream Duct
- (10) Downstream Filter
- (11) Railing System

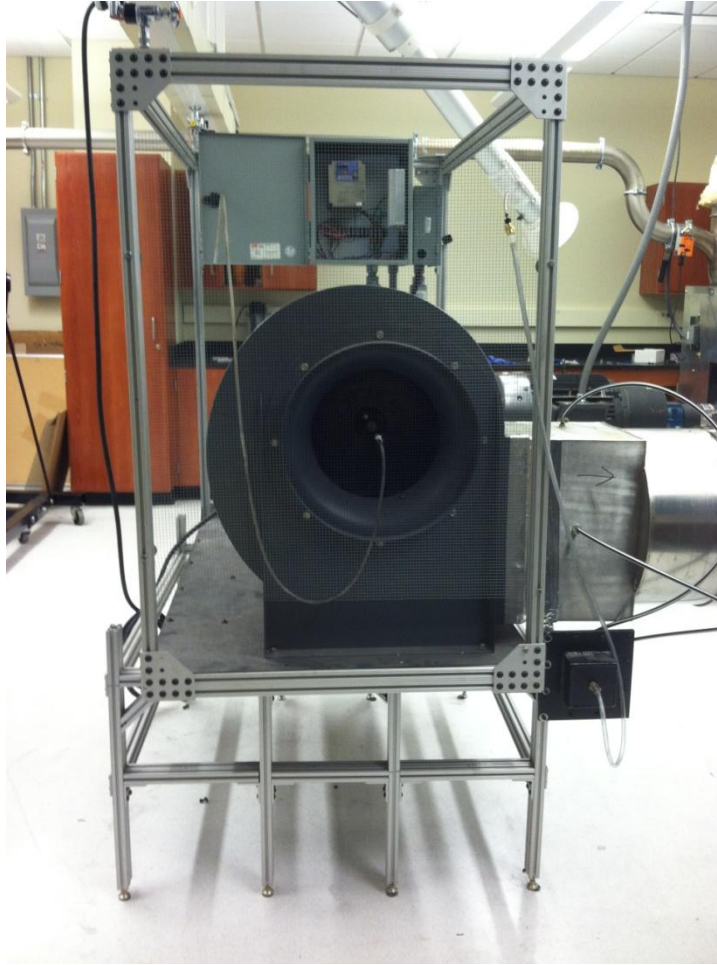


Figure 3.6 Blower and four-tap configuration

The air exited the blower via a stainless steel four-way expansion that increased the cross section area of the rig to 24" × 24". The transition led directly to an upstream filtration box that is capable of holding a HEPA air filter or a 36 inch deep pocket filter. All dirt loading and efficiency tests employed the HEPA filter while initial pressure drop tests utilized the pocket filter. The HEPA filter (purchased from American Air Filters) is capable of removing 99.97% of 0.3 μm diameter particulate matter. High removal efficiency was needed for removing background contaminations and for providing a uniform baseline during efficiency testing. The pocket filter was used when large volumetric flow rates were needed without concern for high



purity background air. The clean air would pass from the filtration box into the aerosol inlet section.

In order to create challenge particles spanning three orders of magnitude, the system was equipped with a TSI 8108 large particle generator. The TSI 8108 system was built to output a polydispersed challenge of KCl particles in the range of 0.1 to 10  $\mu\text{m}$ . The particles were created by pumping a 30% KCl solution at 1.2 mL/min into a spray nozzle where it was mixed with 1 cfm of atomizing air. The nebulized particles were dispersed into a 12-inch diameter by 52-inch high plenum where the droplets were dried with 4 cfm of preheated air. An air ionizer neutralized any charges present on the aerosol. Charge removal was necessary to prevent the particle from being artificially captured by electrostatic deposition within the ductwork or the test filter. The KCl particles were delivered into the center of the ductwork facing the direction of flow by a 1.5 inch NPT pipe. Distribution was enhanced by introducing the particles in this manner. The generator produced a stable concentration of  $6 \times 10^8$  particle/ $\text{m}^3$  of 1  $\mu\text{m}$  and  $1 \times 10^7$  particle/ $\text{m}^3$  of 10  $\mu\text{m}$  aerosol when nebulizing the KCl solution. The manufacturer's schematic is shown in Figure 3.7.

A Blue Heaven Technologies custom-built dust loader was used to artificially age the test filter with a high concentration of particulate matter. The loader was designed to meet the ASHRAE 52.2 Standard. House air was dried by a desiccant bowl before being supplied to the unit at 80 PSI. The air throttling through a Venturi pump caused a vacuum to be formed on the feed tray. The feed tray, driven by a belt, brought the challenge dirt into the proximity of the vacuum at a steady linear rate of 0.5 fpm. A common artificial aging material, ASHRAE synthetic test dirt, was used in our experiments. ASHRAE dirt is composed of, by weight, 72% ASTM ISO fines, 23% powdered carbon black, and 5% milled cotton linters. ASTM ISO fines

are a mixture of alumina oxide and silica dioxide. The carbon black is Raven 411. Figure 3.8 shows the size distribution provided by the manufacturer.

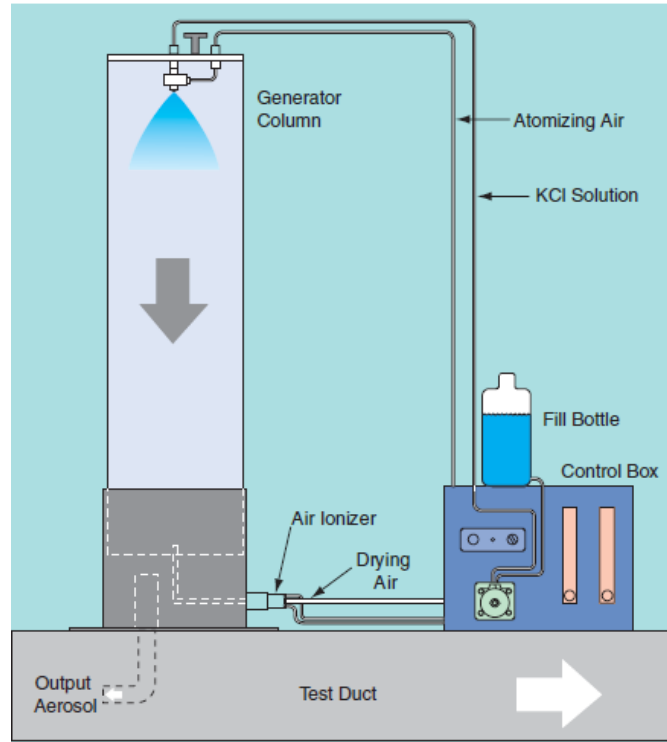


Figure 3.7 Schematic of TSI 8108 large particle generator

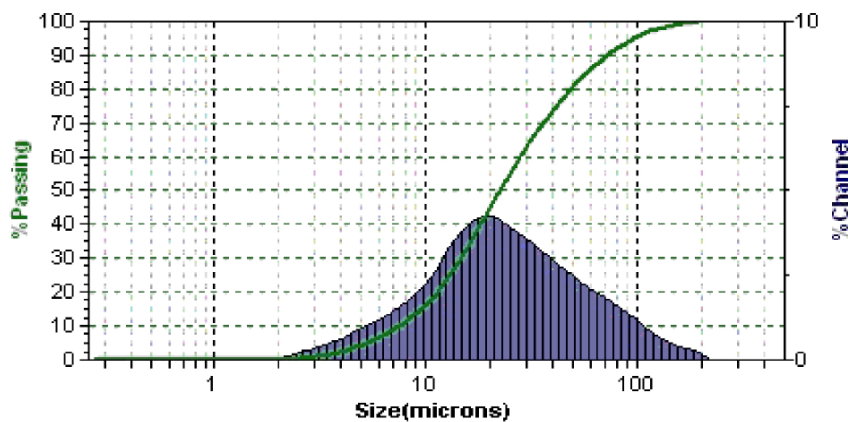


Figure 3.8 ASHRAE dust size distribution

The challenge dirt was mixed and distributed throughout the cross section of the system by the upstream static mixer. The three-part mixer began by contracting and concentrating the

loaded air with a 12-inch circular opening orifice plate. To expand and distribute the mixed air, a 12-inch circular disk built from a 50% blocked perforated stainless steel was located one foot behind the orifice plate. A stainless steel ring with an outside diameter of 18 inches and an inner diameter of 12 inches was formed from a 50% blocked perforated stainless steel sheet. This was followed by a 6-inch disk in order to further distribute the loaded air. The test air reached the filtration system via two four-foot long sections designed to allow the air to further distribute and self-correct. The mixer, in conjunction with the upstream duct, provided a uniform flow into the filtration test section. Table 3.1 showed that the coefficient of variances (CoV) for the delivered airflow to the filtration section was less than 10%, as mandated by ASHRAE Standard 52.2. The upstream duct also housed an isokinetic probe used during removal efficiency testing. The probe was located 12 inches ahead of the filtration unit and was positioned in the center of the ductwork.

Table 3.1 Average velocity and coefficient of variation within the test rig (Sothen, 2009)

Setting (Hz)	15	20	30	40	50	60
Average Velocity (m/s)	1.05	1.39	2.04	2.80	3.49	4.22
Standard Deviation	0.06	0.11	0.11	0.21	0.29	0.32
Coefficient of Variance	6.18	8.03	5.52	7.53	8.32	7.60

The test section had an adjustable region that could accommodate filtration units up to 36 inches in depth. The depth adjustment was accomplished through a linear motion track, created out of 80/20 T-slotted aluminum extrusion (2" in height and 1" in width), on which the downstream ductwork and final filter bag can move. The multi-element structured array units were built in our laboratory for each design and the installed filters were manufactured by Quality Filters, Inc. in Robertsdale, Alabama. Pressure drop across the filtration section was

monitored by an Invensys IPO10 differential pressure transmitter. The filter bank was held in place with eight “quick-grip” clamps (Figure 3.9).

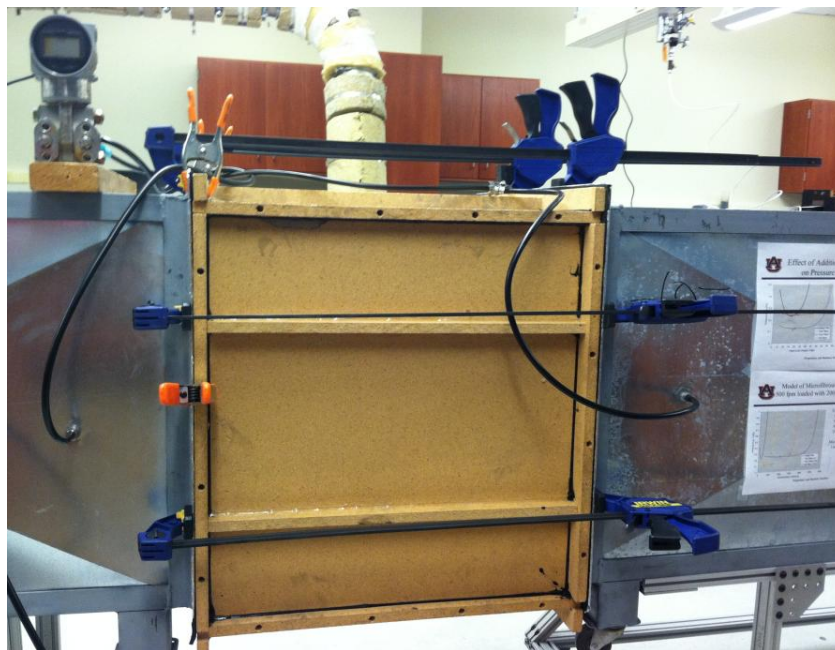


Figure 3.9 Alignment and clamping system

The air passed through the test section and traveled into the downstream ductwork. The downstream duct was an eight-foot long section that housed a second isokinetic probe. The final filter, a 95% efficiency pocket filter (AAF DriPak 2000, purchased from American Air Filter), was located at the end of the duct to capture any challenge particulate that passed through the tested filter. Figure 3.10 is an upstream picture and Figure 3.11 is a downstream picture of the test rig.

The transitions between sections were outfitted with clamping systems to seal the rig and prevent the loss of volumetric flow and challenge dirt. Each section had a 3-inch wide flanged joining plate. Closed cell foam with a thickness of 3/8 inches was added to the width of each flange. The seal between the sections was created by compressing the foam to a minimum of 75% of its original thickness. The compression was created by outfitting the flange with bolt

assemblies and specialized tracks. The extruded aluminum U-channel tracks doubled as second enclosing mechanisms and ran the width of the flange.

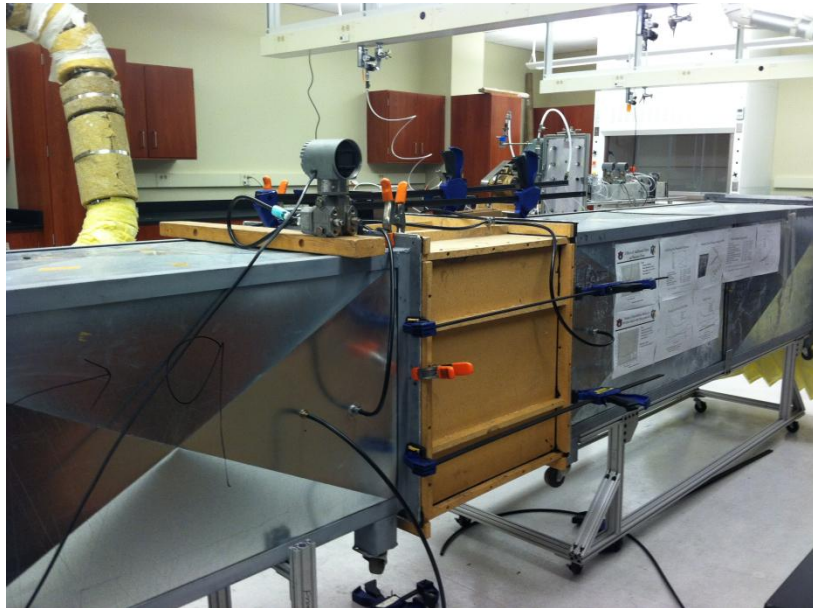


Figure 3.10 Upstream picture of filter test rig

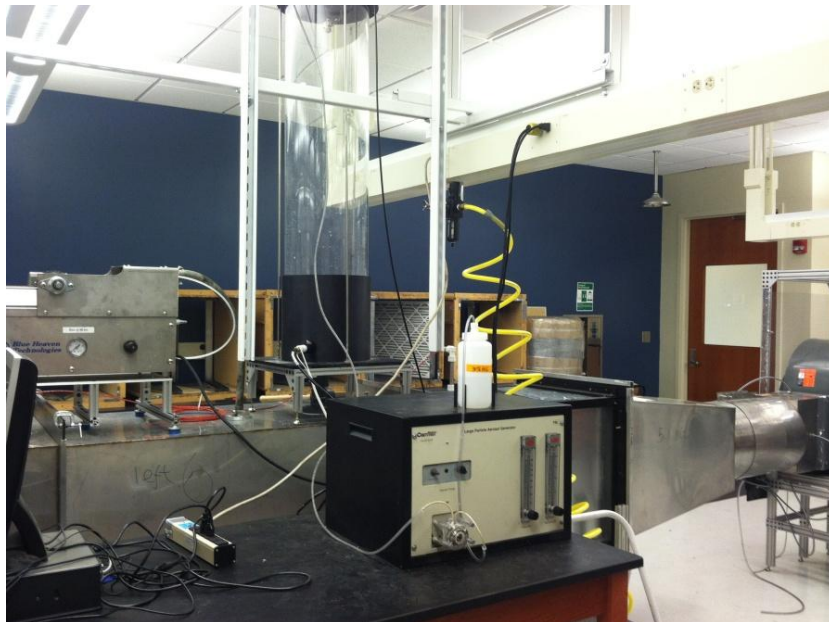


Figure 3.11 Downstream picture of filter test rig

### **3.3 Test Procedure**

The small-scale test rig was designed to measure initial pressure drop and dirt loading for a given media sample. The full-scale test rig was designed to measure initial pressure drop, face velocity, and upstream/downstream particle count as well as dirt loading for a given filtration unit. From these measurements, the filter's performance could be assessed for power consumption, dirt holding capacity, and particle removal efficiency. The following sections describe the general procedure for each test on the full-scale test rig.

#### **3.3.1 Initial pressure drop test**

The initial resistance to flow for a filtration unit was found by measuring the pressure drop across the filtration section over the entire range of frequencies. The filtration unit was first loaded into its appropriate housing unit. The housing was secured within the test rig by bolt assemblies and eight quick-grip clamps. The quick-grip clamps were positioned equidistant from each other around the perimeter of the test section. The room temperature, dew point, and atmospheric pressure were recorded with an Extech 445815 hygrometer and a Conex JDB1 digital barometer. Based on the room temperature, dew point, and barometric pressure, the air density was calculated and found to be approximately constant around  $0.0725 \text{ lb/ft}^3$  ( $1.16 \text{ kg/m}^3$ ).

The pressure transmitters were zeroed and the data acquisition software was initiated before each test. The software recorded a 12-bit signal from each pressure transmitter at a rate of five data points every second. The blower was turned on and allowed to automatically ramp up to 60 Hz over the course of 420 seconds. A ramp rate of 420 seconds was chosen to eliminate trailing effects due to the transmitters not being in equilibrium simultaneously. Once

the blower reached 60 Hz, the system was shut down and the data-logging software was stopped. A text data file was generated from the software that collected data and was manipulated utilizing Microsoft Excel. The transducer's readings, which were recorded as a 1 to 5 volt signal, were changed to the corresponding pressure drop measurements. Face velocity was determined from the orifice plate calibration curve.

### **3.3.2 Removal efficiency test**

A filtration removal efficiency test was performed to identify the ability of filter units to remove particles based on their diameters. The test began by loading the desired filters into the proper filtration unit. The units were then clamped and sealed within the ductwork in the same manner as described for the initial resistance testing. The blower was started and allowed to reach a face velocity of 500 fpm. The TSI nebulizer was then started and the challenge KCl particle concentration was allowed to equilibrate over a five minute period before data collection commenced. Data collection was conducted with a Solair 3100+ particle counter (Figure 3.12). The process was initialized by taking a 20-second sample count from the upstream isokinetic probe. The three-way valve was then switched to allow a sample from the downstream isokinetic probe to be obtained. Before the downstream sample was gathered, the counter performed a 10-second self-purge to remove any remaining particles out of the line from the previous sample. The counter then measured a 20-second count of the downstream particles. The process was repeated until 50 counts were taken from the upstream and downstream probes. The data from the Solair 3100<sup>+</sup> was downloaded via Lighthouse LMS Exchange software. The data was transferred to Microsoft Excel for further processing. The removal efficiency for a given size range was calculated using the Equation 3.1.



Figure 3.12 Picture of Solair 3100<sup>+</sup> particle counter

### 3.3.3 Dirt loading test

Dirt loading tests were performed to artificially age the filter at an accelerated rate in order to evaluate filter performance. The face velocity used during dirt loading test was 500 fpm, which is one of two common set points in the HVAC industry. It was preferred over the second set point 300 fpm, because the larger particles in the ASHRAE dust tend to settle in the ductwork due to longer resident times.

The procedure began by weighing the test filter element(s) with a DENVER Instruments S2002 scale (maximum capacity 2,000 g with a resolution of 0.01g). The filter elements were placed into the tested filter bank unit. Pressure transmitters were zeroed and atmospheric conditions recorded. The blower was initiated and set to deliver 1,985 cfm of house air into the test rig. The clean air was mixed with a known concentration of dirt introduced into the system by the Blue Heaven dust loader. The concentration was fixed by assuring that a uniform height of dirt was evenly distributed across the tray. This was accomplished with a leveling tool shown in Figure 3.13. Challenge dirt was first dried out in an oven at 110 °C (230 °F) for 30 minutes to promote dispersion of the material when subjected to the shearing forces of the Venturi pump. The dirt was then loaded into the feed tray and gradually spread out to achieve a uniform layer.



The tray with a width of 4.5 inches was loaded to a height of 0.25 inches. The chain feed rate was 0.5 inch/min, which represents  $0.56 \text{ in}^3$  of challenge per minute. When picked up and mixed with the 15 cfm of air supplied by the Venturi pump and the 1,985 cfm of clean air, the volumetric concentration delivered to the filter was  $9.76 \times 10^{-6} \text{ m}^3$  of dirt per  $\text{m}^3$  of air. A fully loaded tray ( $272.0 \text{ cm}^3$  volumetric loading dirt) was experimentally determined to weigh 82.9 grams. This equated to an apparent packing density of  $0.30 \text{ g/cm}^3$  of tray volume. The mass load to the rig was computed to be  $2.77 \text{ g/min}$ . Data acquisition took place by turning on the pressure transmitter when the dirt loader was turned on. There was a one minute lag between the time the dirt load started and when the tray delivered the first amount of challenge dirt to the Venturi pump. This lag could easily be identified and removed from the gathered data.

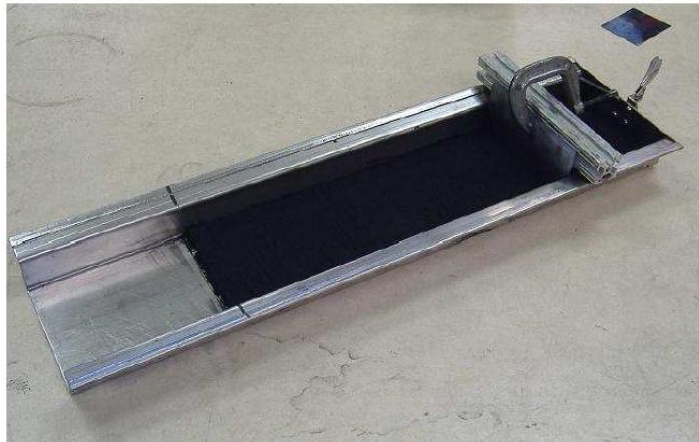


Figure 3.13 Loading tray with leveling tool (Sothen, 2009)

Although the rig loaded the filter at a uniform rate, the blower's volumetric output steadily dropped as the static head in the system increased due to the filter's loading. In order to keep the blower set at 1,985 cfm, the frequency drive was manually incremented to maintain a set point resistance across the orifice plate. The rate at which the filter loaded was quite low; thus, it was very easy to maintain the flow within  $9.44 \times 10^{-3} (\pm 20 \text{ cfm})$ .

The filter unit was aged with ASHRAE dirt until a resistance of 1.0 " H<sub>2</sub>O across the filter unit was achieved. The test was stopped and the filter unit was removed and weighed to determine the amount of dirt loaded. It was possible to periodically pull and weigh the filter, but it was determined to be unnecessary for data processing since the system loads at a uniform rate. Periodically pulling the filter introduces errors into the data collection due to potential disturbances of the cake formation on the filter's surface. Additionally, there was the risk of dropping the filter and ruining the tests.

## **Chapter 4 Fundamental Design of Microfibrous Materials as Pleated Filter**

### **Media**

#### **4.1 Introduction**

Utilization of microfibrous entrapped sorbent media in air filtration can be a promising method to combine particle filtration and gas phase filtration in one unit. However, a high pressure drop created by small, entrapped sorbent particles and a low saturation capacity due to the relatively low thickness of the media will hamper its use as filter media (Harris et al., 2001). A pleated filter design can improve pressure drop performance and enhance capacity of microfibrous materials. The performance enhancements are due to the increased available media area by transforming the flat material into a three-dimensional, corrugated structure. The additional area extends the capacity of a filter as well as lowers the pressure drop by slowing down the velocity through the porous material. However, the addition of each pleat introduces a new source of resistance due to increased surface-fluid friction. The reduction in pressure drop through the media is steadily counteracted by a rise in the flow resistance because of increased friction in the pleat. Due to the exchange of media-induced flow resistance loss for pleat-induced pressure losses, a pleated filter will experience a minimal resistance corresponding to an optimal pleat count and media area (Figure 4.1) (Sothen, 2009). Finding the optimal pleat count for a given dimension is the primary design problem for a pleated filter made of microfibrous media.

By applying fundamental fluid dynamic equations and empirical data, Sothen et al. (2008) developed a semi-empirical pressure drop model which can predict initial flow resistance across a 20" × 20" pleated filter with a depth of 4 inches or less at any face velocity. The model can be used as a design tool to predict minimum initial pressure drop, maximum filtration area, and preferred media properties with respect to permeability versus thickness. In theory, this model should be applicable to any pleated filters with known media characterization (such as media thickness, media constants). I will apply this model in designing a dual-functional pleated filter made of microfibrous media entrapped activated carbon particles. In addition, the impacts of design factors (such as pleat count, filter depth, media permeability and media thickness) on initial pressure drop will also be investigated based on the model simulation results.

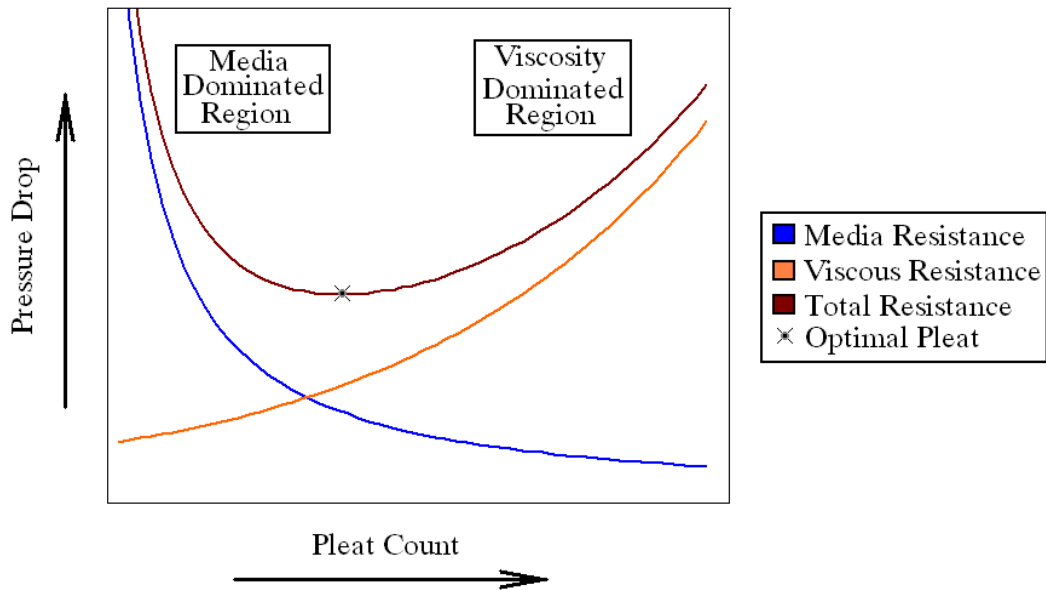


Figure 4.1 Typical “U” pleating curve (Sothen, 2009)

## 4.2 Model Description

The pathway of air flow through a pleated filter was proposed to consist of seven regions of various cross-section areas (Figure 4.2) (Sothen and Tatarchuk, 2008). Therefore, the

overall pressure drop across a single pleated filter was modeled as a summation of seven individual resistances, which can be expressed as the following formulas:

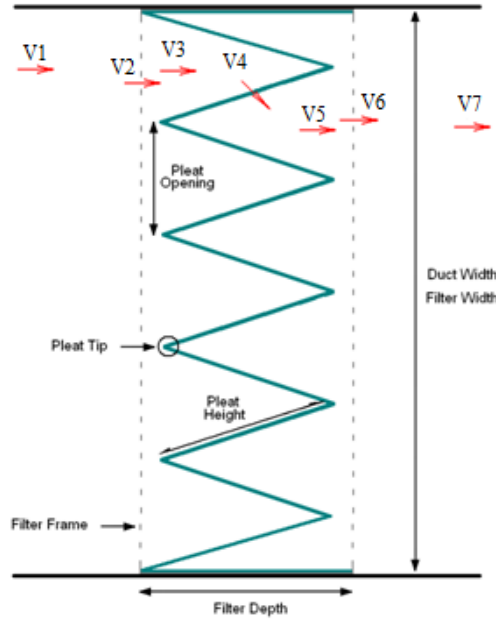


Figure 4.2 Proposed flow pattern

$$\Delta P_{total} = \sum \Delta P_i = \Delta P_1 + \Delta P_2 + \Delta P_3 + \Delta P_4 + \Delta P_5 + \Delta P_6 + \Delta P_7$$

Where

- |  |  |
|--|--|
| 1) Across front grating:                     | $\Delta P_1 = \frac{1}{2} \rho [(V_2^2 - V_1^2) + K_G V_2^2]$    |
| 2) Flow from grating to pleat inlet:         | $\Delta P_2 = \frac{1}{2} \rho [(V_3^2 - V_2^2) + K_C V_3^2]$    |
| 3) Flow from pleat inlet to media surface:   | $\Delta P_3 = \frac{1}{2} \rho [(V_4^2 - V_3^2) + K_{P1} V_3^2]$ |
| 4) Flow through media:                       | $\Delta P_4 = A V_4 + B V_4^2$                                   |
| 5) Flow from media surface to pleat outlet:  | $\Delta P_5 = \frac{1}{2} \rho [(V_5^2 - V_4^2) + K_{P2} V_5^2]$ |
| 6) Expansion from pleat outlet into grating: | $\Delta P_6 = \frac{1}{2} \rho [(V_6^2 - V_5^2) + K_E V_5^2]$    |
| 7) Across back grating:                      | $\Delta P_7 = \frac{1}{2} \rho [(V_7^2 - V_6^2) + K_G V_6^2]$    |

Using the equation of continuity, the series could be simplified by replacing all downstream velocity with their reciprocal upstream velocities. The seven terms could be summed and rearranged into the following equation:

$$\Delta P_{total} = \frac{1}{2} \rho [(2K_G)V_2^2 + (K_C + K_E + K_P)V_3^2] + A V_4 + B V_4^2 \quad (4.1)$$

Here,  $K_{p1}$  and  $K_{p2}$  was lumped into one parameter  $K_p$ , since the individual contributions of  $K_{p1}$  and  $K_{p2}$  could not be separated and analyzed experimentally due to the upstream and downstream pleat symmetry. In the equation, the first four terms represented the geometric contribution, and the last two terms denote the media influence. The coefficients  $K_C$ ,  $K_E$  and  $K_G$  can be computed through Eq. 4.2, Eq. 4.3 and Eq. 4.4 (Idelchik, 1994).

$$K_C = \frac{1}{2} \left(1 - \frac{A_{Free}}{A_{Total}}\right)^{0.75} \quad (4.2)$$

$$K_E = \left(1 - \frac{A_{Free}}{A_{Total}}\right)^2 \quad (4.3)$$

$$K_G = \left(1.707 - \frac{A_{Free}}{A_{Total}}\right)^2 \left(\frac{A_{Free}}{A_{Total}}\right)^2 \quad (4.4)$$

$A_{Free}$  and  $A_{Total}$  stand for the free area and total area, respectively. An accurate and universal coefficient of friction formula for  $K_p$  was determined by testing a multitude of filter designs (Sothen, 2009), which can be described in the following equation

$$K_p = 0.07903 \left(\frac{F_{HD}}{F_D}\right) \left(\frac{1}{\beta}\right)^{1.29} \quad (4.5)$$

$$F_{HD} = \frac{2F_H F_D}{F_H + F_D} \quad (4.6)$$

Where  $F_{HD}$  = filter hydraulic diameter, m

$F_H$  = filter height, m

$F_D$  = filter depth, m

$\beta$  = pleat pitch, rad

In order to make the above equation expression easier to understand, the dimensions of filter and pleat are illustrated as follows.

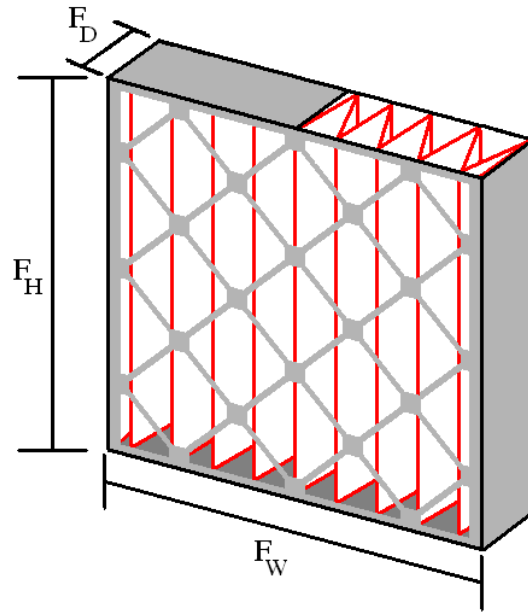


Figure 4.3 Illustration of filter dimensions (Sothen, 2009)

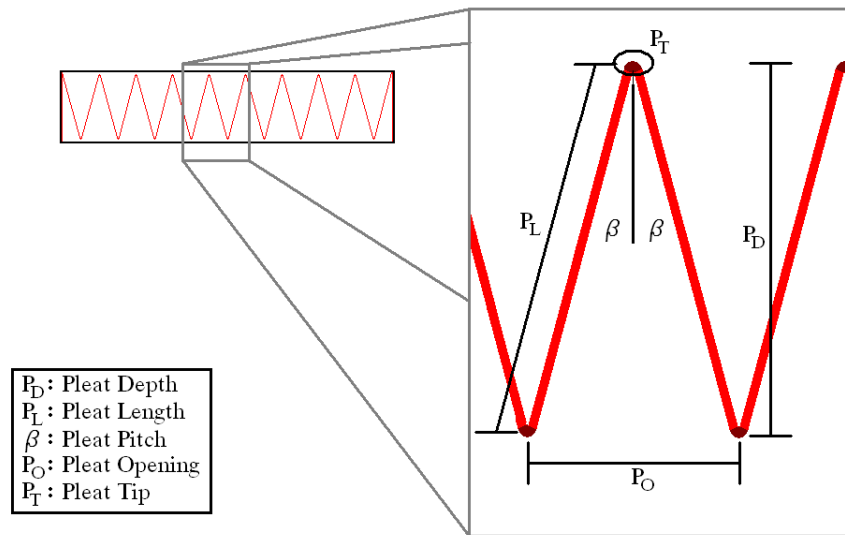


Figure 4.4 Illustration of pleat dimensions (Sothen, 2009)

### 4.3 Media Preparation

Polymeric microfibrous material was selected as model media in this study. The microfibrous media (MFM) is composed of 19  $\mu\text{m}$  diameter bicomponent (linear low density polyethylene on polyethylene terephthalate) polymer fibers and 50~80 mesh (180~300 micron)

activated carbon particles (ACPs). MFM is prepared by a wet lay process followed by sintering at a chosen temperature. The first step was to create a homogeneous uniform suspension of polymer fibers by using a blender to disperse 3.15g 19  $\mu\text{m}$  diameter bicomponent polymer fiber in about 900mL water. In another blender, 7g of hydroxyl ethyl cellulose (HEC) was added to 1 L of water, then 1 mL of 0.1 M NaOH solution was added to adjust the pH of the HEC solution to 8~9. This HEC solution is merely a viscous solution for use in the wet lay process to ensure the even distribution of particles in the final sheet.

The two resulting suspensions were transferred into a 8"  $\times$  8" head box of paper making equipment with approximately 8 L of water (Figure 4.5). 5.85g ACPs (ACP) were then added to the head box while stirring the contents with a plunger. Then, the excess water in the suspension was drained quickly. The ACPs became entrapped in the fiber matrix as they settled along with the microfibers to form a thin sheet on the bottom screen in the paper making equipment. The pre-form was carefully removed and sintered in air inside a 450 K oven for 5 min, then dried further at 373 K for 48hrs. The created sheet has about 200  $\text{g}/\text{m}^2$  of basis weight with 65% carbon loading, which is referred to MFM No.1. Varying the weight ratio of polymer fibers and of the ACPs and the total weight, the other two samples are made by the same procedure. They are referred to MFM No.2 and MFM No.3. The MFM No.2 basis weight is about 300  $\text{g}/\text{m}^2$  with 70% carbon loading and the MFM No. 3 basis weight is approximately 400  $\text{g}/\text{m}^2$  with 75% carbon loading. Table 4.1 listed the compositions of polymer fibers and the ACPs in the three MFM samples. The tested media samples were prepared by punching 2-inch diameter discs from each 8"  $\times$  8" media sheet. The MFM No.2 samples are shown in Figure 4.6.



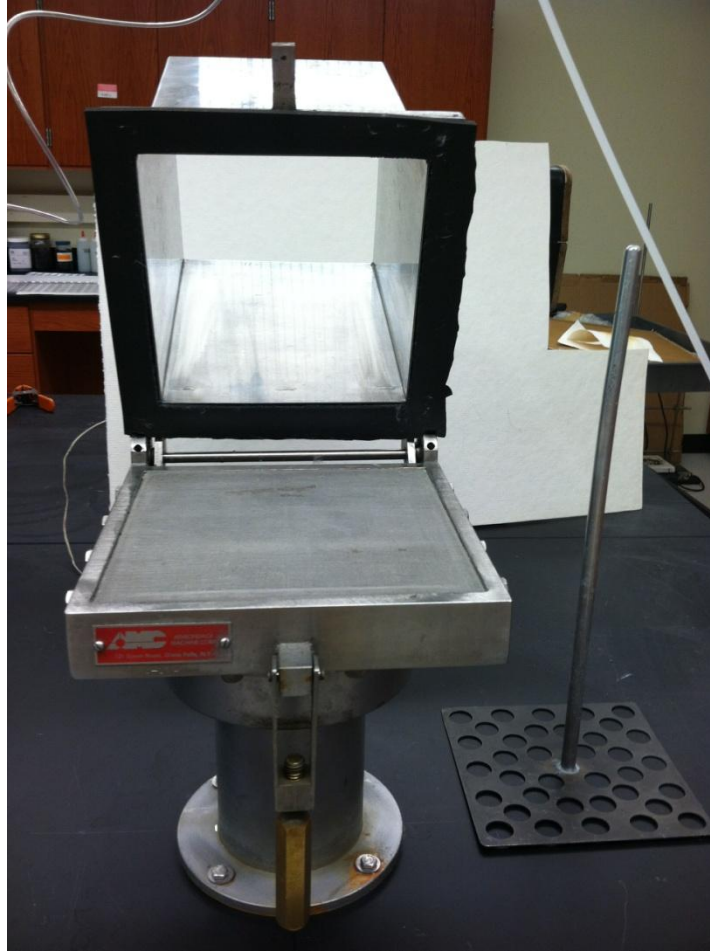


Figure 4.5 Picture of 8" × 8" sheet making equipment in our lab



Figure 4.6 Picture of MFM media sample No. 2

**Fiber:** 19  $\mu\text{m}$  diameter bicomponent polymer fiber (linear low density polyethylene on polyethylene terephthalate)

**Particle:** 180 ~300 micron activated carbon particles

Table 4.1 Composition of three MFM samples

<b>Media</b>	<b>Polymer Fiber</b>	<b>ACPs</b>	<b>Basis Weight</b>	<b>Carbon Percentage</b>
<b>(-)</b>	<b>(g)</b>	<b>(g)</b>	<b>(g/m<sup>2</sup>)</b>	<b>(wt %)</b>
MFM No. 1	3.15	5.58	200	65
MFM No. 2	3.95	9.25	300	70
MFM No. 3	4.13	12.38	400	75

#### 4.4 Media Thickness and Constants

The media thickness was measured by using the equipment provided by IntraMicron, Inc. (Figure 4.7). Each sample was measured three times and the average value was selected for model simulation.

The media constants A and B should be unique and would vary with the filter media types. They were determined by an experimental approach that is the same as the method Sothen (2009) employed. The schematic for the media test rig is illustrated in Figure 4.8. A media test rig was constructed to measure pressure drop performance across a media sample (Figure 4.9). The rig was composed of 1-inch diameter circular duct powered by house air at 100 psig. Airflow to the rig was controlled by two Omega rotameters. Rotameter 1 (Model No.: Fl. DA 3407G) had a flow range of 0~50 SCFH with a precision of 1 SCFH. Rotameter 2 (Model No.: Fl. DA 3208C) had a flow range of 0~140 SCFH with a precision of 10 SCFH. These two rotameters were connected in series to produce a stable, controllable volumetric flow between 0 and 160 SCFH. This correlated to a maximum superficial velocity of 430.5 fpm within the 1-inch test rig. The duct length to diameter ratio (48-to-1) was made sufficiently large in order to ensure that there were no entrance effects. A media sample was held in place by two

plates tightened together by four nut and bolt assemblies. A 12-inch outlet section was located downstream from the media sample to prevent additional pressure loss due to a sudden expansion out of the tube.

Pressure drop measurements across the media sample were obtained with an Omega differential pressure transmitter (Model No.: PX154-0d0DI). This transmitter was connected to two pressure taps that were located five inches upstream and five inches downstream from the media sample. The taps had a 1/8-inch diameter and were drilled flush with the inner tube diameter in order to prevent increased friction. The pressure transmitter had a range of -1.0 to 10" H<sub>2</sub>O with a resolution of 0.001" H<sub>2</sub>O.

Pressure drops were measured three times at each volumetric flow rate setting point. An average value was selected to form the media resistance curve. The media constants were determined from a second order polynomial fit. Table 4.2 summarizes the characterization of three different MFM samples. Figure 4.7 show the media resistance curve for the MFM samples. As depicted in Figure 4.10, MFM No.3 had a much higher pressure drop than MFM No.2 and No.1.

Equation 4.7 denotes that the pressure drop of a media is directly proportional to thickness (h) and packing density (c). It possesses an inverse quadratic relationship to fiber radius (R) (Brown 1993).

$$\Delta P = 4\eta chV / R^2\xi \quad (4.7)$$

Because it was the thickest media and had the highest carbon loading, MFM No.3 media had the highest flow resistance. A higher pressure drop is undesirable, because this causes larger energy consumption in a HVAC system (Arnold et al., 2005). This problem can be partially alleviated by folding and packaging the media into a pleated filter arrangement. However, pleat numbers,

pleat depth and media thickness should be optimized in order to get the best filtration performance.



Figure 4.7 Picture of thickness measurement equipment

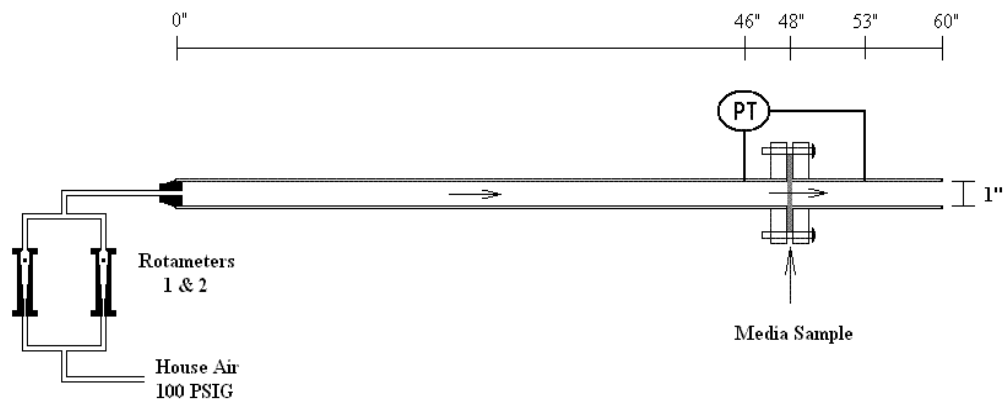


Figure 4.8 General schematic of media test rig (Sothen, 2009)

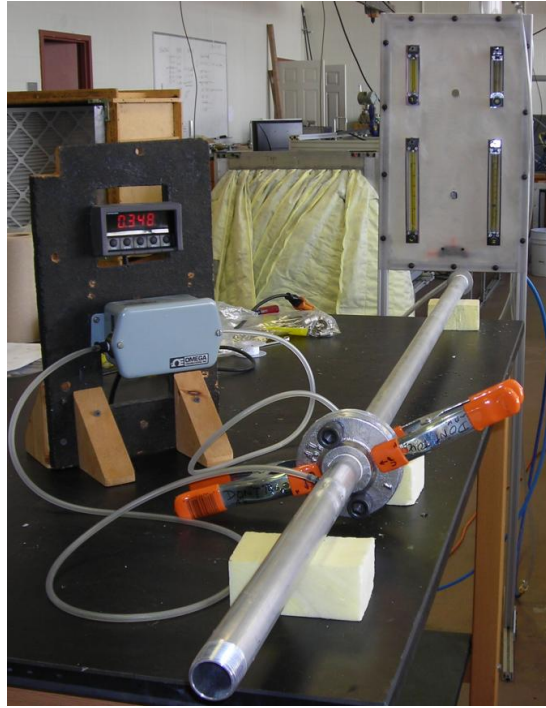


Figure 4.9 Picture of media test set-up

Table 4.2 Summary of MFM media characterization

<b>Media</b> (-)	<b>Thickness</b> (in)/[mm]	<b>A</b> ( " H <sub>2</sub> O•min/ft )	<b>B</b> ( " H <sub>2</sub> O•min <sup>2</sup> /ft <sup>2</sup> )	<b>R<sup>2</sup></b> (-)
MFM No. 1	0.0717/[1.82mm]	$4.0 \times 10^{-4}$	$7.0 \times 10^{-7}$	0.9987
MFM No. 2	0.1110/[2.82mm]	$9.0 \times 10^{-4}$	$10.0 \times 10^{-7}$	0.998
MFM No. 3	0.1516/[3.85mm]	$56.2 \times 10^{-4}$	$10.0 \times 10^{-7}$	0.9988

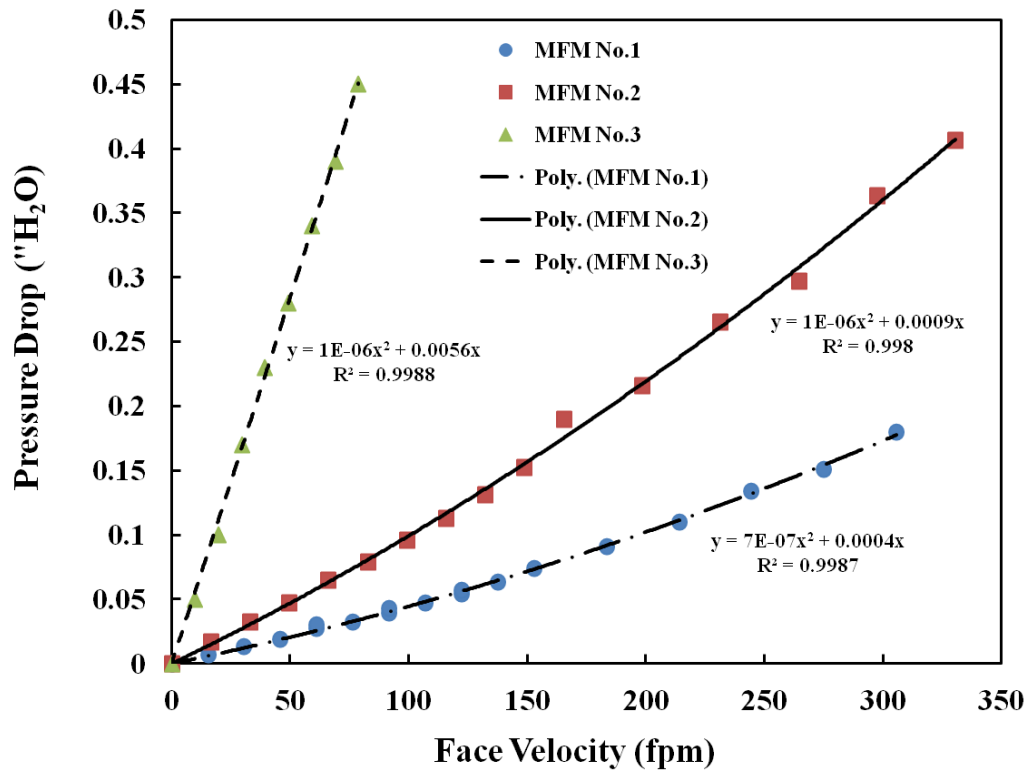


Figure 4.10 Media resistance curve for three MFM samples

#### 4.5 Application of Model for MFM Filters Design

Sothen's semi-empirical pressure drop model (2009) was used to predict pressure drop across the MFM pleated filters with a cross section of 24" × 24" in this section. In addition, the effect of design parameters including pleat number, filter depth, media thickness on pressure drop was investigated by applying this semi-empirical model.

##### 4.5.1 Effect of pleat number

Pleat number is an important design parameter for air filter. As presented by researchers such as Sothern (2009), Chen et al. (1996), Del Fabbro et al. (2002), Tronville and Sala (2003), and Caesar and Schroth (2002), there is an optimal pleat count corresponding to a minimal pressure drop for a pleated filter due to the trade-off of media-induced pressure loss for

viscous-induced pressure loss. To verify my preliminary results, I did initial pressure drop tests on commercial MERV 8 particle filters (purchased from Quality Filters, Inc., Robertsdale, AL) with different depths. The experimental results were plotted in Figure 4.11. The plotted results revealed “U” curves and an optimal pleat number corresponding to a lowest obtainable resistance for MERV 8 filters with each depth.

The actual dimensions and pleat numbers of tested filters are listed in Table 4.3. The data in the parenthesis stand for the nominal dimensions of the filters.

According to previous researchers’ studies and my experimental results, pleated filters made of MFM would seem to have an optimal pleat count corresponding to the lowest initial pressure drop. To verify the hypothesis and determine the optimal pleat count for a MFM filter, the prediction of initial pressure drop for MFM pleated filters with different pleat counts was conducted.

MFM No.1 was selected as the model media due to the lowest pressure drop among the three prepared samples. Assuming this media has been made into a filter with the dimension of 24" × 24" × 4", the initial pressure drop at different face velocities was computed. Figure 4.12 represents the effect of pleat count on the initial pressure drop for pleated filters made of MFM No.1. As shown in this figure, MFM filter with 5 pleats had the highest initial pressure drop, while a MFM filter with 20 pleats had the lowest initial pressure drop for face velocity in the range of 0~900 fpm. Although a MFM filter with 40 pleats has more available filtration area, it had a higher initial pressure drop than the 20-pleat MFM filter. It can conclude that there is an optimal pleat count for MFM pleated filters.

Table 4.3 Critical parameters of filters employed

<b>Filter</b>	<b>Depth</b>	<b>Width</b>	<b>Height</b>	<b>Pleat Count</b>
1	0.75" (1")	23.8125" (24")	23.8125" (24")	20
2	0.75" (1")	23.8125" (24")	23.8125" (24")	28
3	0.75" (1")	23.8125" (24")	23.8125" (24")	36
4	0.75" (1")	23.8125" (24")	23.8125" (24")	44
5	0.75" (1")	23.8125" (24")	23.8125" (24")	52
6	0.75" (1")	23.8125" (24")	23.8125" (24")	60
7	1.75" (2")	23.375" (24")	23.375" (24")	15
8	1.75" (2")	23.375" (24")	23.375" (24")	20
9	1.75" (2")	23.375" (24")	23.375" (24")	25
10	1.75" (2")	23.375" (24")	23.375" (24")	30
11	1.75" (2")	23.375" (24")	23.375" (24")	35
12	1.75" (2")	23.375" (24")	23.375" (24")	40
13	3.5" (4")	23.375" (24")	23.375" (24")	10
14	3.5" (4")	23.375" (24")	23.375" (24")	16
15	3.5" (4")	23.375" (24")	23.375" (24")	22
16	3.5" (4")	23.375" (24")	23.375" (24")	28



### U Curve for Single Filters with Different Depths (24"×24")

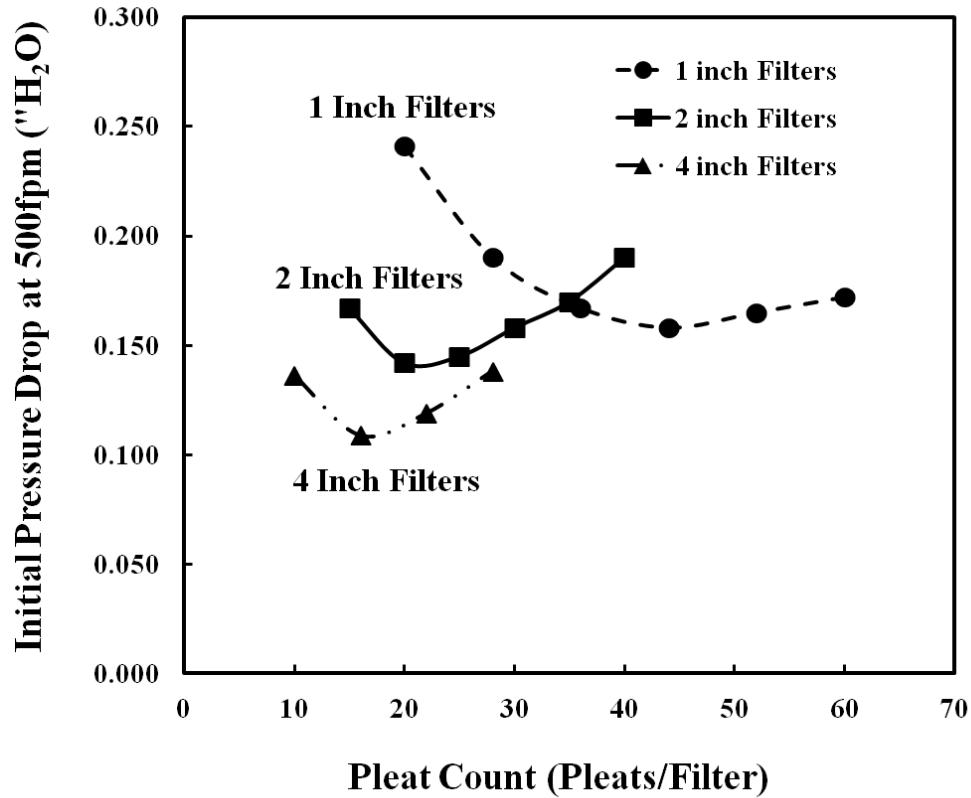


Figure 4.11 Pleating curves of commercial MERV 8 filters with different depth

Since HVAC filters often operate at 500 fpm face velocity, initial pressure drop across pleated filters made of MFM sample No.1 with different depth (1", 2", 4") at 500 fpm were calculated. As shown in Figure 4.13, there is an optimal pleat number for filter with each depth. For a 1" pleated filter, the optimal pleat number is 57 and the minimum initial pressure drop is 0.178" H<sub>2</sub>O. For a 2" pleated filter, the optimal pleat number is 28 and the minimum initial pressure drop is 0.146" H<sub>2</sub>O. For a 4" pleated filter, the optimal pleat number is 20 and the minimum initial pressure drop is 0.131" H<sub>2</sub>O. The results are summarized in Table 4.4. As shown in this table, when the filter depth is increased, the optimal pleat number decreases and

the initial pressure drop also decreases. This decrease results from the increased filtration area as the filter depth increases.

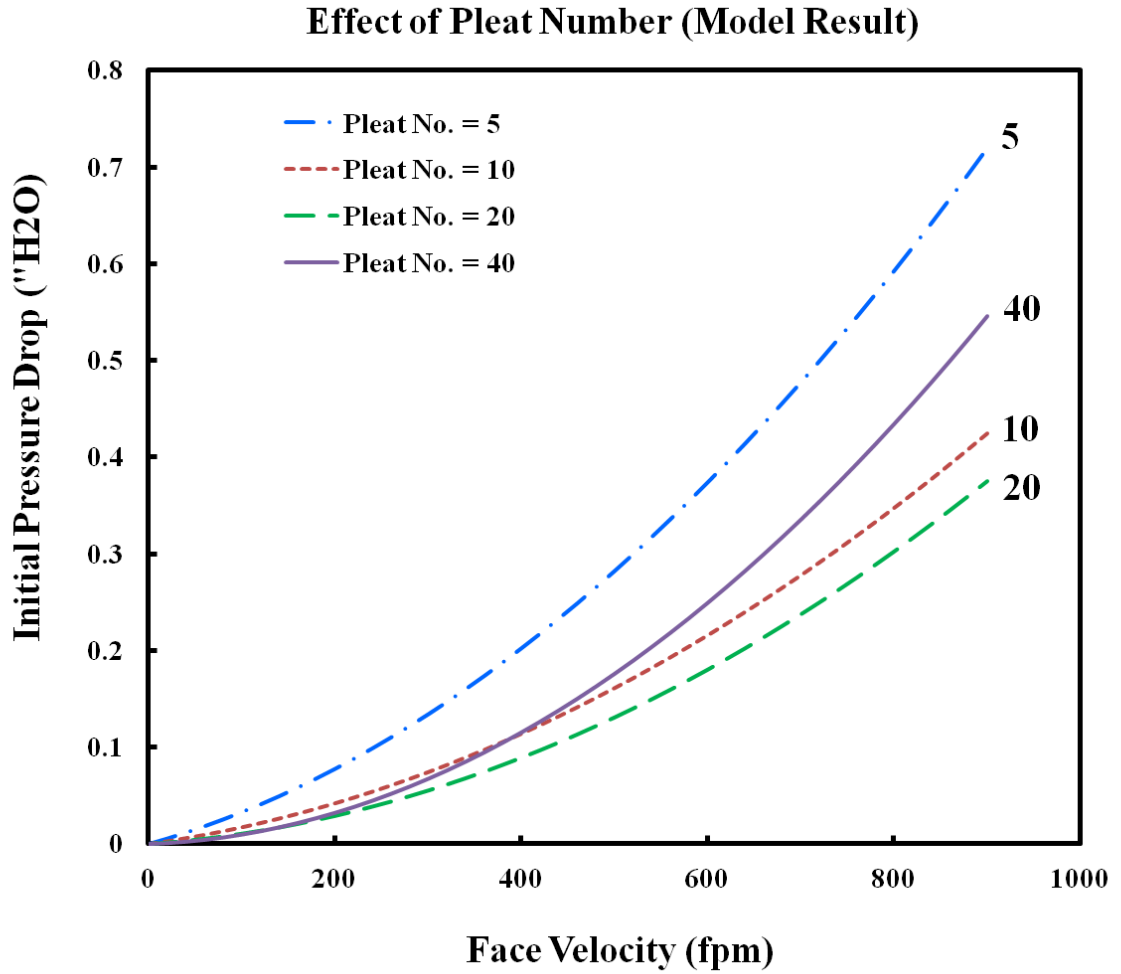


Figure 4.12 Effect of pleat numbers on initial pressured drop for MFM No.1 pleated filters

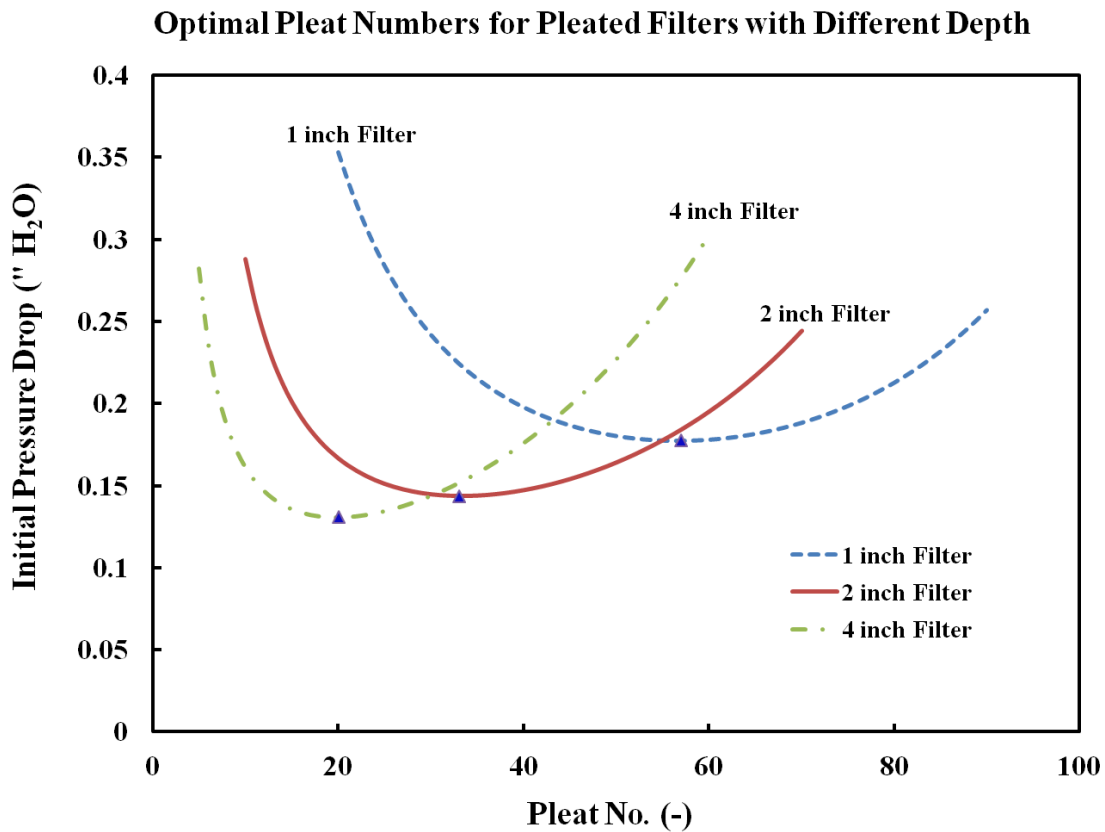


Figure 4.13 Optimal pleat numbers for MFM No.1 pleated filters with different depth

Table 4.4 Optimal pleat numbers and corresponding filtration area for MFM No.1 pleated filters with different depth

<b>Filter Depth (inch)</b>	<b>Opt Pleat No. (-)</b>	<b>Filtration Area (ft<sup>2</sup>)</b>	<b>Min Pressure Drop at 500fpm (inches H<sub>2</sub>O)</b>
1	57	13.88	0.178
2	28	15.91	0.146
4	20	22.73	0.131

#### 4.5.2 Effect of filter depth

Commercial pleated filters are usually made in 1", 2" and 4" depths. However, the effect of filter depth on filtration performance is not clearly understood. I will use MFM No.1 as the modeled media to investigate the effect of filter depth on initial pressure drop by applying

Sothen's semi-empirical pressure drop model. Filter cross section was fixed at 24" × 24" and the pleat number was fixed at 30.

Figure 4.14 presents the simulated pressure drop results of a pleated MFM filter with different depth at face velocity in the range from 0 to about 900 fpm. As shown, the pressure drop of a 2" deep filter is the lowest while the pressure drop of a 1" deep filter is the highest. The pressure drop of a 4" deep filter is between these two. In addition, the pressure drop difference between the 1" deep filter and 4" deep filter is much larger than that between the 2" deep filter and 4" deep filter. This also can be viewed in Figure 4.15 which shows the initial pressure drops at 500 fpm for 1", 2" and 4" MFM filters at the same dimension and the same pleat numbers. The explanation for this counterintuitive situation is based on the geometric structures of the pleats inside different deep filters. As depicted in Figure 4.16, the deeper the pleats are, the smaller the pleat pitches are and the sharper the pleat angles are. Hence, the more effective filtration areas of the 4" deep filter are blocked, so the pressure drop would be larger than that which would be expected. Therefore, the pressure drops of the 4" deep filter are larger than the pressure drops of the 2" deep filter.

The simulated pressure drop results show that the 2" deep filter would give the lowest pressure drop when other design parameters (dimension, pleat number, media thickness and constants) are kept the same, so the optimal filter depth is 2 inches.

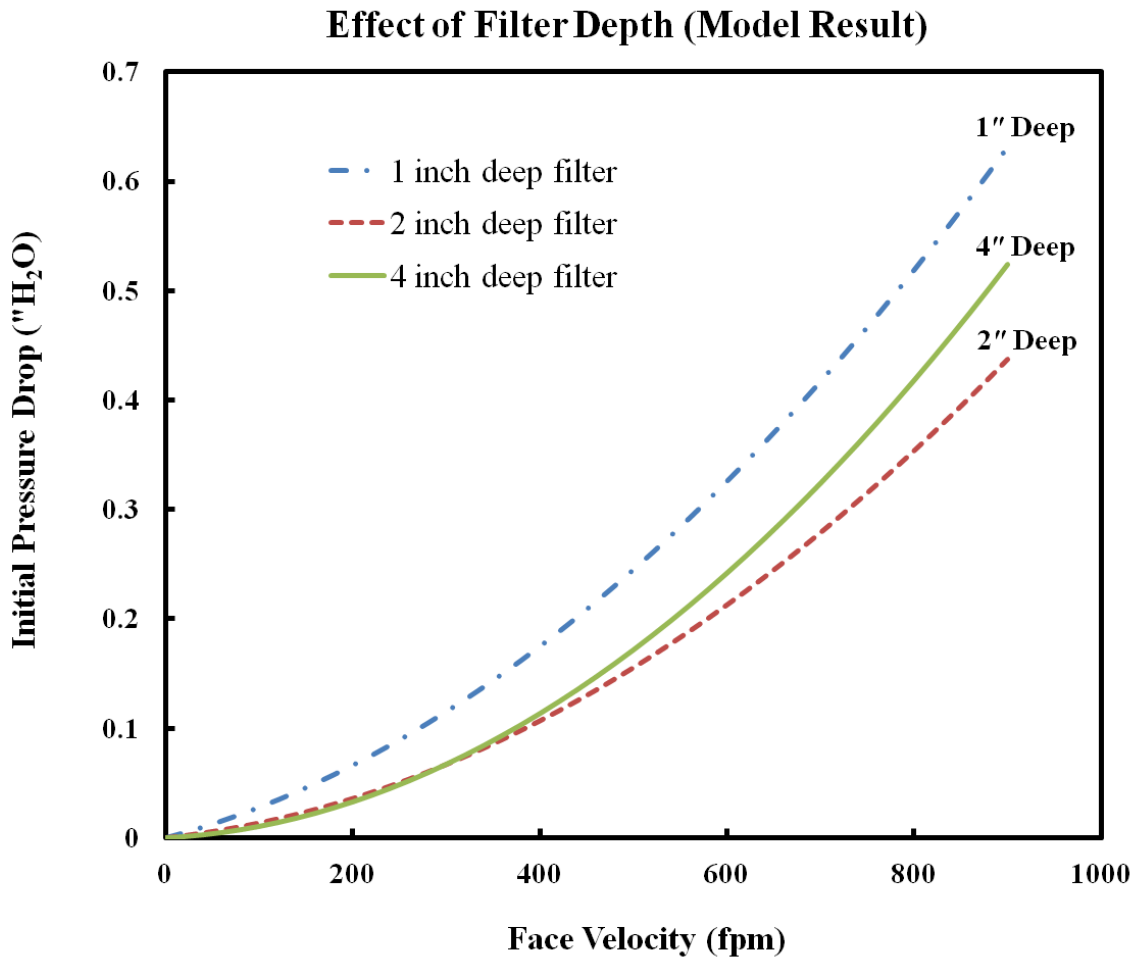


Figure 4.14 Effect of filter depth on initial pressure drop for MFM No.1 pleated filters

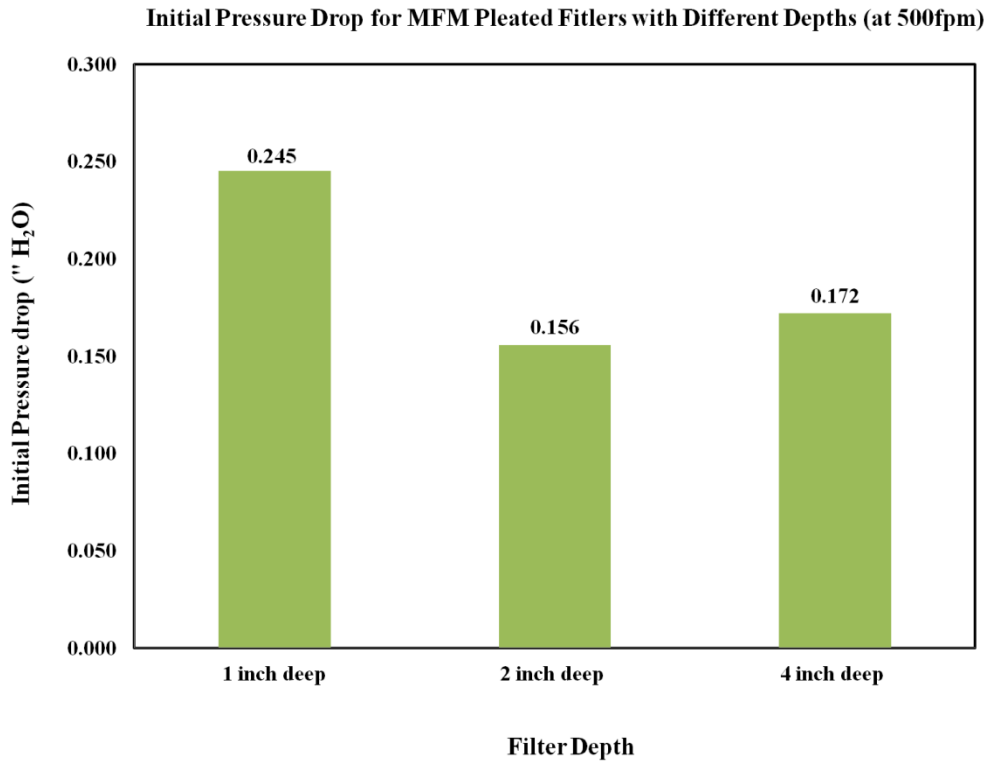


Figure 4.15 Initial pressure drop of MFM No.1 pleated filters with different depth at 500 fpm

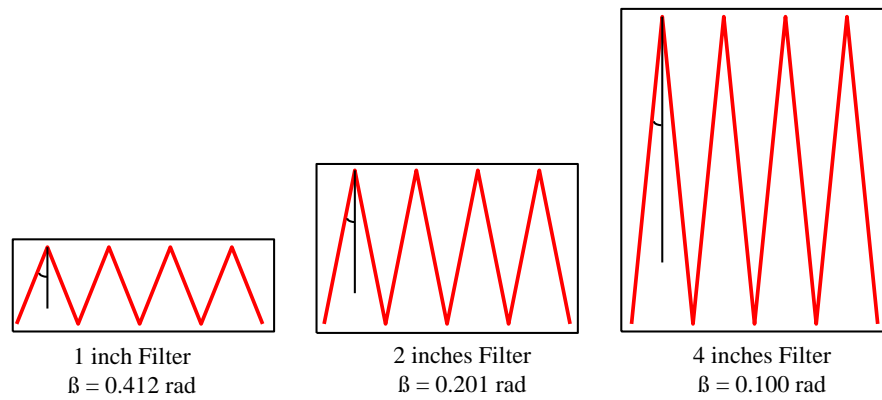


Figure 4.16 Comparison of pleat pitch of 1", 2" and 4" filters

### 4.5.3 Effect of media thickness

As shown by Equation 4.7, the pressure drop of a media is directly proportional to its thickness. Thus media thickness is a very important design parameter. The corollary is that the thinner the media is, the lower the pressure drop would be at the same face velocity. MFM thickness can be adjustable by compression or by thermal bonding after the wet lay process. By using the Sothen's model, the effect of media thickness on pressure drop for pleated MFM filters can be studied.

A new fluffy microfibrinous media (MFM C) was prepared by the method described in Section 4.3. The media thickness was measured to be 0.1181 inch (3 mm). Subsequently the media was compressed to different desired thicknesses. The target thicknesses are 0.0472 inch (1.2 mm) and 0.0787 inch (2 mm) and were referred to as MFM A and MFM B, respectively. In addition, two layers of MFM C were thermally bonded together to form a thicker media (MFM D). The media thickness and constants were obtained by the methods described in Section 4.4. Table 4.5 listed the typical parameters for the above prepared media samples.

Table 4.5 Summary of normal and treated MFM samples characterization

<b>Media</b>	<b>Thickness (in) / [mm]</b>	<b>A (<math>" \text{H}_2\text{O} \times \text{min} / \text{ft}</math>)</b>	<b>B (<math>" \text{H}_2\text{O} \times \text{min}^2 / \text{ft}^2</math>)</b>	<b>R<sup>2</sup> (-)</b>
MFM A (1 layer)	0.0472 / [1.2 mm]	$8 \times 10^{-4}$	$1.00 \times 10^{-6}$	0.9998
MFM B (1 layer)	0.0787 / [2 mm]	$7 \times 10^{-4}$	$2.00 \times 10^{-6}$	0.9981
MFM C (1 layer)	0.1181 / [3 mm]	$10 \times 10^{-4}$	$1.00 \times 10^{-6}$	0.9995
MFM D (2 layer)	0.2362 / [6 mm]	$12 \times 10^{-4}$	$2.00 \times 10^{-6}$	0.9995

Figure 4.17 presents the predicted initial pressure drop results as the media thickness are altered. The predictions are made for a filter with 30 pleats with the dimension of 24" × 24" × 2". As seen, when the media thickness decreased, the initial pressure drop reduced. When two

layers of uncompressed MFM that were thermally bonded together were utilized, the initial pressure drop increased dramatically. Therefore, media thickness plays an important role in the pressure drop across a filter. As the manufacturing procedure and treatment methods permit, making the media as thin as possible would be desirable.

Figure 4.18 shows the predicted optimal pleat numbers for MFM pleated filters with different thickness. The predictions are made for a single 24" × 24" × 2" filter at 500 fpm with various pleat counts. As seen, the overall effect is an increase in the minimum pressure drop as the media thickness increases, and the optimal pleat number decreases when the media thickness is increased. Table 4.6 lists the optimal pleat numbers and corresponding achievable minimum initial pressure drops for the model filters. As shown in this table, using MFM A instead of MFM C can reduce the initial pressure drop by about 25%. In addition, using MFM A instead of MFM C can increase media area by about 53%. Therefore, there are some advantages for using compressed media to make pleated filters.

One of the advantages of using compressed media is to reduce initial pressure drop and save energy. The second advantage is to increase available filtration area and sorbent loading capacity. For example, a filter constructed using a 1.2 mm thick media instead of 3 mm would have 23 ft<sup>2</sup> of media area versus 15 ft<sup>2</sup> into which more ACPs could be packed. The increased ACPs loading would result in an improved removal efficiency of gaseous contaminants.



### Effect of Media Thickness (Model Result)

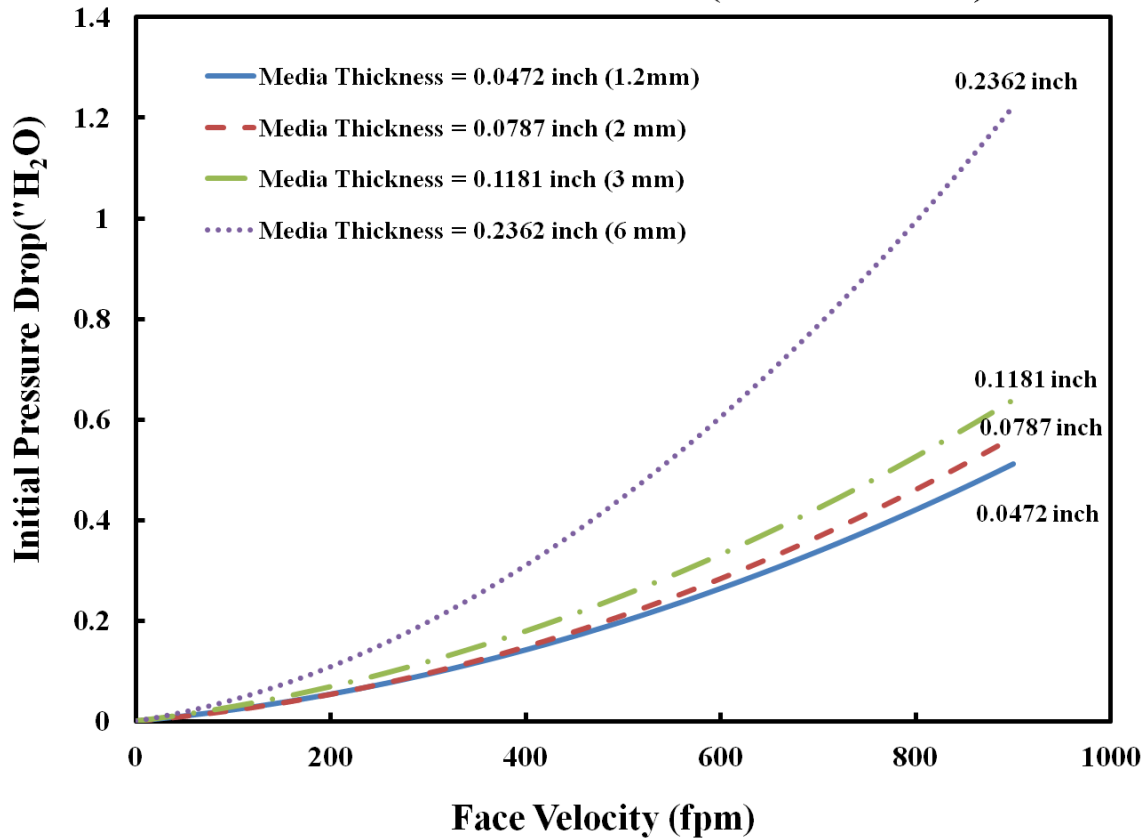


Figure 4.17 Effect of media thickness on initial pressure drop for MFM filters

Table 4.6 Model predicted optimal pleat numbers different MFM filters at 500 fpm

Media (-)	Thickness (in) / [mm]	Opt. Pleat No. (-)	Minimum Initial Pressure Drop (\" H <sub>2</sub> O)
MFM A (1 layer)	0.0472 / [1.2 mm]	40	0.189
MFM B (1 layer)	0.0787 / [2 mm]	36	0.205
MFM C (1 layer)	0.1181 / [3 mm]	32	0.250
MFM D (2 layer)	0.2362 / [6 mm]	24	0.390

**Optimal Pleat No. for Pleated MFM Filters with Various Media Thickness**

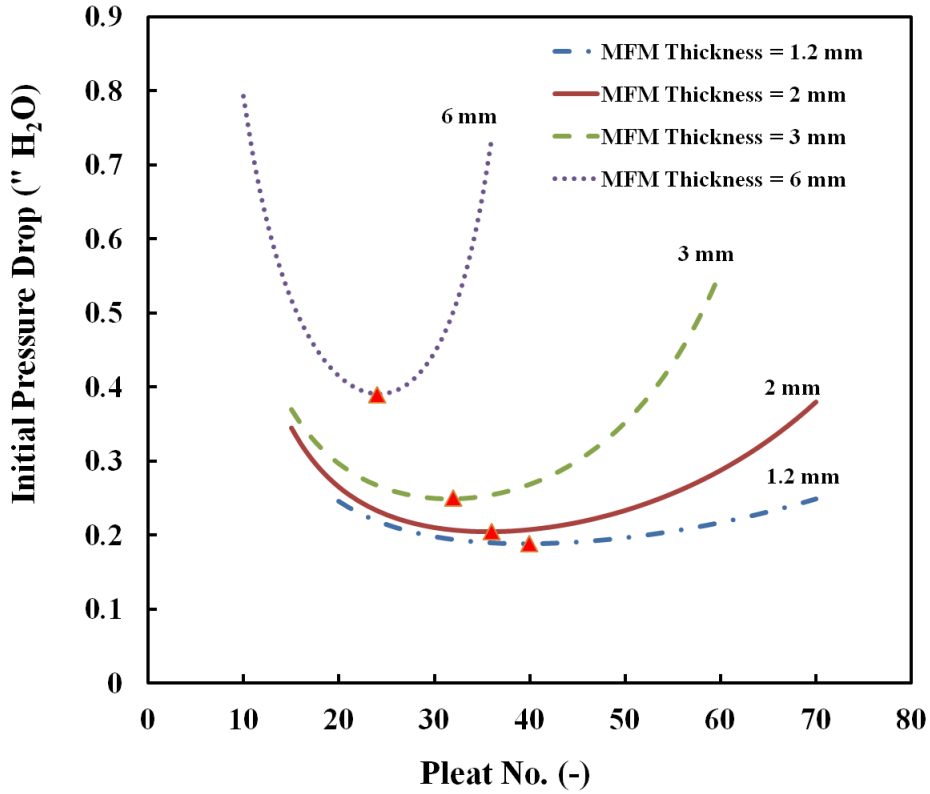


Figure 4.18 Optimal pleat numbers for filters with different media thickness at 500 fpm

#### 4.5.4 Effect of media constants

As characterization parameters, media constants A and B can be altered by changing the fiber diameter, the fiber length, the entrapped particle size, and the mass. In order to investigate the effect of media constants on initial pressure drop, we selected MFM C as the modeled media. The model predictions are made for single filters with 30 pleats. All the filters were 24" × 24" × 2" and the media thickness was kept at constant. The media constants ( $A = 10 \times 10^{-4}$ ,  $B = 1 \times 10^{-6}$ ) are assumed to be half of the normal values and two times of the normal values, respectively.

The simulated results are presented in Figure 4.19. As shown in Figure 4.19, the initial pressure drop increased as the media constants increased. Therefore, increasing fiber diameters and reducing sorbent particle loading during the media preparation process would be helpful for reducing initial pressure drop. However, reduction of sorbent particle loading would lower the removal efficiency of gaseous contaminants. So a better packaging design would be needed to solve the problem. Multi-element structured array (MESA) developed by Sothen (2009) can greatly increase the sorbent particle loading capacity and further reduce the pressure drop by employing a number of pleated filters into a single filtration unit.

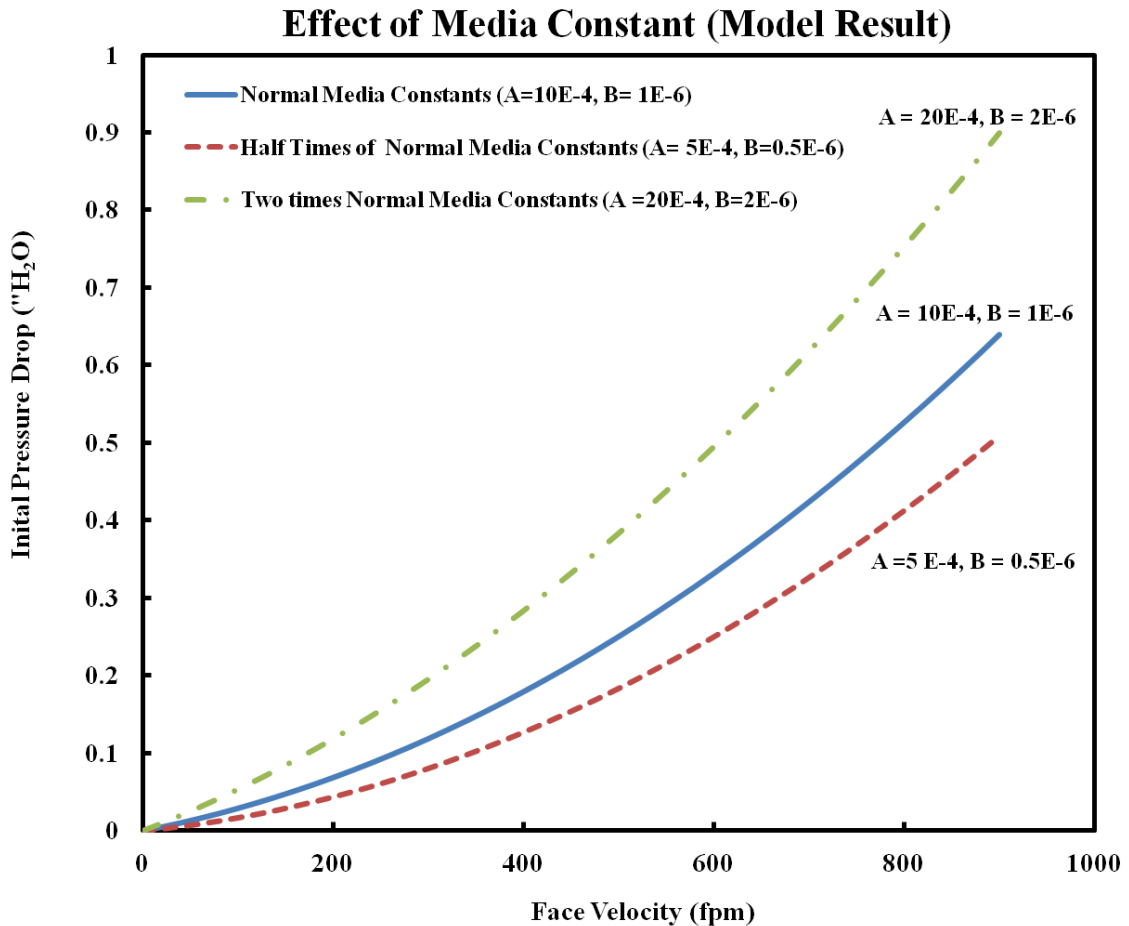


Figure 4.19 Effect of media constants on initial pressure drop for MFM filters

## 4.6 Conclusions

As a design tool, Sothen's semi-empirical pressure drop model was used to investigate the impacts of design factors (pleat count, filter depth, media constants and media thickness) on initial pressure drop for pleated filters made of MFM. The model results showed that a pleated filter made of MFM also experienced a minimal pressure drop corresponding to an optimal pleat number as commercial particle filters do. In addition, the simulated results showed that the optimal filter depth is 2" for the filters made of the same MFM with the same pleat number and the same cross section. As expected by the theory, media thickness plays an important role on affecting the flow resistance across the filter. The model predicted results indicated that the compressed media can help to reduce the initial pressure drop and increase the sorbent loading capacity at the same time. Computed results by the model also showed that reducing media constant can lower the initial pressure drop. Therefore, any factor that is able to reduce the media constants should be considered during the media design and preparation processes.

# **Chapter 5 Influence of Design Parameters on Filtration Performance of MESA**

## **5.1 Introduction**

The health effects of indoor air pollution have received great attention during the last two decades because more and more health problems have been proved to be related to poor indoor air quality, such as asthma, allergies, lung cancers, and Sick Building Syndromes (SBS) (Brooks et al., 1991; Horvath, 1997; Lahtinen et al., 1998; Jones, 1999; Godish, 2001; Daisey et al., 2003; Sundell, 2004). Rising concerns about indoor air quality have resulted in the need for more stringent air filtration requirements in heating, ventilation, and air conditioning (HVAC) systems. Air filters capable of removing both particle matter and airborne molecular contaminants simultaneously are needed to meet the high air purification requirements. However, as media of those filters, sorbent (i.e., activated particle carbon, activated alumina) containing media has some disadvantages due to the presence of small sorbent particles, such as high pressure drop, lower permeability and low saturation capacity (Harris et al., 2001). Since pressure drop across an air filter is proportional to the system's energy consumption, high pressure drop is detrimental to energy efficiency (Fisk et al., 2002; Arnold et al., 2005).

Pleated filters and V-bank mini pleated filters are two strategies which can be used to overcome the disadvantages of those materials, and improve both pressure drop performance and overall sorbent loading capacity. A new housing design devised by Sothen and Tatarchuk (2009) can further maximize the usefulness of sorbent containing media. It was named as multi-

element structure array (MESA) or multi-element pleated filter bank (MEPFB). By integrating multiple pleated filter elements into a single filtration system to form “macro pleats,” MESA has been shown an effective design for reducing flow resistance across filtration units and increasing loading capacity (Sothen and Tatarchuk, 2009; Sothen, 2009). In pressure-sensitive filtration applications, such as medical and other specialty applications, the increased available filtration area and loading capacity of MESA can greatly reduce the pressure drop and dramatically improve contaminant removal from breathing air compared with single carbon air filter. Therefore, they can serve as a platform for high resistance sorbent containing media.

Sothen and Tatarchuk (2009) also developed a semi-empirical pressure drop model capable of predicting the initial pressure drop of MESA. For a media of known thickness and permeability, the model can be used as a predictive design tool without the use of nontransferable factors or extensive empirical data. However, the influence of design parameters such as element numbers, element depth, pleat numbers, element alignment and fairings for initial pressure drop of MESA is unknown. Understanding the effects of these parameters is very important for optimizing MESA design.

In this study, the effects of element numbers, element depth, pleat numbers, element alignment and fairings on flow resistance across the filtration unit are investigated experimentally and compared against the semi-empirical model. The optimal configuration of MESA is determined based on the experimental results. Furthermore, an estimation of lifetime and energy consumption for a pleated filter and a MESA unit is presented. It is expected that this work can bring some insights to energy-efficient air filtration system design.

## 5.2 Material

### 5.2.1 Construction of MESA unit

MESA units were made of 5/8" particle board. The obtained 48" × 24" rectangular particle boards were cut down into 24" × 24" and 28" × 24" sections by using table saw. The 28" × 24" sections served as the top and bottom walls, and the 24" × 24" sections served as the side walls. They were fastened to the extended squares using drywall screws. L brackets were added to all eight corners to further strengthen the bank unit. The units were outfitted with 1.5" flanges in order to mate up with the ductwork and form a tight seal. The flanges were reinforced with 1" wide strips of particle board. The reinforcing brackets and strips were necessary to prevent the flanges from failing when subjected to the 9010 N of force created by a clamping system which was used to hold the MESA unit in the test rig. All cracks and joints were sealed with RTV silicone gasket sealant. The filter elements were held in the bank units by a combination of mechanisms. The front edges were created by custom cutting aluminum or plastic extruded U channel. The U channel fit tightly between the top and bottom walls to serve as an anchor for the filter element. L channels were added to the top and bottom walls to serve as support and provided additional seals for the filters. A solid seal was created between the L bracket and the filter element through the use of closed-cell foam. A V-shaped filter bank for 1 inch deep filters is shown in Figure 5.1.



Figure 5.1 Schematic of multi-element structured array housing (Sothen, 2009)

### 5.2.2 Tested filter information

Most filters tested in this study were specially ordered from Quality Filters in Robertsdale, AL. The filters tested for effect of fairing equipment within a MESA were ordered from American Air Filter local agent. The following table listed the dimensions and pleat counts of tested filters.



Table 5.1 Critical parameters of filters utilized

<b>Filter</b>	<b>Nominal Size Width×Height×Depth (inch)</b>	<b>Actual Size Width×Height×Depth (inch)</b>	<b>Pleat Count (-)</b>
1	24×24×2	23.375×23.375×1.75	15
2	24×24×2	23.375×23.375×1.75	20
3	24×24×2	23.375×23.375×1.75	25
4	24×24×2	23.375×23.375×1.75	28
5	24×24×2	23.375×23.375×1.75	30
6	24×24×2	23.375×23.375×1.75	35
7	24×24×2	23.375×23.375×1.75	40
8	12×24×2	11.375×23.375×1.75	12

### 5.3 Experimental Set-up and Test Procedure

Initial pressure drop, removal efficiency and dirt loading tests were run on the full-scale ASHRAE standard 52.2 test duct. The experimental set-up and test procedure were described in Chapter 3.

### 5.4 Results and Discussion

#### 5.4.1 Comparison of MESA unit and single filter

Initial pressure drop tests were performed on a single 2 inch deep filter with 40 pleats, a V-shaped filter bank by loading two same single filters and a W-shaped filter bank by loading four same single filters. The experimental results were shown in Figure 5.2. From this figure, we can see that MESA could effectively decrease the flow resistance compared to a single pleated filter in the same test condition. The lowest initial pressure drop was achieved by a W-shaped MESA. The initial pressure drop of V-shaped MESA was also much lower than that of a

single filter. The initial pressure drops for these three filtration units at an air face velocity of 500 fpm are listed in Table 5.2. As shown in this table, the V-shaped and W-shaped MESAs can reduce initial pressure drop by 52.5% and 59.7%, respectively.

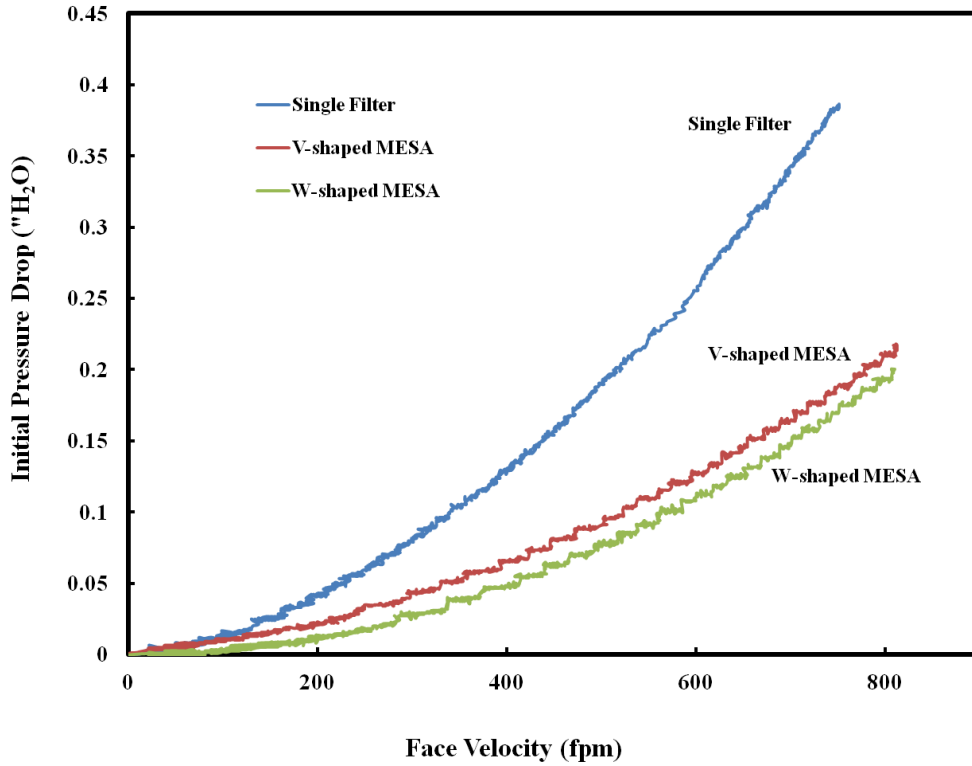


Figure 5.2 Comparison of initial pressure drop across single filter, V-shaped MESA and W-shaped MESA

Table 5.2 Initial pressure drop at 500 fpm

<b>Filtration Unit Type</b>	<b>Initial pressure drop ( \" H<sub>2</sub>O )</b>	<b>Improvement ( - )</b>
Single Filter	0.191	0%
V-shaped MESA	0.091	52.5%
W-shaped MESA	0.077	59.7%

### 5.4.2 Effect of element alignment within a MESA

Pleated filter elements can be loaded into a MESA unit in two different manners: horizontally-oriented pleats or vertically-oriented pleats (Figure 5.3). The different pleat alignments could affect the pressure drop across the MESA unit. In order to determine a preferred loading manner, the initial pressure drop across a V-shaped MESA bank loaded by two 24" × 24" × 2" filters in horizontally-oriented pleats was tested, then the initial pressure drop across a V-shaped MESA bank loaded by two 24" × 24" × 2" filters in vertically-oriented pleats was tested as well. Each of the tested filters had 28 pleats. The experimental results are shown in Figure 5.4.



Figure 5.3 Horizontally-oriented (left) & vertically-oriented (right) banks

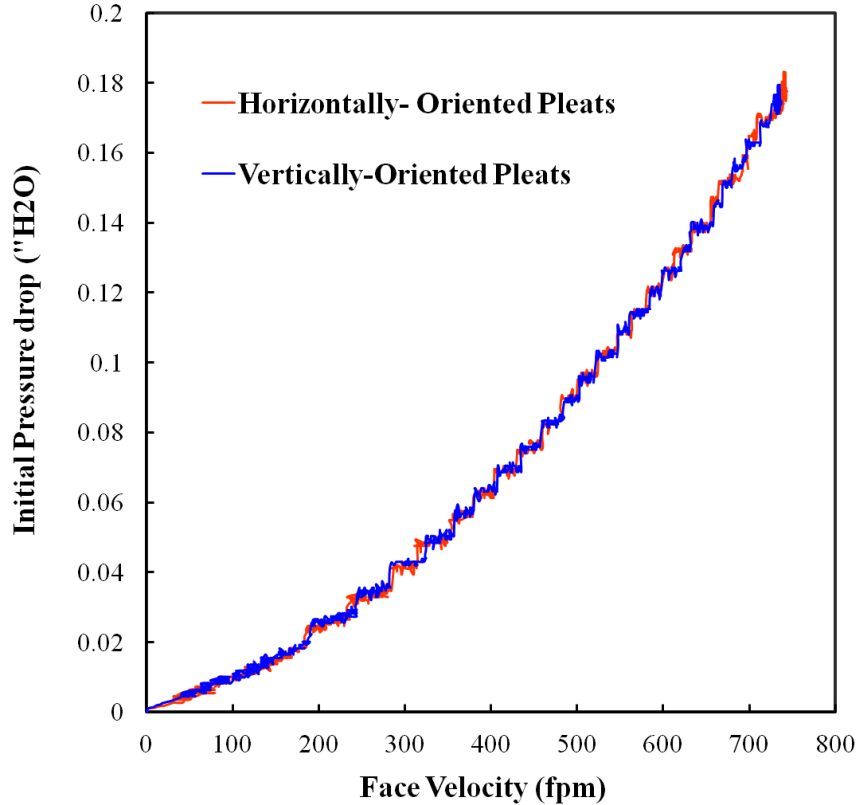


Figure 5.4 Effect of pleat alignment on initial pressure drop for V-shaped MESA

It was observed that there were only minor variations within the initial resistance of the V-shaped MESA units loaded in different manners. The possible explanation for this is that the uniform distribution of flow inside the test rig and the same slot resistance contribution for the overall pressure drop make no difference for those two alignments.

### 5.4.3 Effect of element count within a MESA

Two, four, six and eight two inch deep filters can be loaded into a MESA unit to compose “V,” “W,” “WV” and “WW” configurations, respectively (Figure 5.5). In this section, we will discuss the influence of element count on the filtration performance. Initial pressure drop tests were performed on different configurations of MESA. These MESA units were

loaded with 30 pleats filters of dimension 24" × 24" × 2". The experimental results are shown in Figure 5.6. As depicted in this figure, we can see that the initial pressure drop of MESA units with "V," "W" and "WV" configurations was lower than that of the single filter. But, the MESA unit with "WW" configuration had much higher initial pressure drop than the single filter. "V"-shaped and "W"-shaped MESA units showed the lowest initial pressure drop among all of the tested configurations. A possible reason is that V," "W" and "WV" configurations have much more available filtration area than a single filter, therefore, the media face velocity was decreased and lower pressure drop was produced as a result. Although "WW"-shaped MESA has more filtration area than a single filter, more front and back areas are blocked, a four-fold difference compared to the V-shaped configuration, so the initial pressure drop was higher than that of a single filter. When the face velocity is about 500 fpm, the lowest initial pressure drop (0.076" H<sub>2</sub>O) can be obtained from the W-shaped MESA, which is only half of that from the single filter. This experimental result was in good agreement with the prediction by the semi-empirical pressure drop model for MESA units.

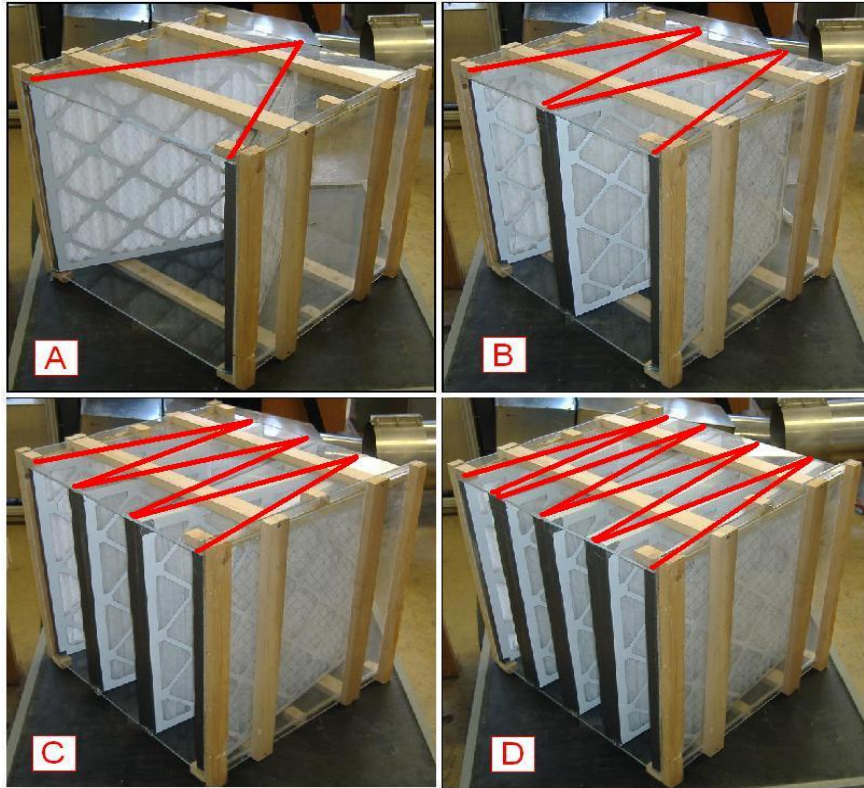


Figure 5.5 Different MESA configurations (Sothen, 2009)

(A) "V" configuration (B) "W" configuration  
(C) "WV" configuration (D) "WW" configuration

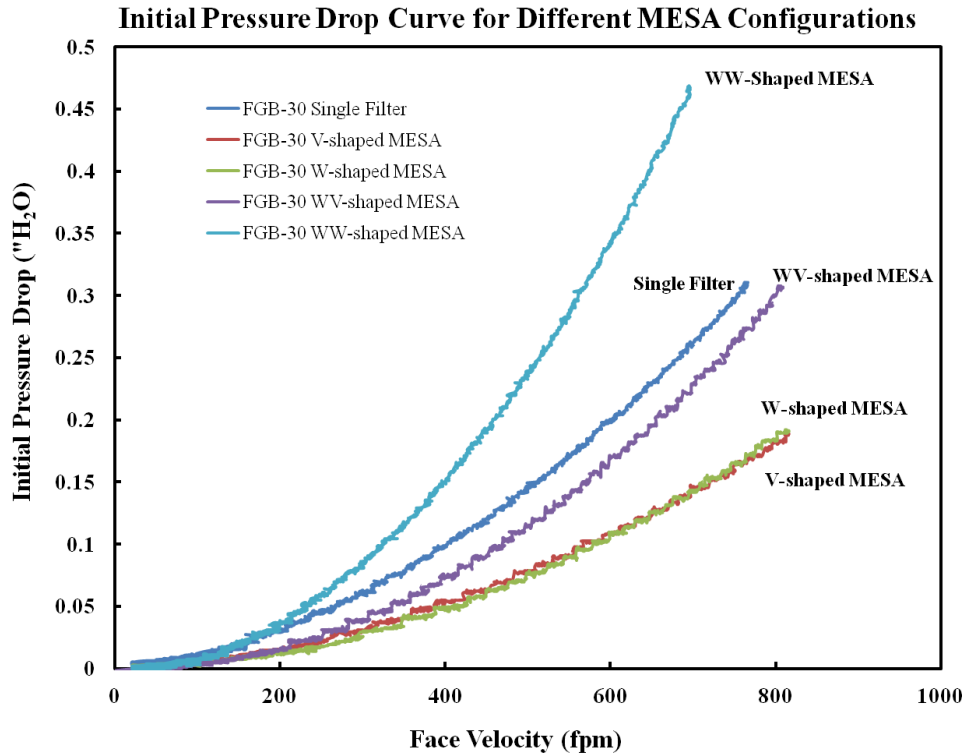


Figure 5.6 Effect of element count on initial pressure drop for 2 inch deep MESA units

#### 5.4.4 Effect of element depth within a MESA

Sothen has predicted the effect of element depth on initial pressure drop at 500 fpm by applying his semi-empirical pressure drop model for MESA units (Figure 5.7) (Sothen, 2009). The result indicated that a two inch deep MESA unit has the lowest initial resistance compared with one inch and four inch deep MESA units. We ran initial pressure drop tests for a one inch deep V-shaped MESA unit, a two inch deep V-shaped MESA unit and a four inch deep V-shaped MESA unit individually. These V-shaped MESA units were loaded with two 24" × 24" filters with 20 pleats of 1", 2" and 4" deep accordingly. Figure 5.8 shows the experimental results. As displayed in this figure, the lowest initial pressure drop was obtained on the two inch deep V-shaped MESA unit when the face velocity was 500 fpm. The experimental result

shows good agreement with the model prediction. It can be concluded that two inches is the optimal element depth for MESA units.

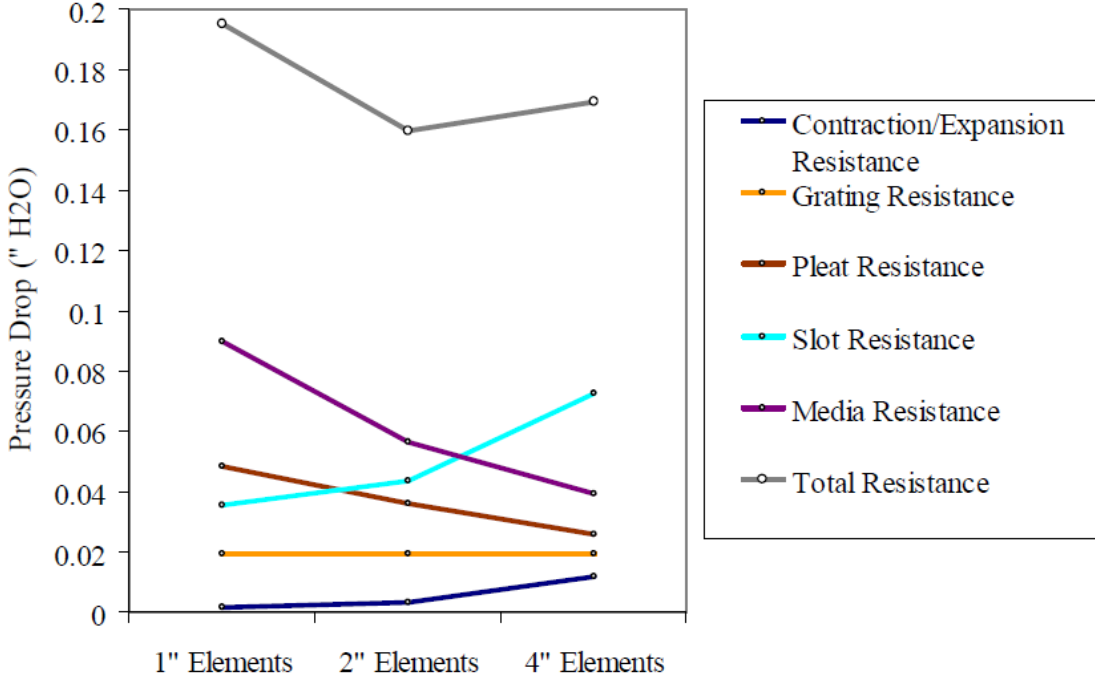


Figure 5.7 Effect of element depth on contribution (Sothen, 2009)



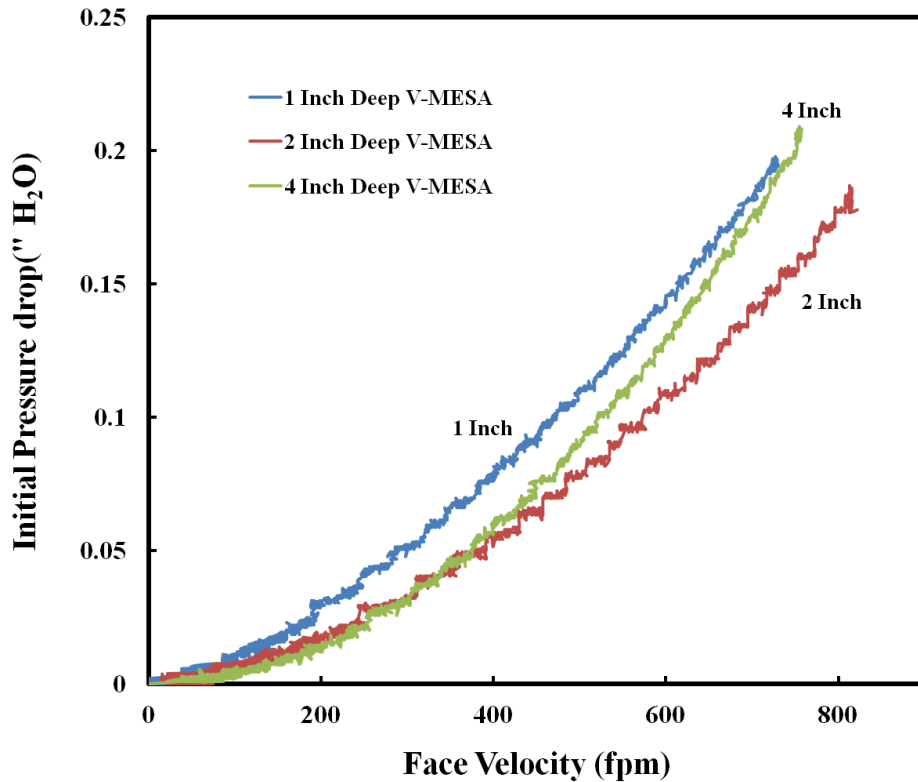


Figure 5.8 Effect of element depth on initial pressure drop for V-shaped MESA

#### 5.4.5 Effect of pleat numbers within a MESA

Previous studies indicated that an optimal pleat count existed, corresponding to the lowest obtainable resistance for single pleated filters (Sothen and Tatarchuk, 2008). The optimal pleat count occurred due to the tradeoff of media resistances for viscous resistance as the pleat count was increased. Throughout the experiments, it was found that the optimal pleat count is 44 for 1 inch deep pleated filters, 20 for 2 inch deep pleated filters, and 16 for 4 inch deep pleated filters (Figure 5.9). In order to investigate the influence of pleat numbers on initial pressure drop for the optimal MESA configuration, we ran a series of initial pressure drop tests for a W-shaped MESA by loading 2 inch deep filters with 15, 20, 25, 30, 35, 40 pleats. In

contrast, we also ran initial pressure drop tests for 2 inch deep single filters with 15, 20, 25, 30, 35, 40 pleats.

Figure 5.10 (a) shows the experimental results for single filters, and (b) shows the experimental results for MESA units. By comparing these two figures, it can be seen that pleat numbers have an obvious effect on single filters, but a negligible effect on MESA units. The reason is that the slot resistance serves as the dominating resistance at all pleat counts for the W-shaped MESA unit. For the W-shaped MESA units loaded with different pleat number filters, the slot resistances were equal, therefore, the overall pressure drop did not show obvious differences.

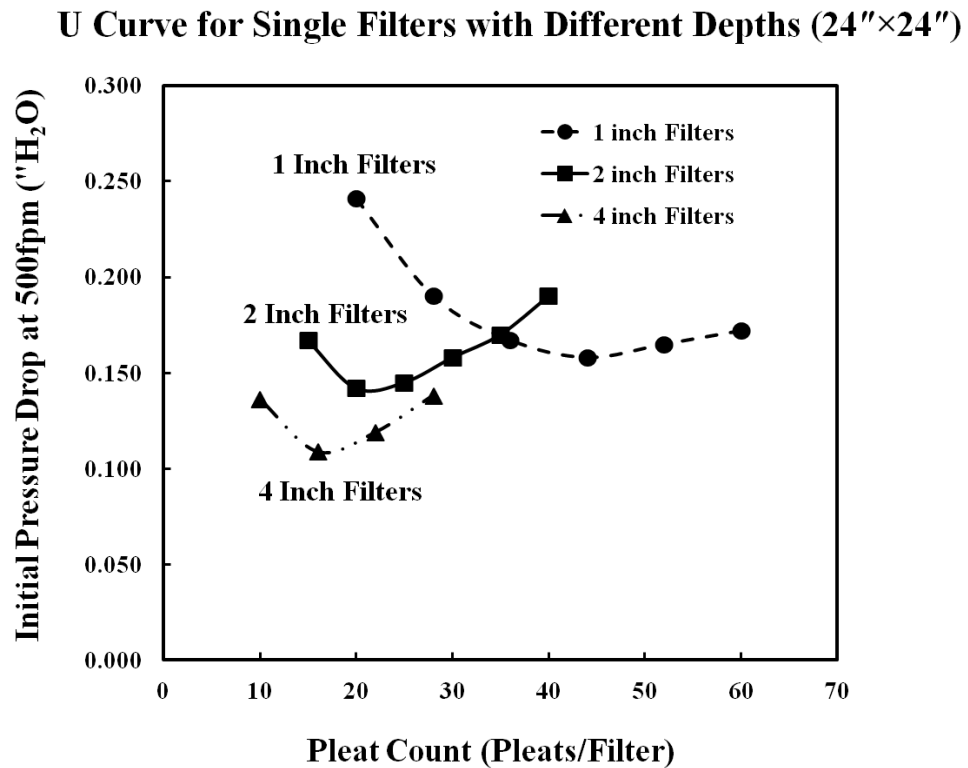
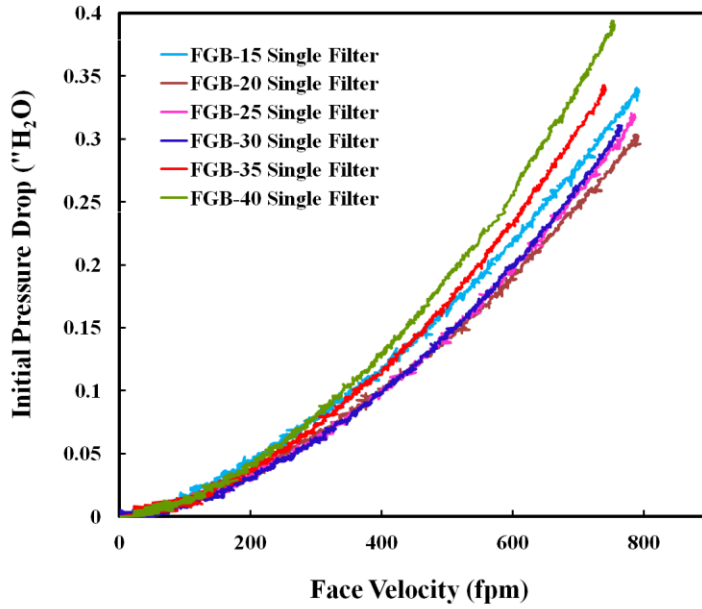
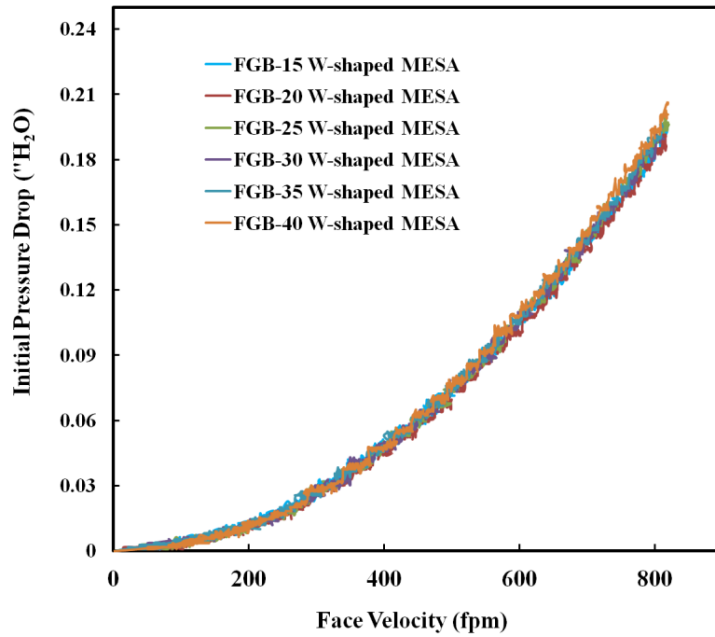


Figure 5.9 Pleating curves for 1, 2 and 4 inch deep filters (experimental results)



(a) Effect of pleat numbers on initial resistance curve for 2 inch deep single filters



(b) Effect of pleat numbers on initial resistance curve for 2 inch deep W-shaped MESA

Figure 5.10 Initial pressure drop curve for single filters and W-shaped MESA units with different pleat numbers

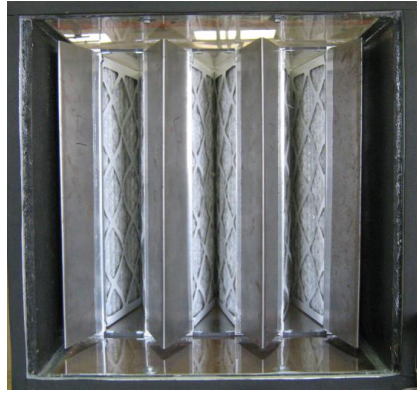
#### **5.4.6 Effect of fairings within a MESA**

Previous studies demonstrated that the addition of a gradual contraction to the front of the bank or a gradual expansion out of the bank could slightly decrease the overall pressure drop (Sothen and Tatarchuk, 2009). In order to reduce the geometric resistance, we made some modifications to the MESA units. Specifically, we added three pieces of fairing equipment in the front of a WV-shaped MESA unit and four pieces of fairing equipment in the back of the WV-shaped MESA unit. This fairing equipment was made in our lab. Pictures of the modified WV-shaped MESA are shown in Figure 5.11. The WV-shaped MESA unit was loaded with 12 pleated filters with the dimension of 24" × 12" × 2" (purchased from a local agent of American Air Filter).

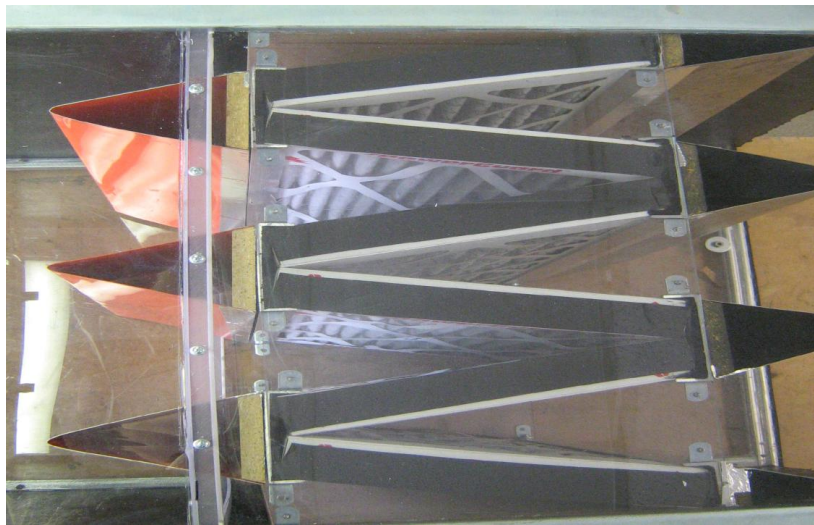
Initial pressure drop tests were run on the unmodified WV-shaped MESA unit, the WV-shaped MESA unit with front fairing equipment only, and the WV-shaped MESA unit with both front and back fairing equipment. The experimental results are shown in Figure 5.12. It was observed that the addition of front fairings can decrease the overall pressure drop and the addition of both of front and back fairings can further decrease the overall pressure drop. With the face velocity increase, the decrease becomes more obvious. At about 500 fpm, the addition of both front and back fairing equipment can reduce initial pressure drop by 15% compared with the unmodified MESA unit. Therefore, the addition of fairing equipment can effectively reduce the overall initial pressure drop.



A. Front view



B. Back view



C. Top view

Figure 5.11 Pictures of the tested MESA unit with fairings

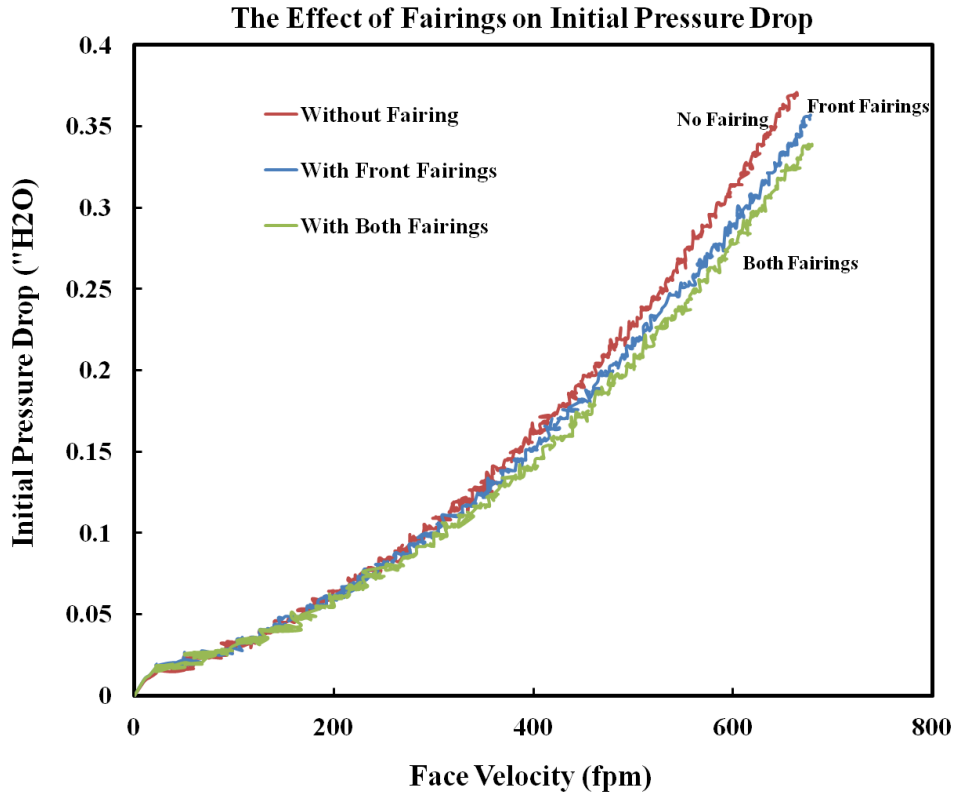


Figure 5.12 Effect of fairings on initial pressure drop of WV-shaped MESA unit

#### 5.4.7 Estimations of useful lifetime and power consumption

Based on the obtained dirt loading data, estimations for the useful lifetime and average energy consumption of single filter with 30 pleats, and V-shaped MESA unit loaded by four single filters with 30 pleats were made. Several assumptions were required before the values could be calculated. A filter was assigned a useful life until a final pressure drop (1\" H<sub>2</sub>O) was reached, which is suggested by the filter manufacturer. The filter should be changed at this point. The operational conditions were set at 2000 cfm with an average run time of 8 hours per day. Total atmospheric dirt concentration is highly dependent on the environment; therefore, it was assumed that the total atmospheric dust concentration in the air was 30 ug/m<sup>3</sup> and that the filter can only capture about one third of the total dirt in the air. The national average residential

electricity cost was taken from the Department of Energy's Energy Information Agency website as \$0.11/kWh (December 2010 estimate). Energy consumption only accounted for the pressure volume work to move air across the filtration unit. The blower efficiency due to power conversion was estimated at 70%. The labor fee was about \$32/hour, based on the information provided by the facility department of Auburn University. The equation used to determine the energy cost follows (Arnold, 2005)

$$\text{Energy Consumption (kWh)} = \frac{Q\Delta Pt}{\eta 1000}$$

where

Q = airflow (m<sup>3</sup>/sec)

ΔP = avg. pressure loss (Pa)

t = time in operation (hours)

η = fan efficiency

The power and energy analysis shown in Table 4 was prepared based on these assumptions and the above formula. Filter costs listed were prices paid to procure the filters from Quality Filters. In order to load about the same amount of dirt and operate at the equal time, two single filters are continuously needed for the case of single filter. Therefore, the energy consumption listed in the table for the case of single filter is the summation of two single filters. The analysis demonstrated that the employment of a V-shaped MESA unit instead of two traditional single pleated filters can result in a 27% reduction in energy consumption. Considering the labor fee for installation and maintenance, the total saving to the end user for one filtration unit was estimated at \$20.87 over the six months period.

A 54% annual reduction in pressure volume work for heating, ventilating and air conditioning (HVAC) systems would have a major impact on the annual energy consumption of

the United States. For instance, households in the United States consumed about 586 billion kWh energy for their HVAC systems in 2007 (Bigelow, 2008). Of that 586 billion kWh, roughly 15% went to the pressure volume work required to move air across the filter units. The employment of a more efficiently designed filtration unit could lead to a 47.5 billion kWh reduction in annual energy consumption within the United States.

Table 5.3 Estimated lifetime costs for single filter, V-shaped MESA unit

	Single Filter	V-MESA
Filter Cost (\$5.24 per filter)	10.48	10.48
Initial Resistance ("H <sub>2</sub> O)	0.156	0.080
Final Resistance ("H <sub>2</sub> O)	1	1
Dirt Loading (g)	65.94	132.13
Life Time (Days)	110	202
Energy Consumption (kWh)	161.68	117.32
Energy Costs (\$)	17.78	12.91
Labor Costs (\$)	32	16
Total Costs (\$)	60.26	39.39

## 5.6 Conclusions

Multi-element pleated filter banks can effectively decrease the flow resistance compared to single pleated filter at the same conditions. The influence of design parameters, such as element alignment, element count, element depth, pleat numbers and fairings on initial pressure drop of MESA units has been investigated experimentally. The loading manner (horizontally-oriented pleats or vertically-oriented pleats) did not have a significant effect on the resistance of



MESA units. Throughout our experiments, W-shaped MESA has been shown to be the optimal configuration and the two inch depth has been shown to be the optimal element depth for the lowest pressure drop. Although an optimal pleat count exists with respect the lowest initial pressure drop for single pleated filters, there is no difference for MESA units loaded by different pleat numbers filters, since the slot resistance serves as the dominating resistance. Experimental results indicated that the addition of front and back fairings could reduce initial pressure drop by 15% compared with the unmodified MESA unit at an air face velocity of about 500 fpm. The analysis demonstrated that the employment of a V-shaped MESA unit instead of two traditional single pleated filters can result in a 27% reduction in energy consumption for a period of six month. Considering the labor fee for installation and maintenance, the total savings to the end user was an estimated \$20.87 for one filtration unit. Therefore, application of MESA units in air filtration has great potential for increased energy efficiency and cost savings.

## **Chapter 6 Pressure Drop Evolution of Pleated Filter During Dirt Loading**

### **Process**

#### **6. 1 Introduction**

In addition to the initial pressure drop, dirt loading capacity is another important factor for evaluating a filter's performance, since it is related to the life time of a filter. There are several advantages for increasing the amount of particle material that a filter could hold. One advantage is that the increased dust holding capacities would result in lower replacement costs since each unit would have a longer life. A closely related second advantage would be fewer times when the whole system has to be shut down in order to replace filters. A third advantage is that the annual maintenance costs would be much less.

In general, the pressure drop during dust loading displays three regions: an initial region of slow increase, a transition region and a final region of cake filtration. The typical behavior of a fibrous filter under aerosol loading is shown in Figure 6.1 (Song et al., 2006). When a surface cake is formed, the resulting pressure drop increase per unit deposit is very large in this regime. Filter replacement is standard practice as a consequence. Therefore, elongating the depth filtration will extend the filter lifetime and lower maintenance costs.

By varying the effective pore diameter and the filter structure, the arrival of the cake filtration phrase can be hastened or delayed. As shown in Figure 6.1, after filter cake formation, the slopes of pressure drop with mass loading were identical for a specific particle diameter regardless of the filter structure (Japuntich et al., 1994). The effect of dust loading on pressure

drop is not fully understood because of the enormous complexity of the problem. There is a need to understand the relationship between mass loading and pressure drop and there is a need to predict when a filter would be entering the transition region. Such insights would guide filter users to know when it would be the best time to replace their filters and thus achieving energy efficiencies without wasting any energy.

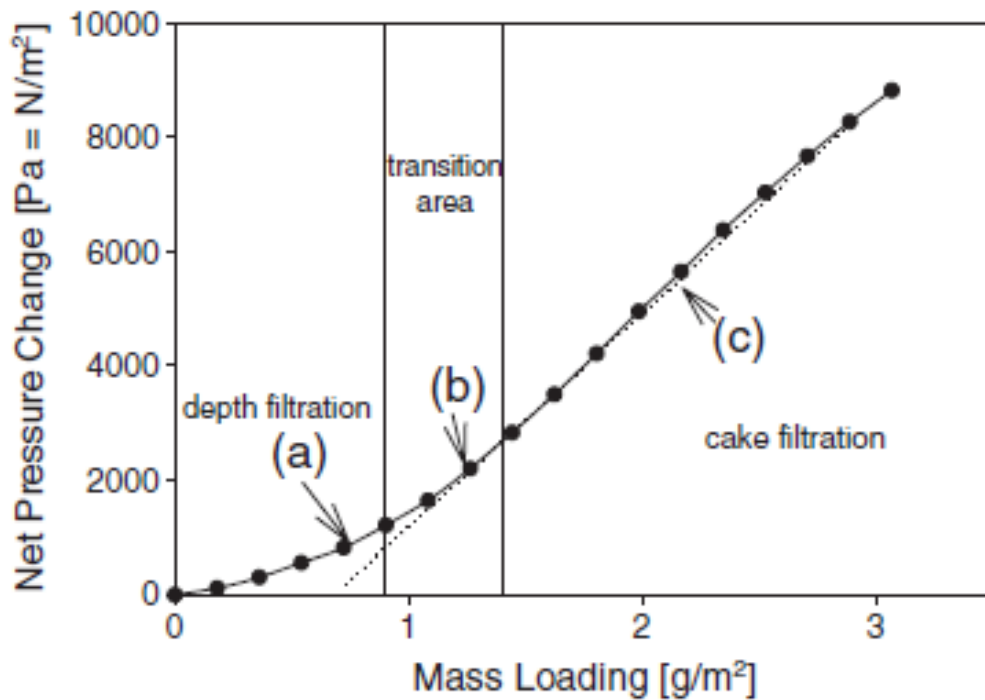


Figure 6.1 A typical loading curve (Song et al., 2006)

## 6.2 Previous Research

Some researchers have attempted to develop a mathematical equation for prediction of pressure drop evolution during dirt loading process. Davies (1973), Bergman et al. (1978), Payatakes and Okuyama (1982), Kanaoka and Hiragi (1990) all developed a theoretical model describing the pressure drop due to particles collected inside the filter. Novick et al. (1990, 1992) first took into account the presence of a cake. Thomas et al. (1999, 2001) developed a

model that was derived from first principle theory. Song et al. (2006) developed an empirical model related to laboratory loading data. The following sections will briefly discuss the key points for some of these previous studies.

### 6.2.1 Davies

Davies' (1973) model (Eq. 6.2) is based on the equation he had developed for a clean filter (Eq. 6.1). He took into account the collected mass and he assumed that the particles would uniformly settle on each fiber. This approach accounted for the increase in the fiber diameter and the filter packing density. The main advantage of this model is that all parameters could be easily calculated. However, the particle size was not considered.

$$\Delta P_0 = 64\mu VZ \frac{\alpha_f^{\frac{3}{2}}(1+56\alpha_f^3)}{D_f^2} \quad (6.1)$$

$$\Delta P = \Delta P_0 \frac{\ln \alpha_f + K}{\ln(\alpha_f + \alpha_p) + K} \quad (6.2)$$

### 6.2.2 Bergman et al.

Bergman et al. (1978) took into account two kinds of fibers contributing to pressure drop during the dirt loading process: the initial clean fibers of the filter and the deposited particles forming dendrites which were considered as new collecting fibers. Then, he modified Davies' (1973) model relating pressure drop during depth filtration to properties of the filter and aerosol as

$$\Delta P = 64\mu VZ \left( \frac{\alpha_f}{D_f^2} + \frac{\alpha_p}{D_p^2} \right)^2 \left( \frac{\alpha_f}{D_f} + \frac{\alpha_p}{D_p} \right) \quad (6.3)$$

This model assumes a homogeneous deposition of aerosol particles inside the filter, which means that particle deposit and particle diameter are uniform over the whole filter thickness. By a peeling method, Letourneau et al. (1990) showed that collected particles are not

uniformly distributed over the whole thickness of a filter and surface layers are more loaded than depth layers. Later, Vendel et al. (1992) compared experimental results with the Bergman model results for the most penetrating aerosol (0.15  $\mu\text{m}$  and 0.25  $\mu\text{m}$ ). They noted that Bergman's model underestimates the pressure drop. Therefore, they suggested that filter pressured drop as a function of the deposited aerosol mass requires the knowledge of the penetration profile of particles inside the filter media.

### 6.2.3 Kanaoka and Hiragi

Kanaoka and Hiragi (1990) established a model to predict the pressure drop of a dust loaded filter based on the determination of the drag force acting on the fibers with the following expression

$$-\Delta P_m(t) = -\Delta P_0 \int_0^Z \frac{C_{Dm}(x,t)}{C_{D0}} \cdot \frac{D_{fm}(x,t)}{D_f} \cdot \frac{dx}{Z} \quad (6.4)$$

In this model, the diameter of a dust loaded fiber and drag coefficient are representative parameters of agglomerate structure and is correlated with collection mechanism and accumulated mass of particle on the fiber. If effective fiber diameter and drag coefficient of a dust loaded fiber are given as a function of accumulated volume of captured particles, the proposed model is applicable to the prediction of the pressure drop of a dust loaded filter in any filtration condition. Since those relationships are hard to determine without well defined filter structure, the model is very complicated.

### 6.2.4 Novick et al.

Novick et al. (1990, 1992) proposed a two termed model for predicting either the final pressure drop across a loaded HEPA filter or the maximum mass that can be loaded onto a HEPA filter for a specified pressure drop. This model describing the total pressure drop across

the filter due to mass loading can be written as the summation of the pressure drop ( $\Delta P_0$ ) of the clean filter and the pressure drop ( $\Delta P_p$ ) across the filter cake due to particle loading as follows:

$$\Delta P = \Delta P_0 + \Delta P_p \quad (6.5)$$

The pressure drop across the clean filter is described by Darcy's law as follows:

$$\Delta P_0 = K_1 V \quad (6.6)$$

The constant  $K_1$  for the HEPA filters in their tests was measured to be  $7.97 \times 10^2 \text{ g/cm}^2$ . Pressure drop across the filter cake due to mass loading ( $\Delta P_p$ ) can be described as follows:

$$\Delta P_p = K_2 V \frac{M}{A} \quad (6.7)$$

The constant  $K_2$  is the specific resistance of loading material on the filter and depends primarily upon the particle diameter and cake porosity. However, the cake porosity can only be determined with experimental measurements of the thickness of the deposited cake and total mass of particles in the cake. These measurements are difficult and subject to large experimental errors. For these reasons, it is more practical to define  $K_2$  in terms that are more easily measureable;

$$K_2 = (\Delta P - \Delta P_0) A / MV \quad (6.8)$$

The specific  $K_2$  in their experiments was determined by the following expression

$$K_2 = \frac{0.963}{D_p} - 1.64 \times 10^5 \quad (6.9)$$

The advantage of this approach is to avoid using some parameters, particularly  $D_e$ , which are difficult to determine or quantify, and allows  $K_2$  to be experimentally corrected with parameters what are known or easily estimated. Therefore, accurate predictions can be made for

the pressure drop as a function of mass loading. However, this model only applies for the laminar gas flow through the HEPA filter (the gas flow velocity is in the range of 0.5 cm s<sup>-1</sup> to 5 cm s<sup>-1</sup>). Also, it is valid only when particle cake thickness on the filter does not exceed half of the spacing between the layers of filter material.

### 6.2.5 Thomas et al.

Thomas et al. (1999) established a model which takes into account the heterogeneous deposit of particles inside the filter medium of HEPA filters. In this model, the filter is considered to be a series of elementary slices which are assumed to be homogeneously loaded by particles. Particles are assumed to form dendrites which can be considered as newly formed fibers. The pressure drop across each slice at each time increment was calculated from a modified Bergman model including the factor  $(1+56\alpha^3)$  proposed by Davies (1952) for high packing density:

$$\Delta P_{J,t} = 16\mu V Z_J \left( \frac{\alpha_{P J,t}}{r_{J,t}^2} + \frac{\alpha_f}{R^2} \right)^{\frac{1}{2}} \left( \frac{\alpha_{P J,t}}{r_{J,t}} + \frac{\alpha_f}{R} \right) [1 + 56(\alpha_f + \alpha_{P J,t})^3] \quad (6.10)$$

Where  $J$  stands for the layer  $J$  and  $t$  stands for time.

Before calculating the pressure drop across the layer  $J$  at time  $t$ , several other parameters need to be estimated, such as the packing density of collected particles ( $\alpha_{P J,t}$ ), and the mean radius of dendrites formed by collected particles ( $r_{J,t}$ ). The calculation process described above is repeated for each time increment up to the final filtration time. The overall pressure drop across the filter at time  $t$  is calculated by the summation of each slice,

$$\Delta P_t = \sum_{J=0}^{np} \Delta P_{J,t} \quad (6.11)$$

Although this model allows the prediction of the pressure drop evolution from the sole knowledge of clean filter, aerosol and filtration characteristics, the calculation procedure is very complicated. The validity of this model was examined only in the depth filtration. Later, Thomas et al. (2001) developed a depth and surface filtration model based on their previous research:

$$\Delta P_{J,t} = 16\mu V Z_J \left( \frac{4\alpha_{P,J,t}}{\bar{d}_{P,J,t}^2} + \frac{4\alpha_f}{d_f^2} \right)^{\frac{1}{2}} \left( \frac{2\alpha_{P,J,t}}{\bar{d}_{P,J,t}} + \frac{\alpha_f}{d_f} \right) [1 + 56(\alpha_f + \alpha_{P,J,t})^3] \quad (6.12)$$

$$\Delta P_t = \sum_{J=0}^{np} \Delta P_{J,t} \quad (6.13)$$

The model describes the transition area between depth filtration and cake filtration as a continuous process and has a good agreement with experiments for submicron particles. The disadvantage of this model is the complexity of the calculation process.

### 6.2.6 Song et al.

Song et al. (2006) developed an empirical model for predicting the pressure drop across a cellulose paper filter during clogging. Similar to the Novick model, the total pressure drop across the filter can be written as the summation of the pressure drop across the clean filter and the pressure drop across the filter cake due to the particle loading. Different from the Novick model, Song et al. take into account the Cunningham correction factor ( $C_c$ ), increasing applicability of the model to particles smaller than 0.5  $\mu\text{m}$ . The proposed model was expressed as follows

$$\Delta P = \Delta P_0 + \Delta P_p = \Delta P_0 + \left( \frac{2.623}{AMD(d_p)C_c} + 9.6450 \times 10^4 \right) \times \frac{VM}{A} \quad (6.14)$$

Where  $C_c$  is Cunningham correction factor, dimensionless

AMD( $d_p$ ) is the aerodynamic particle diameter, m



This correction is only valid for dry and solid particles at relatively low humidity. In addition, some errors exist due to the use of linear fit method assuming that the pressure drop is a linear function of collective mass loading. It also has some limitations relative to the filtration conditions. For example, it is only valid for the face velocity in the range of 0~0.4 m/s corresponding to a laminar flow regime. The challenge particles are the monodispersed polystyrene latex (PSL) particles with the diameter of 0.135~ 2.0  $\mu\text{m}$ .

### **6.3 Experimental Methods**

Two dust loading rigs of similar design but varying size were used in this study. The small rig could incrementally challenge 5.5"  $\times$  5.5" samples of flat media. The full-scale rig was modeled after the ASHRAE 52.2 standard and was capable of continuously loading filter units with internal dimensions up to 24"  $\times$  24"  $\times$  4" (ASHRAE 2007). Details of these two test rigs have been described in Chapter 3.

A common artificial aging material, ASHRAE synthetic test dirt (purchased from Blue Heaven Technologies) was used in this study. Detailed information about this challenge was provided in Chapter 3.

#### **6.3.1 Testing protocol for flat media samples**

Both the Kimberly Clark media and self-made model media were tested on the small rig in this study. The Kimberly Clark media was obtained from the filter manufacturer in a flat form. The model media was constructed by combining layers of differing fibrous material in order to simulate the gradient packing density of the full-scale pleated filter media. The upper two layers consisted of 8  $\mu\text{m}$  (1.5 denier) rayon fibers with a void volume of 92 %. The bottom layers of 6.7  $\mu\text{m}$  polypropylene fibers had a void volume of 68 %. Since the layers were not

chemically or mechanically bonded together, it was possible to deconstruct the media after a test to examine penetration rate and weight gain of each layer.

The small filter system's flow rate was adjusted after each incremental dust addition. The flat media filters were loaded until a desired pressure drop was reached. The filter was then removed and weighed. The resulting singular pressure drop versus weight procedure was repeated for multiple samples to construct an aging curve. The flat filter's loading rates used a higher precision scale ( $\pm 0.001$  g) to measure the weight change.

The small rig utilized a similar foam sample cell but it was designed in accordance with ASTM Standard F778-88 (ASTM 2007). The media sample was prevented from bowing or blowing out by a 98% void metal mesh backing. The pressure drop produced by the metal mesh was subtracted from the resistance measurements. Additionally, the small area blocked by the metal mesh was subtracted from the available media area in subsequent calculations. Taps to measure the pressure drop across the small scale filter were fitted in an identical manner as listed above for the rig's orifice plate. Any uncaught challenge was subjected to a second high efficiency filter before being vented into the atmosphere.

### **6.3.2 Testing protocol for full-size filters**

All full-size filters were custom built by Quality Filters in Robertsdale, AL. Due to the niche order, the manufacturer was only able to supply one filter for each pleat count. The full-size filters used two different filtration media. The media used were both dual layer composites of olefin fibers from Kimberly Clark. Each filter's specifications including dimensions and pleat counts can be found in the results section (Table 6.1).

Flow control in the large duct was maintained by a Hitachi frequency inverter. Due to the dust buildup and subsequent resistance rise across the filter, the inverter's frequency was continuously controlled to maintain a set pressure drop, and therefore volumetric flow, across the mixer. Loading rates for the full-size filters were verified by periodically removing the filter and measuring the weight captured with a Denver Instruments S2002 scale ( $2000 \pm 0.01$  g).

Test filters were sealed and held into the large rig by custom designed holders. Each holder was specifically built to accommodate the size differential between the nominal filter dimensions and the duct. The main components consisted of a permanent flange attached to an encasement with a second removable flange to allow access to the filter. The encasement was sized to fit around the perimeter of the filter frame. Each flange was slightly oversized and outfitted with a foam gasket to prevent bypass around the filter. The rig possessed matching flanges with close-cell foam to provide a seal between the unit and the rig. The seal was created by compressing the entire assembly together with C clamps. The encasement prevented the filter from being crushed by the force of the clamps. No additional support or sealing mechanisms were needed to secure and keep the filter in place.

## **6.4 Results and Discussion**

### **6.4.1 Dirt loading capacity of full-size filters**

Dirt loading results obtained on the full-size filters are listed in Table 6.1.  $\Delta P_F$  stands for the final pressure drop for a full-size pleated filter, which is commonly suggested by the manufacturer as 1" H<sub>2</sub>O (250 Pa). The difference between the initial and final pressure drops of a filter is defined as the operational pressure drop window ( $\Delta P_W$ ). The data presented in Table 6.1 indicates that the dirt loading capacity depends on not only the available filtration area, but

also the operational pressure drop window. For example, the filter with 44 pleats in Set A and the filter with 20 pleats in Set B have the similar filtration area, but the media usages of these two filters show obvious differences due to the variance of the operational pressure drop windows of these two filters. Therefore, more filtration area does not result in more loaded dirt.

Figure 6.2 shows the effect of pleat count on initial pressure drop and dirt loading capacity for Set A and C filters that have the same geometric characterization but different filter media. Similarly, Figure 6.3 presents the effect of pleat count on initial pressure drop and dirt loading capacity for Set B and D filters. As shown in these two figures, for each set of filters, the optimal pleat account correlating to the minimal initial pressure drop is not the same with the optimal pleat count related to the highest dirt loading capacity. The dust holding capacity of a pleated filter is always increased by pleating beyond the pleat count correlating to minimal initial pressure drop. Therefore, when designing pleat filters, the two parameters (initial pressure drop and dirt loading capacity) need to be considered together in order to locate the optimal pleat count for the overall filtration performance.

Poor media utilization rates were also observed for filters with high pleat numbers. In these cases, the decline in media usage was attributed to the smaller operational resistance windows. This decreased window limited the overall dust capacity and as a consequence the average media utilization suffered. These two phenomena, the decreased operational window on low pleat counts and loss of media utilization at high pleat counts, lead to the observance of a pleat count correlating to an optimal media utilization.

Table 6.1 Dirt loading results of full-scale filters

Filter Set (-)	Pleats (-)	$\Delta P_0$ "H <sub>2</sub> O	$\Delta P_F$ "H <sub>2</sub> O	$\Delta P_W$ "H <sub>2</sub> O	Dirt Loaded g	Filtration Area ft <sup>2</sup>	Loading Rate "H <sub>2</sub> O/g/ft <sup>2</sup>	Usage g/ft <sup>2</sup>
Set A 24" × 24" × 1" Media Type 1	20	0.53	1.0	0.47	22.81	5.36	0.11	4.26
	28	0.43	1.0	0.57	40.69	7.53	0.11	5.40
	36	0.37	1.0	0.63	52.00	9.65	0.12	5.39
	44	0.37	1.0	0.63	59.60	11.79	0.12	5.05
	52	0.38	1.0	0.62	64.08	13.94	0.13	4.60
	60	0.43	1.0	0.57	58.41	16.08	0.16	3.63
Set B 24" × 24" × 2" Media Type 1	15	0.32	1.0	0.68	68.76	8.48	0.08	8.11
	20	0.28	1.0	0.72	98.36	11.31	0.08	8.7
	25	0.27	1.0	0.73	109.40	14.14	0.09	7.74
	30	0.26	1.0	0.74	127.23	16.97	0.10	7.5
	35	0.28	1.0	0.72	135.20	19.80	0.11	6.83
	40	0.30	1.0	0.70	151.60	22.63	0.11	6.70
Set C 24" × 24" × 1" Media Type 2	20	0.35	1.0	0.65	25.64	5.36	0.14	4.78
	28	0.24	1.0	0.76	53.52	7.53	0.11	7.11
	36	0.22	1.0	0.78	64.71	9.65	0.12	6.71
	44	0.21	1.0	0.79	71.44	11.79	0.13	6.06
	52	0.22	1.0	0.77	79.73	13.94	0.13	5.72
	60	0.24	1.0	0.76	80.13	16.08	0.15	4.98
Set D 24" × 24" × 2" Media Type 2	15	0.22	1.0	0.78	69.64	8.48	0.09	8.21
	20	0.18	1.0	0.82	97.85	11.31	0.09	8.65
	25	0.18	1.0	0.82	120.10	14.14	0.10	8.49
	30	0.19	1.0	0.81	145.44	16.97	0.09	8.57
	35	0.22	1.0	0.78	158.61	19.80	0.10	8.01
	40	0.24	1.0	0.76	153.71	22.63	0.11	6.79

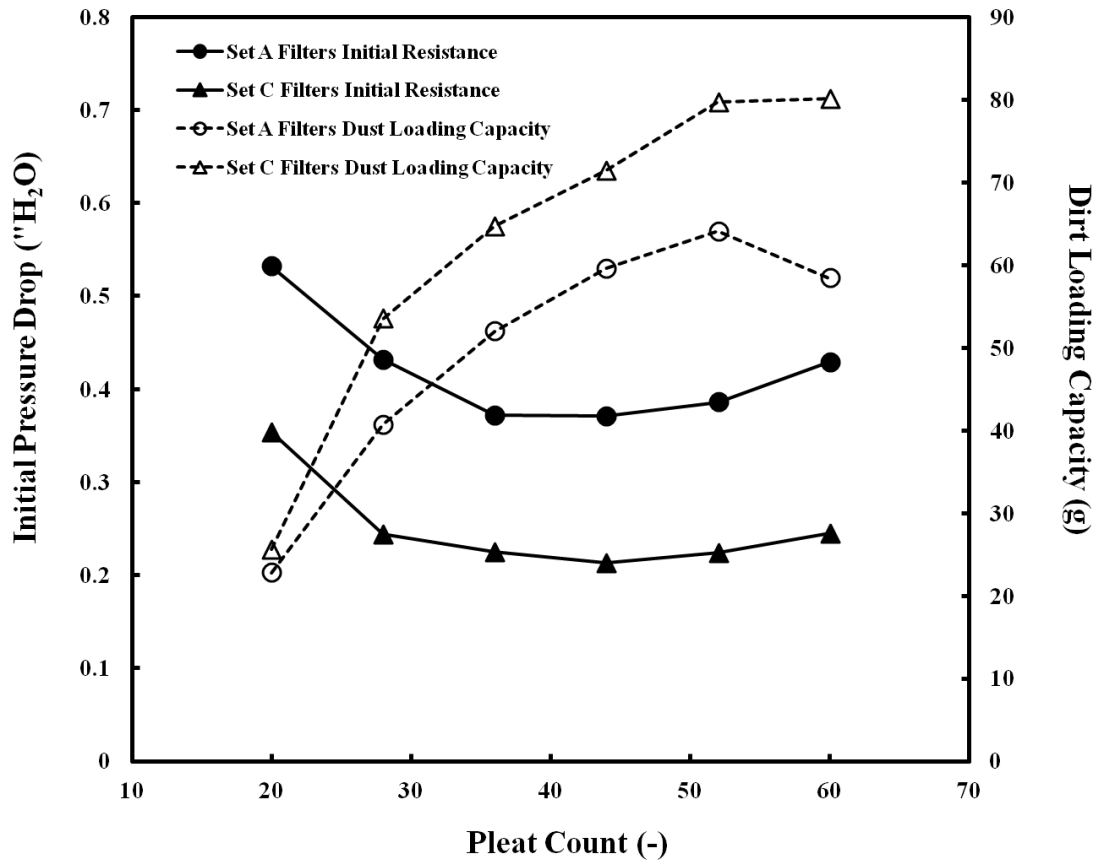


Figure 6.2 Effect of pleat count on initial pressure drop and overall dirt loading of Set A and C filters

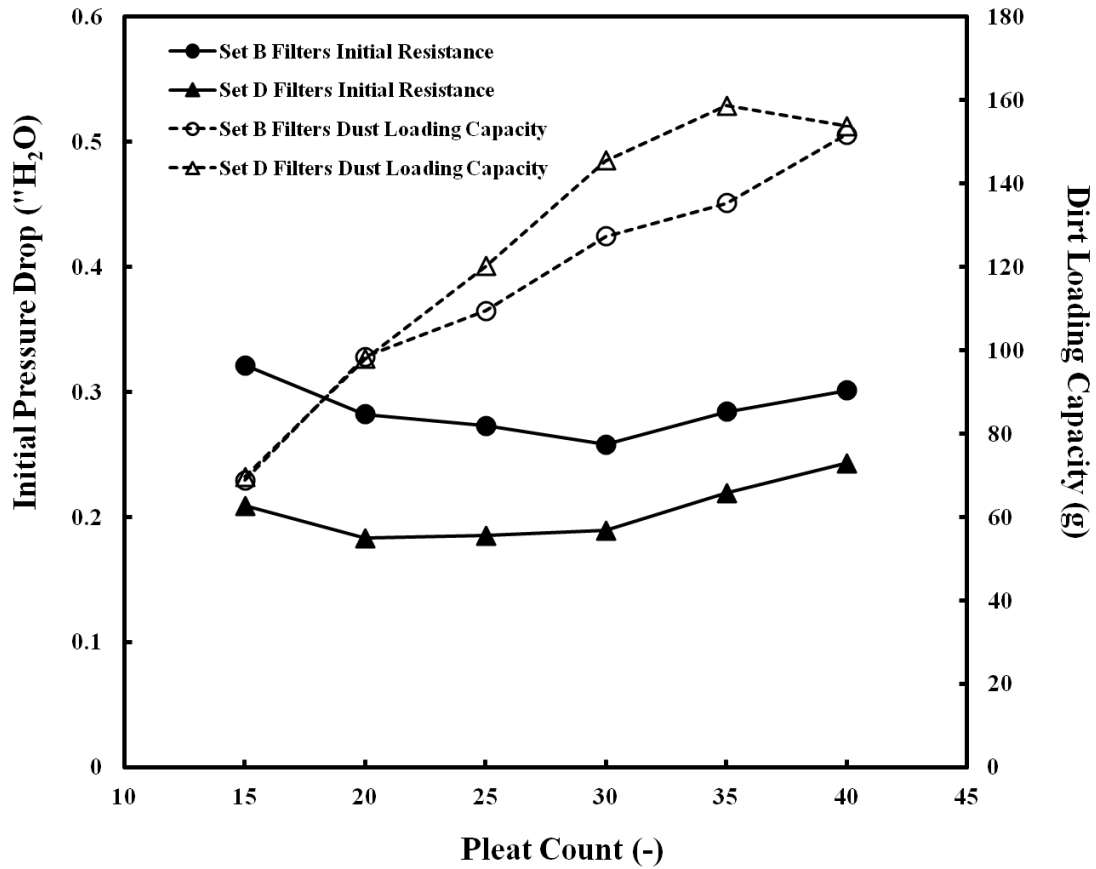


Figure 6.3 Effect of pleat count on initial pressure drop and overall dirt loading of Set B and D filters

#### 6.4.2 Model development and verification

Dirt loading tests were run on different MERV rank (MERV 8, 11 and 13) pleated filters with the dimension of 24" × 24" × 2". MERV 8 pleated filters were obtained from Quality Filters, Inc (QF). MERV 11 and MERV 13 pleated filters were purchased from American Air Filters, Inc (AAF). Experimental results are plotted in Figure 6.4, Figure 6.5 and Figure 6.6, respectively. As shown in these figures, the relationship of incremental pressure drop with the fully normalized dirt loading parameter (VM/A) follows the third order polynomial trend.

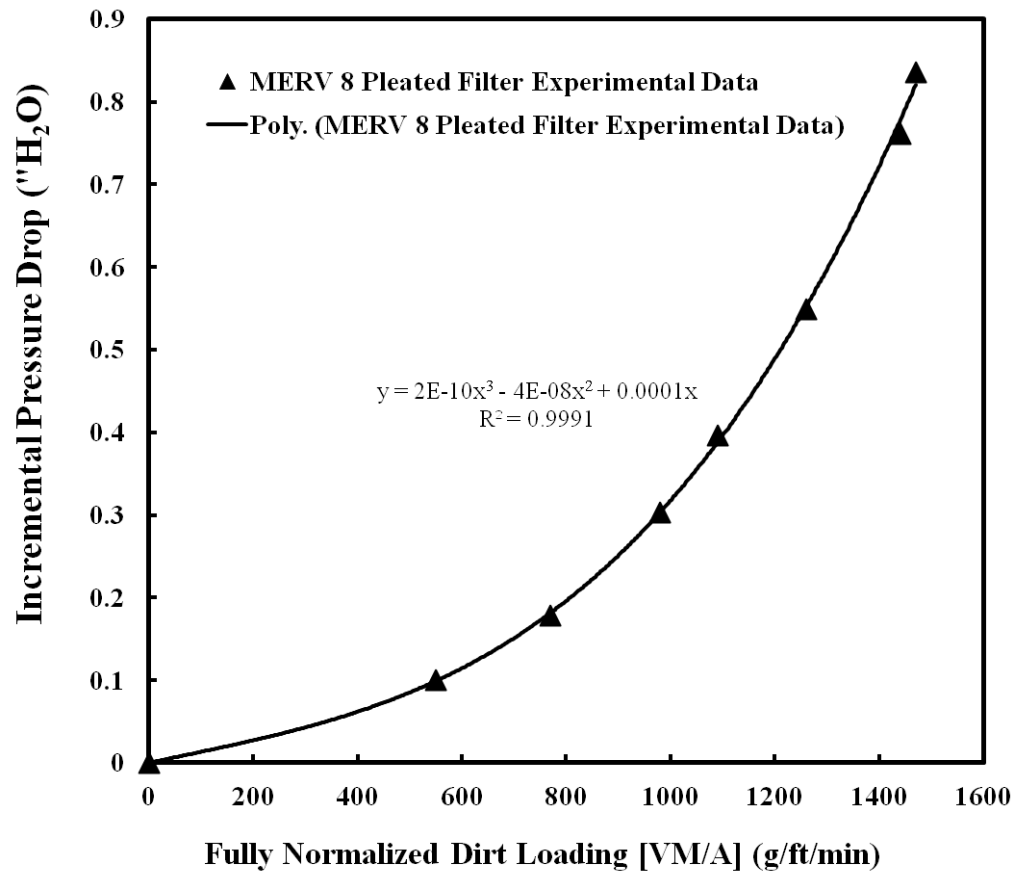


Figure 6.4 Dirt loading curve of MERV 8 pleated filter



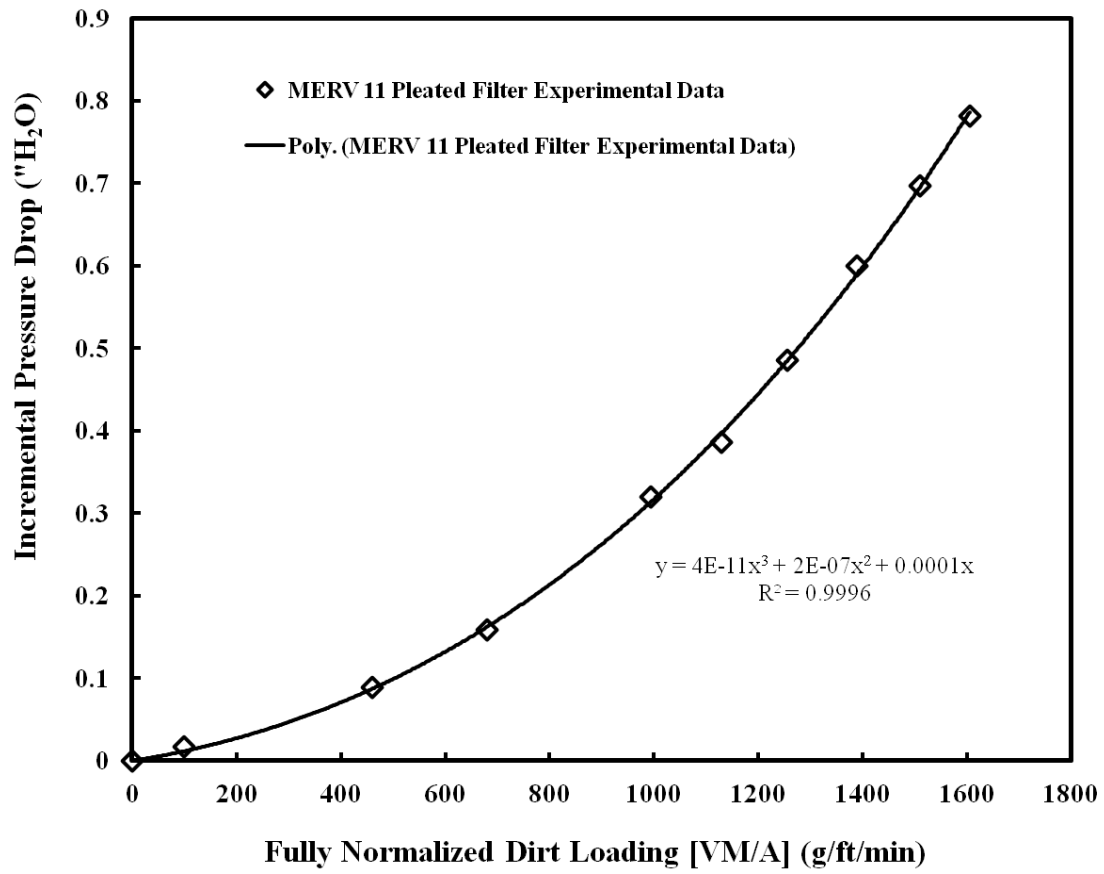


Figure 6.5 Dirt loading curve of MERV 11 pleated filter

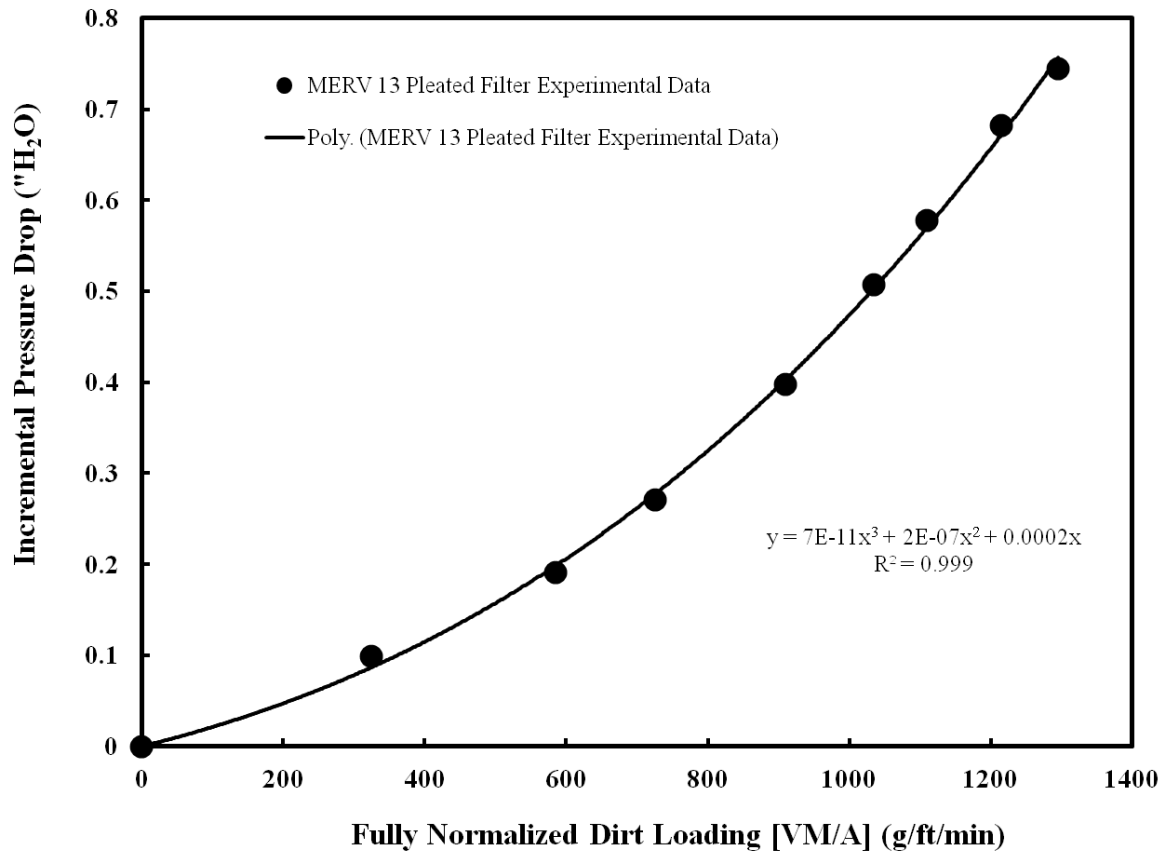


Figure 6.6 Dirt loading curve of MERV 13 pleated filter

Based on the above experimental results, an empirical pressure drop model for pleated filters during dirt loading process can be proposed as follows

$$\Delta P - \Delta P_0 = L_1 \left(\frac{VM}{A}\right)^3 + L_2 \left(\frac{VM}{A}\right)^2 + L_3 \left(\frac{VM}{A}\right) \quad (6.15)$$

Loading coefficients  $L_1$ ,  $L_2$  and  $L_3$  vary with the types of filter media. They can be determined from the above experimental results and listed in the following table.

Table 6.2 Dirt loading characterization of different MERV rank filters

Filter Rank [-]	MERV 8 Filter	MERV 11 Filter	MERV 13 Filter
Area [ft <sup>2</sup> ]	17.8	17.6	17.6
Total Loaded Dirt [g]	52.27	56.44	45.54
L <sub>1</sub> [”H <sub>2</sub> O (ft• min/g) <sup>3</sup> ]	2×10 <sup>-10</sup>	4×10 <sup>-11</sup>	7×10 <sup>-11</sup>
L <sub>2</sub> [”H <sub>2</sub> O (ft• min/g) <sup>2</sup> ]	-4×10 <sup>-8</sup>	2×10 <sup>-7</sup>	2×10 <sup>-7</sup>
L <sub>3</sub> [”H <sub>2</sub> O (ft• min/g)]	1×10 <sup>-4</sup>	1×10 <sup>-4</sup>	2×10 <sup>-4</sup>
R [-]	0.9991	0.9996	0.999

In order to verify this model, dirt loading tests were run on 1” and 4” deep MERV 8 filters. Experimental results and model calculated results are shown in Figure 6.7 and 6.8, respectively. As seen in these two figures, there are good agreements between the model predicted results and the experimental observations. It should be concluded that the proposed empirical pressure drop model can accurately predict the pressure drop of pleated filters during the dirt loading process in the turbulent flow regime.

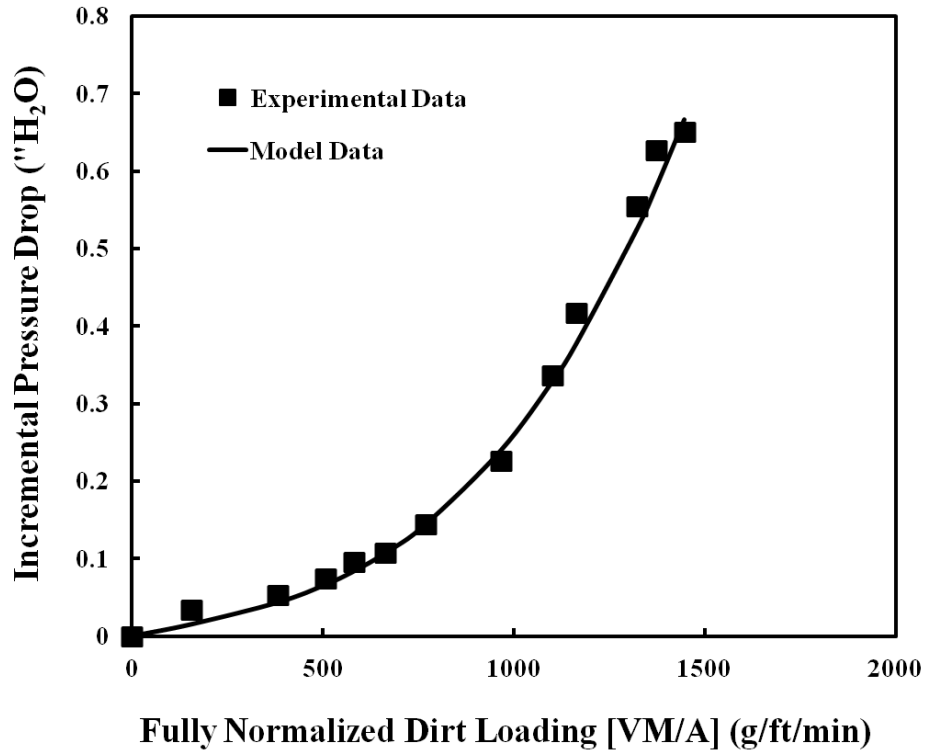


Figure 6.7 Comparison of experimental and model results for MERV 8 24" x 24" x 1" filter with 20 pleats

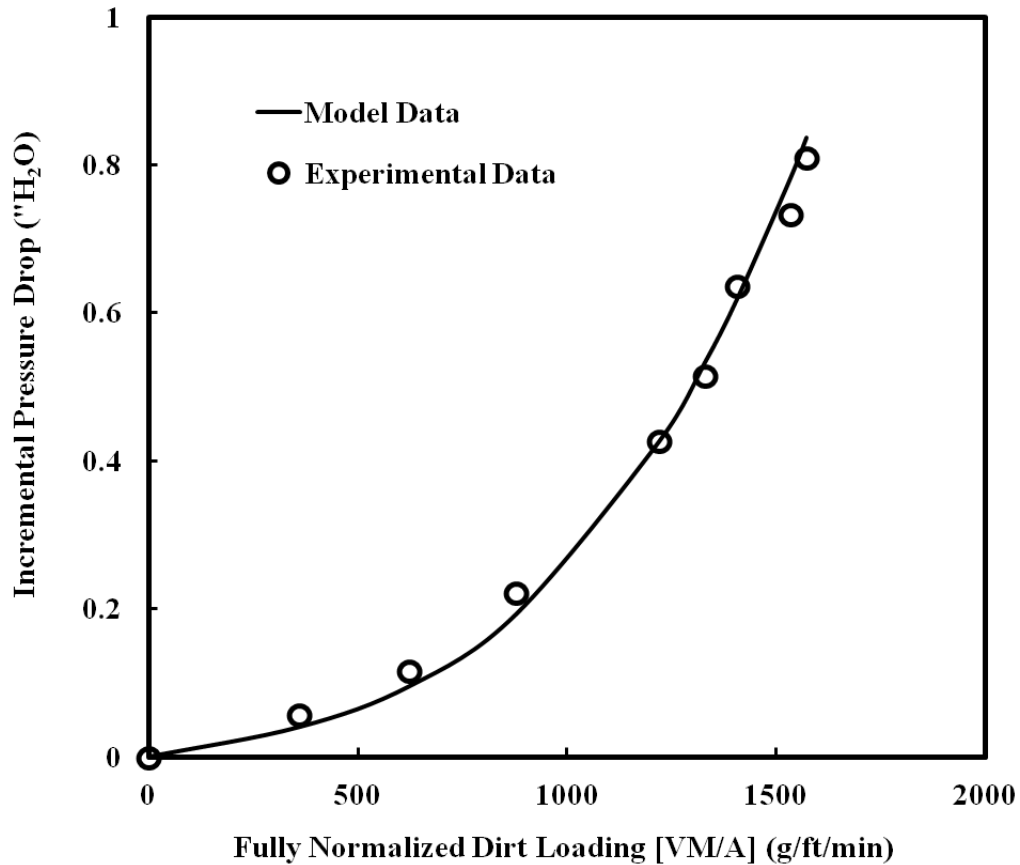


Figure 6.8 Comparison of experimental and model results for MERV 8 24" × 24" × 4" filter with 10 pleats

### 6.4.3 Effect of loading velocity

Figure 6.4, Figure 6.5, and Figure 6.6 demonstrated that the tested filters experienced the traditional two stage loading behavior characteristic of many filter types. The initial depth stage consisted of a slow growth in pressure drop as the dust was collected through the interior regions of the fibrous media. The media eventually clogged and transitioned from the depth-loading stage into the surface-loading stage. This transition was marked by a progression from the slow loading rate into a more rapid loading rate (Stenhouse and Trottier, 1991; Graef, Stenhouse and Walsh, 1995).

Earlier studies observed that the aging profiles of a given particle-fiber flow system would converge when normalized to a reference loading velocity and media utilization. Since the graphs' slopes were equal once fully normalized, face velocity was concluded to not influence the loading coefficient (Lee, Kim and Liu, 2001; Song, Park and Lee 2006). The face velocity, however, still impacted the magnitude of the pressure drop by linearly raising the drag forces on the fibers.

Figure 6.9 tested this phenomenon by measuring the resistance increase versus normalized loading rates at four different loading velocities on flat media type 1. The aging rates during the initial depth loading phase did demonstrate this convergence behavior, yet the loading plots did not overlap throughout the lifetime as with previous studies. The divergence indicated that face velocity was impacting the loading coefficient in this given particle-fiber system.

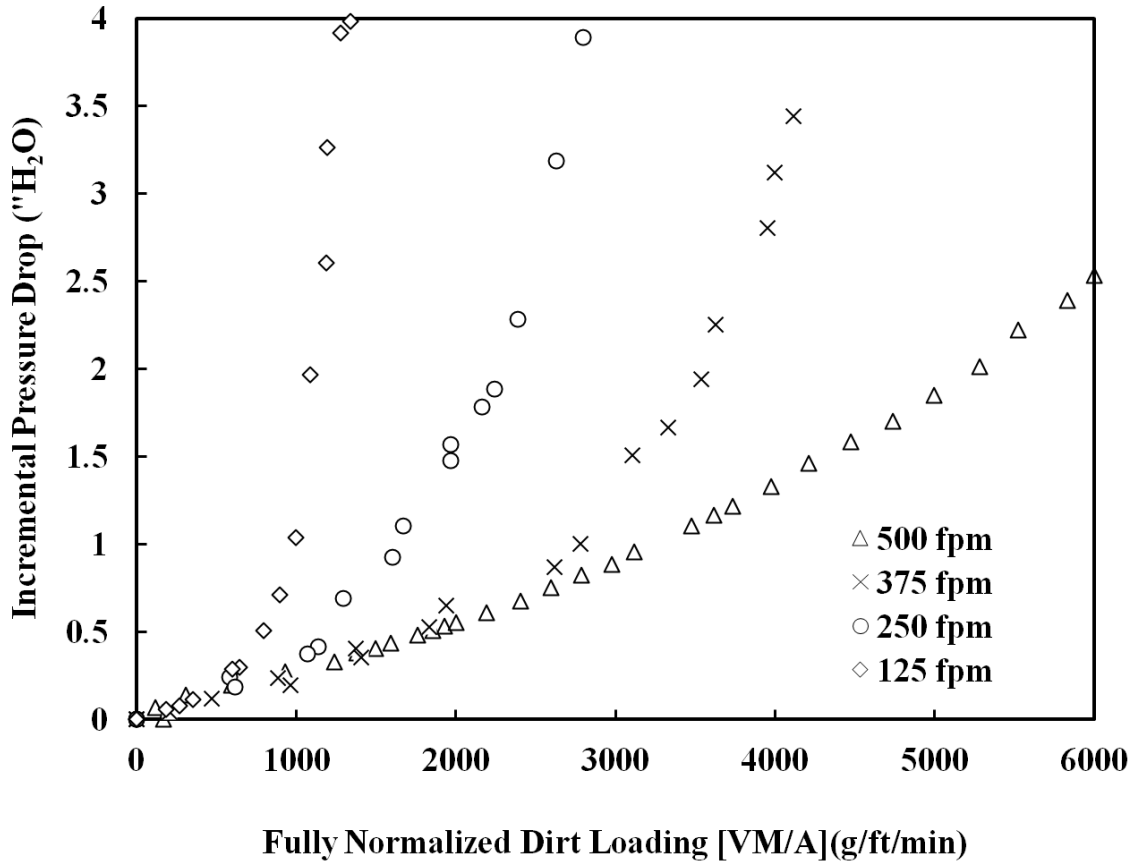


Figure 6.9 Effect of loading velocity for media type 1

Changes in face velocity affected both the transition phase to the surface loading stage and the aging rate in the surface loading stage. The onset of the transition occurred at lower media utilizations as the face velocity was decreased. Decreasing face velocity also correlated to an increase in the media aging rate once in the surface loading region. Although the quicker transition and faster aging were clearly induced by slower media velocities, it was not directly clear what filtration mechanisms were leading to these negative behaviors. The filter media was therefore systematically analyzed to examine the potential roles of enhanced efficiencies, dendrite growth, preferential layer loading, and alternative deposition patterns on the aging rate.

#### 6.4.4 Enhanced removal efficiencies

Enhanced removal efficiency due to dendrite growth was identified as a potential mechanism to influence the loading behavior (Brown, 1993). Since smaller dust particles create larger form drag forces per gram mass, a filter which is more capable of removing smaller particulates will age faster (Song, Park and Lee, 2006). A simple material balance (Equation 6.16) allowed the overall removal efficiency (E) of the filter to be calculated because the mass of dust challenged ( $M_C$ ) was known and the amount of dust captured (M) was periodically measured by pulling and weighing the filter.

$$E = \frac{M}{M_C} \quad (6.16)$$

On average, all full-size filters captured greater than 95% of the incoming challenge dust. A 4.9% coefficient of variation was observed between filters of the same media type, but no discernable trends regarding improved efficiency versus pleat count were identified among the sets.

Similarly, the formation of dendrite filaments between the media's fibers will gradually improve the removal efficiency of the filter, which would cause it to age more quickly (Brown, 1993). Under continuous loading conditions, filters capturing more dirt during a given period of time due to dendrite fiber growth would display heightened loading rates. For example, the higher loading rates towards the end of the filter's life could be attributed to greater dust capture efficiency. The efficiency was therefore also periodically computed based on the pulled and measured weights. The research observed that the filter's efficiency remained steady throughout the experiments, which indicated that enhanced removal rates due to dendrite growth was not a prominent factor.



The results were expected because higher efficiency media were used in the experimental filters to preemptively mitigate these effects. It should be noted that the impact of these phenomena might be different for other media types. In particular, filters composed of lower efficiency media might show significant improvement in removal efficiency due to lower media velocities.

#### **6.4.5 Layer penetration**

The previous removal efficiency analysis only examined the macroscopic efficiency rate of the filters, yet it was not determined if individual layer efficiencies within the media were potentially higher. Increased layer efficiency would cause the dust to preferentially load towards the surface of the media effectively blocking inner fibrous regions from being loaded. An asymmetric loading profile accelerates pressure drop and limits a filter's useful lifetime (Davis and Kim, 1999). A model filter media was used to examine the particle penetration profile at different face velocities. It was possible to disassemble the model media after a test and measure the mass of particles captured by each layer since the media was not physically bonded together. Figure 6.10 illustrates the percentage of dust penetrating the first layer of the composite media in comparison to the total loading rate. The filter's aging rates were also plotted to demonstrate the close similarity between the loading behaviors of the model and commercial filter media.

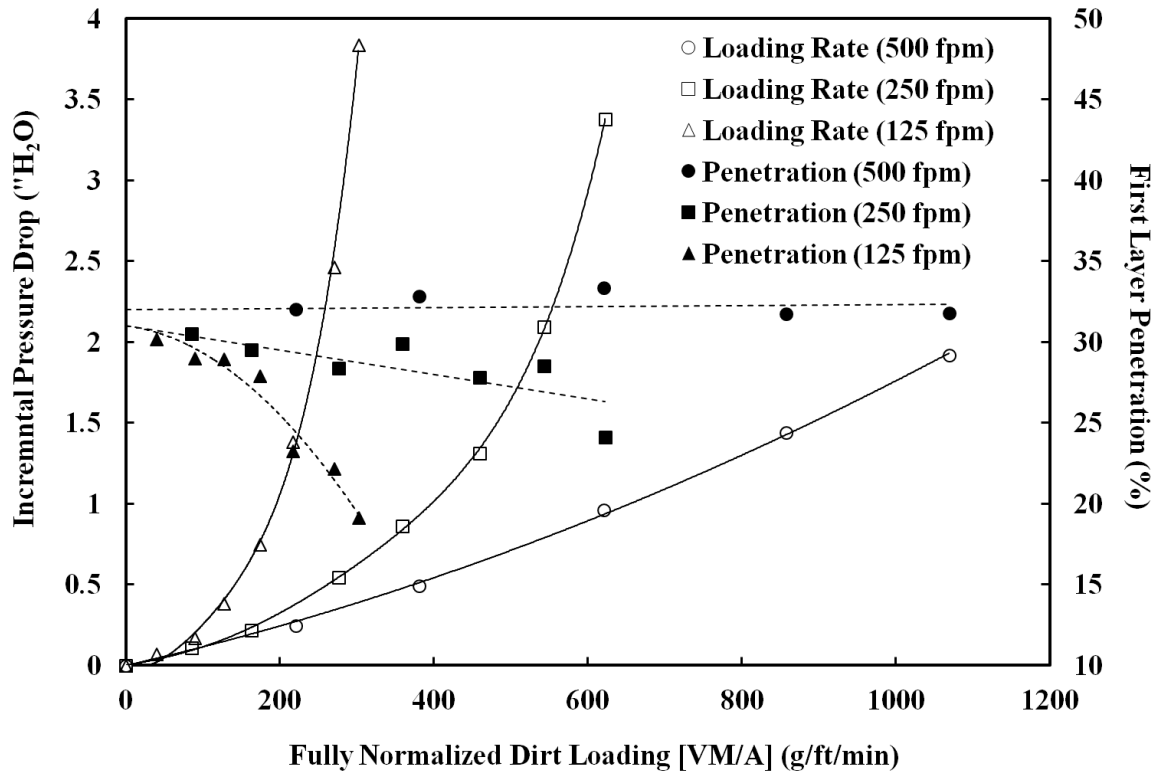


Figure 6.10 Dirt penetration and aging rates of model filter media

The samples loaded at the lower two velocities experienced a decrease in particle penetration through the first layer as more dust was captured. This decrease indicated a growth of a filter cake on the lead layer caused the removal efficiency to increase. As expected, the decrease in layer penetration coincided with an increase in the overall pressure drop. The media challenged at 500 fpm displayed no observable decrease in dust penetration, which indicated little growth of dendrite filtrate cake. Since the samples initially demonstrated a nearly identical penetration rate regardless of loading velocity, dust capture and dendrite growth would be expected to occur at similar rates. Clearly, the growth of the dendrite filaments is much higher at the lower velocities as seen in the more rapid penetration rate declines and reciprocating increase in pressure drop.

#### 6.4.6 Variations in deposition patterns

In order to explain this occurrence, the deposition patterns of the model layers at various velocities were qualitatively examined. The manner of particulate deposition impacts the pressure drop by altering the cross-sectional area of the dust loaded fibers. Particles loaded by impaction agglomerate at the front of the fiber. The resulting oval-shaped deposition pattern possesses a cross-section that is aerodynamically similar to the capturing fiber; thus, pressure drop will not greatly increase. As a particle's inertia drops into the interception regime, the deposition method shifts from loading at the fiber's front stagnation point to capture around the front circumference of the fiber. Particles entrapped around the front perimeter create wide, branched structures that possess high form drag coefficients. These branched structures impact efficiency by actively decreasing the average pore diameter (Japuntich, Stenhouse and Liu, 1994).

The general transition from impaction to interception occurs when the Stokes number for the flow in the particle-fiber system drops below one (Brown, 1993). Stokes number is the ratio of particle stopping distance to fiber diameter as shown in Eq. 6.17, and it can be used to predict a particle's ability to follow streamlines.

$$St = \frac{\rho_p D_p^2 V}{18\mu D_f} \quad (6.17)$$

The flat model media, flat commercial media, and full-sized filters were loaded with a polydispersed particle challenge that possessed diameters ( $D_p$ ) between 1~100  $\mu\text{m}$  over a range of face velocities from 125 to 500 fpm. Additionally, the fiber's diameters ( $D_f$ ) were between 5~10 micrometers. Based on these flow conditions, the deposition pattern of particulates in the

range of 20 to 50  $\mu\text{m}$  were shifted from impaction to interception. The Stokes number of approximately 20% of the dust dropped below one as face velocity decreased.

The rapid rise in pressure drop and increase in removal efficiency of the highly pleated filter was attributed to the creation of branched formations brought about by the new deposition patterns. Scanning electronic micrographs (SEM) were used to qualitatively verify this effect by examining the model filter samples aged at 125 fpm, 250 fpm and 500 fpm over the course of aging. The images provided in Figures 6.11 through 6.13 are showing the top layer of model media loaded at different face velocity after the 2<sup>nd</sup>, 6<sup>th</sup> and final dirt load. As shown in these figures, a higher face velocity resulted in a slightly more coverage at the same loading stage. This observation is consistent with the aging curve of media at different face velocities. As more dust was captured, the pore diameters of media loaded at lower velocities began to close because wider dendrite fibers were generated. The early formation of a particulate web was particularly evident at fiber junctions (Figure 6.12 B). The web continued to grow until the entire porous structure was encased (Figure 6.13 B). This encasement is accompanied with a very steep loading coefficient. Figure 6.13 C shows that the porous structure was still readily visible even at the end of the run. These images confirm that lower loading velocities will negatively impact the useful lifetime by promoting the formation of dendrite fibers in foremost media layers.



Figure 6.11 SEM image of the top layer of model media loaded at different face velocity after the 2nd dirt load: (A) 125 fpm (B) 250 fpm (C) 500fpm

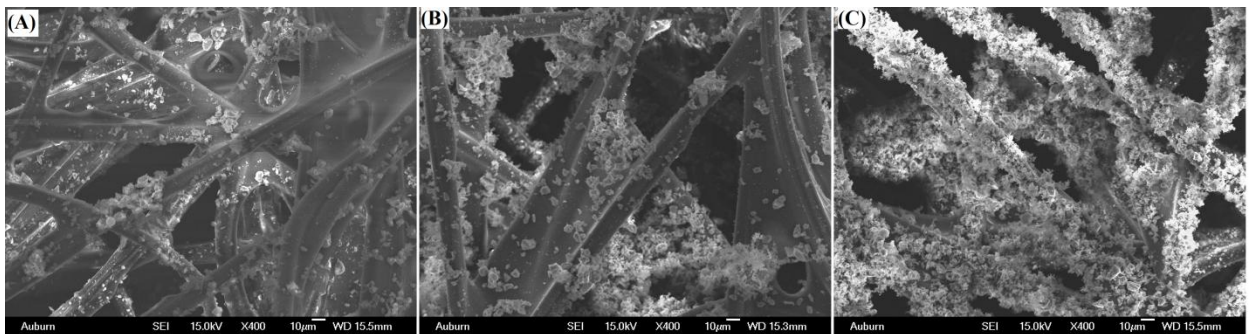


Figure 6.12 SEM image of the top layer of model media loaded at different face velocity after the 6<sup>th</sup> dirt load: (A) 125 fpm (B) 250 fpm (C) 500fpm

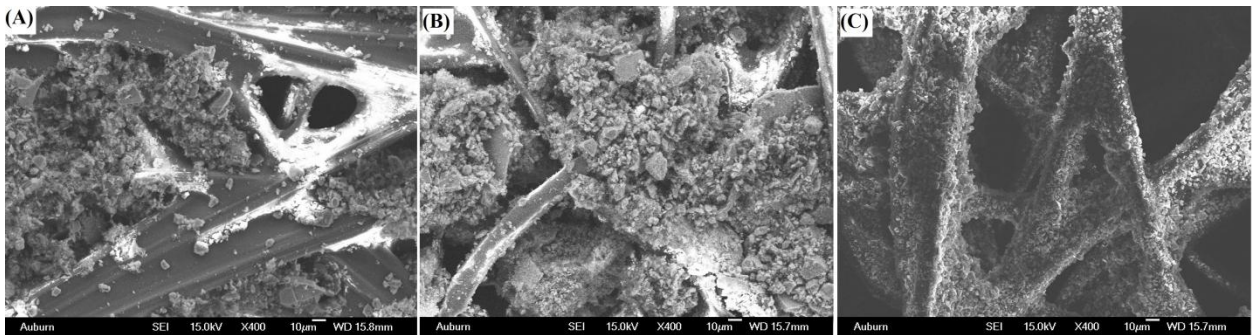


Figure 6.13 SEM image of the top layer of model media loaded at different face velocity after the final dirt load: (A) 125 fpm (B) 250 fpm (C) 500fpm

The discrepancy between previously published work and the current work in regards to the influence of face velocity on aging rates can be explained by this behavior. The previous

studies loaded monodispersed, submicron particles at face velocities below 78 fpm on 1 micrometer fibers (Lee, Kim and Liu, 2001; Song, Park and Lee, 2006). This loading regime resulted in very small Stokes numbers ( $\ll 1$ ) for all of test conditions. Filtration theory denotes the capture mechanism in very low Stokes flow occurs by Brownian diffusion (Brown, 1993). Since the filtration mechanism did not change throughout the course of the previous studies, the deposition pattern remained constant, which renders the loading coefficient unaffected by differing face velocities.

## **6.5 Conclusions**

The present study provides insight into novel methods to improve future filter and media designs to enhance the performance of traditional filtration applications. It was observed that the optimal pleat count related the minimal initial pressure drop does not match with the optimal pleat count corresponding to the maximal dirt loading. In order to achieve significantly improved total dust holding capacities, pleated filters should be pleated beyond the traditional minimal optimal pleat count. However, this may slightly increase the initial pressure drop, but pleated filters designed by this increased pleating approach would decrease the frequency and costs associated with downtime change outs when used in combinational pre-filter/HEPA filter systems. Another drawback to the high pleating approach is a loss in the average media utilization; thus, this technique might not be suitable in all situations. In particular, the utilization of high end filter media such as those composed of metal fibers or adsorbent materials must be assessed with regard to the cost-benefit ratio of the life extension versus the procurement cost. In addition, an empirical model for pleated filters during dirt loading process was developed to predict pressure drop during the dirt loading process in turbulent regime.

Experimental results and model calculation for different MERV 8 pleated filters show a good agreement.

Removing the cardboard grating is a second potential technique to improve a traditional filter design. The presence of the cardboard frame decreases media utilization as well as adds extra resistance to the filter. An expanded metal wire backing would supply sufficient support to a pleated media without unnecessarily blocking a portion of the incorporated media area. This increase in media utilization and increase in operational window would help extend the filter's lifetime.

Understanding the mechanisms that cause pleated filters to transition into the surface loading stage is critical to maximizing the useful life and capitalizing on the additional area being utilized. The realization that lower media velocities translate into poorer media utilization should be used to tailor specific media types for low velocity filtration application such as variable air volume (VAV) units or proton exchange membrane (PEM) fuel cells. These low flow systems should utilize filtration media with larger void volume towards the front of the filter. The increased porosity would delay the formation of dendritic webs and allow higher utilization of the interior regions thereby increasing energy efficiency and cost effectiveness of the unit.

## **Chapter 7 Design of Microfibrous Materials in Multi-Element Structured Arrays**

### **7.1 Introduction**

Gas phase filters are typically deep bed filters loaded with sorbent materials, such as activated carbon, activated alumina, silica gel, zeolites, molecular sieves, porous clay minerals, or engineered polymers. Once the sorbents are spent, gas phase filters must be replaced or regenerated by application of heat or other processes. Factors affecting gas phase filter life include removal capacity, sorbent loading capacity, sorbent collection efficiency, airflow rates, molecular weight, and the concentration of the targeted contaminant. Among those parameters, sorbent loading capacity plays an important role on service life of the filtration system. The ability to load more sorbent correlates to longer service life.

As a novel platform that integrates multiple pleated filter elements into a single filtration system, MESA shows obvious benefits for reducing pressure drop which has been discussed in Chapter 5. Apparently MESA can increase sorbent loading capacity due to the integration of multiple filter elements. However, the sorbent loading capacity of different MESA configurations has not been previously investigated. In this chapter, the sorbent loading capacity of various MESA units will be estimated by applying a developed semi-empirical pressure drop model for MESA units. In addition, optimal design of a MESA unit based on the minimal initial pressure drop and maximal sorbent loading capacity will be conducted. Furthermore, sorbent loading capacity of other structures, such as packed bed and composite bed will be compared



with that of the optimal MESA unit for determining a longer gas life filtration unit. Since activated carbon is the most common sorbent used in HVAC systems and it excels in capturing most organic chemicals, it will be selected as the model sorbent.

## 7.2 Model Description

Sothen (2009) has developed a semi-empirical pressure drop model capable of predicting the resistance of MESA units. The total flow resistance through a MESA unit was compiled as a summation of eleven individual resistances. The individual resistances were formulated by applying Bernoulli's equation or Forchheimer-extended Darcy's law as follows:

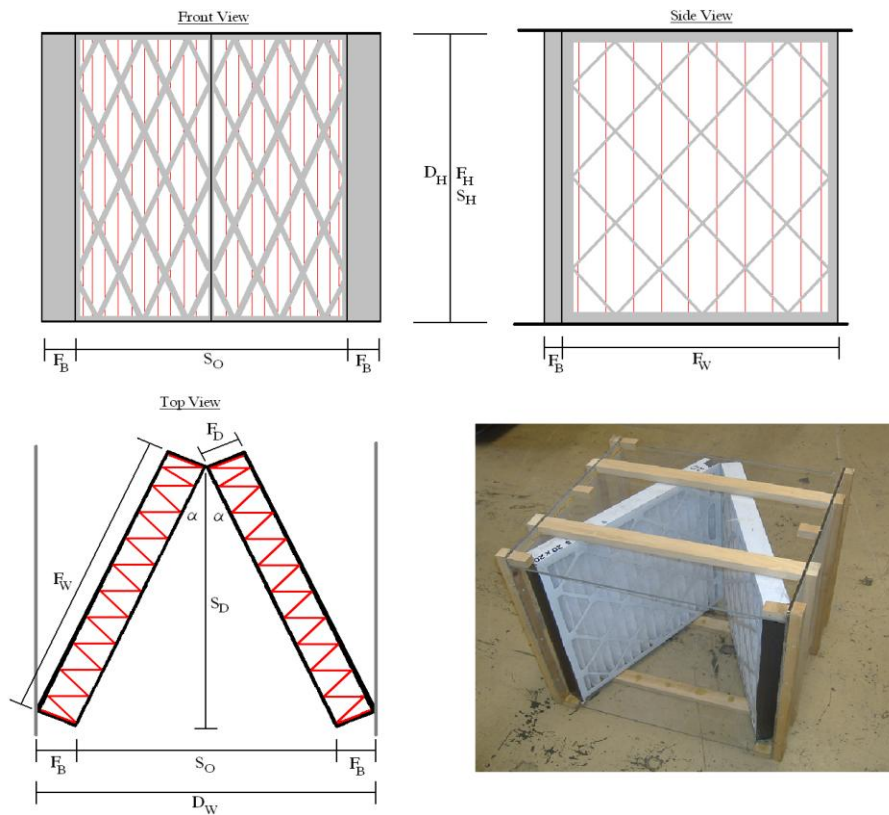


Figure 7.1 General schematic of a MESA unit (Sothen, 2009)

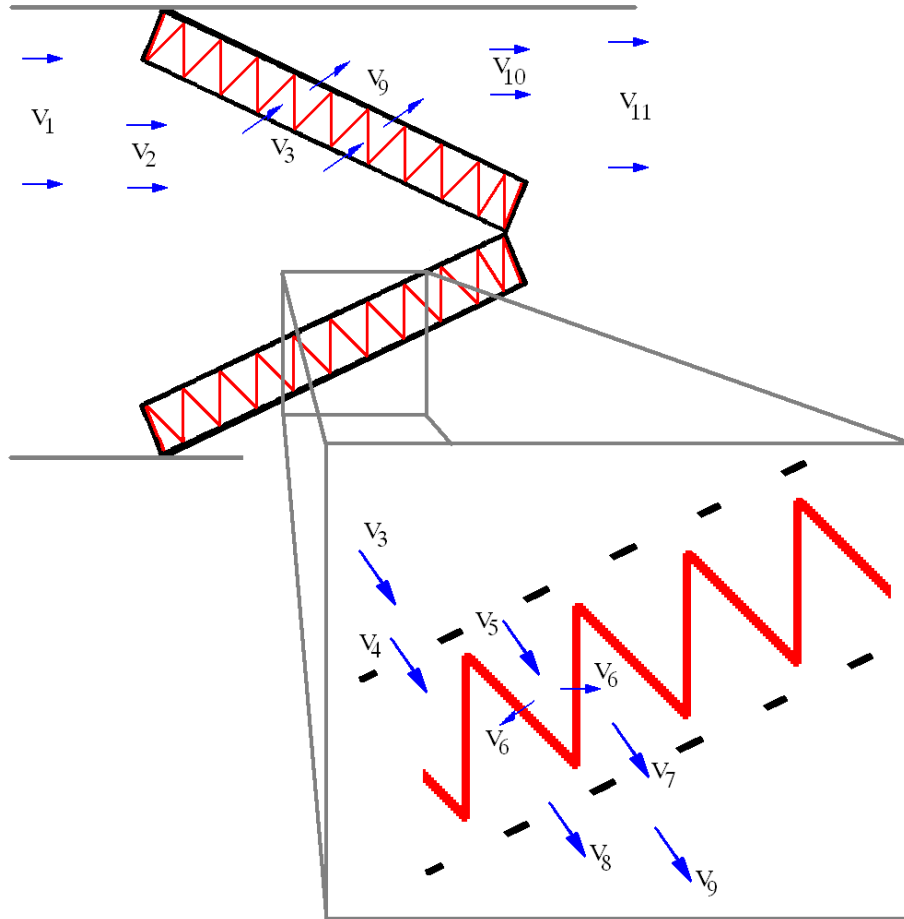


Figure 7.2 Proposed flow pattern (Sothen, 2009)

Flow into Slot:

Flow from Slot Inlet to Filter Face:

Across Front Grating:

Flow from Grating to Pleat Inlet:

Flow from Pleat Inlet to Media Surface:

Flow through Media:

Flow from Media Surface to Pleat Outlet:

Expansion from Pleat Outlet into Grating:

Across Back Grating:

Flow from Filter Face to Slot Outlet:

Flow out of Slot:

$$\Delta P_1 = \frac{1}{2} \rho [(V_2^2 - V_1^2) + K_{CB} V_2^2]$$

$$\Delta P_2 = \frac{1}{2} \rho [(V_3^2 - V_2^2) + K_{S1} V_3^2]$$

$$\Delta P_3 = \frac{1}{2} \rho [(V_4^2 - V_3^2) + K_G V_3^2]$$

$$\Delta P_4 = \frac{1}{2} \rho [(V_5^2 - V_4^2) + K_{CP} V_5^2]$$

$$\Delta P_5 = \frac{1}{2} \rho [(V_6^2 - V_5^2) + K_{P1} V_5^2]$$

$$\Delta P_6 = A V_6 + B V_6^2$$

$$\Delta P_7 = \frac{1}{2} \rho [(V_7^2 - V_6^2) + K_{P2} V_7^2]$$

$$\Delta P_8 = \frac{1}{2} \rho [(V_8^2 - V_7^2) + K_{EP} V_7^2]$$

$$\Delta P_9 = \frac{1}{2} \rho [(V_9^2 - V_8^2) + K_G V_9^2]$$

$$\Delta P_{10} = \frac{1}{2} \rho [(V_{10}^2 - V_9^2) + K_{S2} V_9^2]$$

$$\Delta P_{11} = \frac{1}{2} \rho [(V_{11}^2 - V_{10}^2) + K_{EB} V_{10}^2]$$

The total pressure drop across a MESA unit is the summation of the above eleven individual resistance as the following expression:

$$\Delta P_T = \sum \Delta P_i = \Delta P_1 + \Delta P_2 + \Delta P_3 + \Delta P_4 + \Delta P_5 + \Delta P_6 + \Delta P_7 + \Delta P_8 + \Delta P_9 + \Delta P_{10} + \Delta P_{11} \quad (7.1)$$

After making the appropriate substitutions by utilizing the upstream/downstream symmetry and the equation of continuity, the total pressure drop across a MESA unit can be re-written into the following expression:

$$\Delta P_T = \frac{1}{2} \rho [(K_{CB} + K_{EB})V_2^2 + (2K_G + K_S)V_3^2 + (K_{CP} + K_{EP} + K_P)V_5^2] + AV_6 + BV_6^2 \quad (7.2)$$

$K_{CB}$  and  $K_{EB}$  stand for the friction coefficients for a sudden contraction and expansion due to the flow change in and out of the array.  $K_G$  is the friction coefficient due to the grating support on the filter element.  $K_S$  is the combined friction coefficient encountered in the slots upstream and downstream of the filter elements.  $K_{CP}$  and  $K_{EP}$  stand for the friction coefficients for a sudden contraction and expansion due to the pleat tips.  $K_P$  indicates the pleat tip coefficient. A and B are media constants. Among these nine parameters, A, B,  $K_G$ ,  $K_{CP}$ ,  $K_{EP}$  and  $K_P$  were determined by the research presented in Chapter 4.  $K_{CB}$  and  $K_{EB}$  were calculated by the following formula:

$$K_{CB} = \frac{1}{2} \left(1 - \frac{A_{Free}}{A_{Total}}\right)^{0.75} \quad (7.3)$$

$$K_{EB} = \left(1 - \frac{A_{Free}}{A_{Total}}\right)^2 \quad (7.4)$$

$K_S$  was determined by analyzing empirical data spanning 32 MESA systems (Sothen, 2009) and formulated as follows:

$$K_S = 2.575 \left(\frac{1}{\alpha}\right)^2 \quad (7.5)$$

## 7.3 Results and Discussion

### 7.3.1 Utilization of MESA pressure drop model

MFM No. 1 was selected as the model media to make a pleated MFM filter. The preparation method was described in Chapter 4. Its characteristic parameters are listed in Table 7.1. According to the simulated results in Chapter 4, the filter dimension selection was 24" × 24" × 2" since the two inch deep filter has the lowest initial pressure drop. The pleat count was selected as 36 randomly.

Table 7.1 Characteristic parameters of MFM No.1

Thickness (inch)	0.0717
A ("H <sub>2</sub> O×min / ft)	4.0×10 <sup>-4</sup>
B ("H <sub>2</sub> O×min <sup>2</sup> / ft <sup>2</sup> )	7.0×10 <sup>-7</sup>
Basis Weight (g/m <sup>2</sup> )	200
Carbon Loading (wt) %	65

By applying the MESA pressure drop model developed by Sothen (Sothen, 2009), the initial pressure drops of single MFM filter, V-shaped MFM MESA, W-shaped MFM MESA and WV-shaped MESA in the face velocity range of 0~900 fpm were calculated and the results were plotted in Figure 7.3. As depicted in this figure, the initial pressure drops of all of the MESA units are significantly lower than that of the single MFM filter. This is in good agreement with our experimental results in Chapter 5 for particle removal filters. Among the three different MESA configurations, the W-shaped MESA has the lowest initial pressure drop. This simulated result is in good agreement with the experimental results shown in Chapter 5 as well. It is indicated that the slot resistance plays an important role during the overall initial pressure drop of MESA structures.

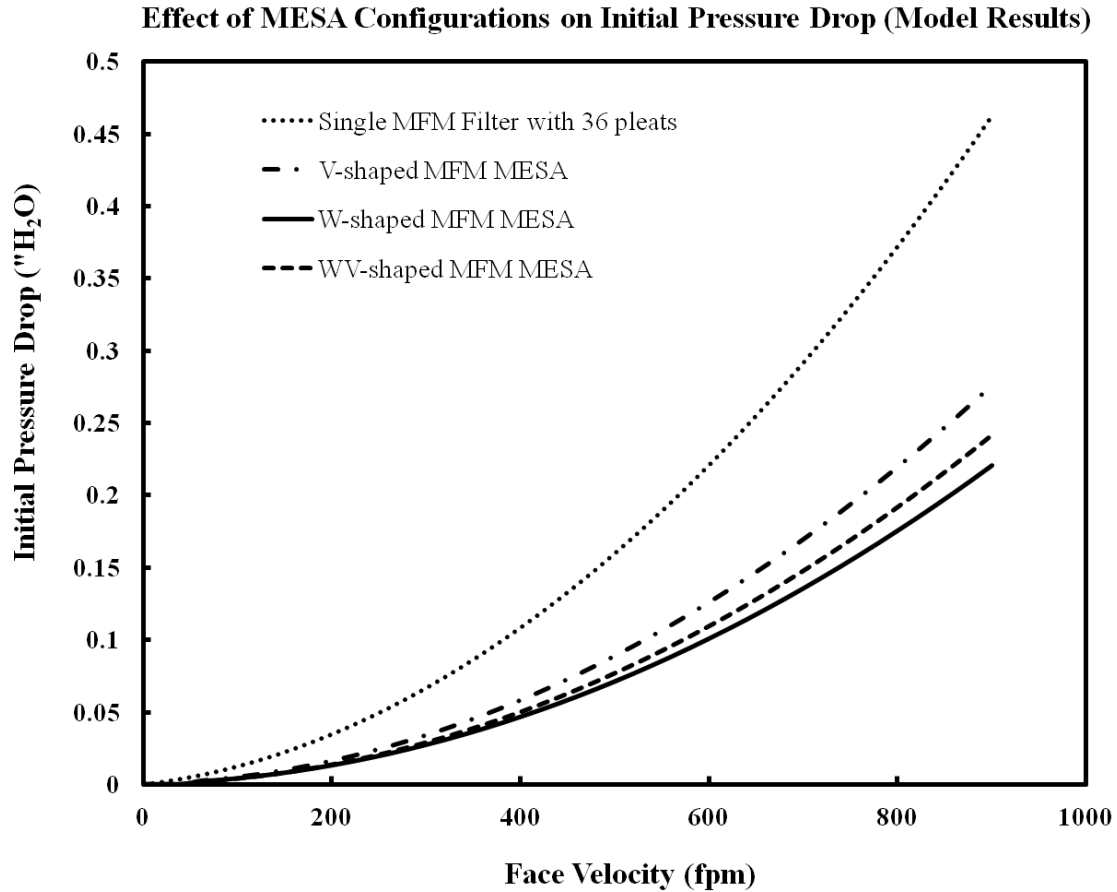


Figure 7.3 Comparison of initial pressure drop of single MFM filter and various MESA configurations (model simulation results)

In order to show the difference in quantity, the initial pressure drops of different filtration unit at 500 fpm were listed in Table 7.2. As shown in this table, compared with the single MFM filter, V-shaped MESA can reduce the initial pressure drop by 44.4%; W-shaped MESA can reduce the initial pressure drop up to 55.6%; WV-shaped MESA can reduce the initial pressure drop by 51.9%. Due to the obvious pressure drop reduction of MESA units, it can be expected that energy consumption can be reduced by applying this special filter housing design.

Table 7.2 Comparison of initial pressure drop at 500 fpm of different MFM filtration units

	<b>Initial Pressure Drop</b> <b>( " H<sub>2</sub>O )</b>	<b>Improvement</b> <b>( - )</b>
Single Filter	0.160	N/A
V-shaped MESA	0.089	44.4%
W-shaped MESA	0.071	55.6%
WV-shaped MESA	0.077	51.9%

### 7.3.2 Optimization of MFM MESA units regarding to initial pressure drop

Based on the previous results on the single MFM filter in Chapter 4, there also should exist an optimal pleat count for differing MFM MESA configurations. Applying the MESA pressure drop model, initial pressure drops at 500 fpm for each MESA configuration inserted by 24" × 24" × 2" single MFM filter with various pleats were calculated. Figure 7.4 shows the model results. It can be seen that there exists an optimal pleat number corresponding to minimum initial pressure drop for each MFM filtration structure as expected. Similarly with single MFM filter, a typical "U" curve is showing the relationship of initial pressure drop verses pleat counts for V-shaped MESA unit. However, for W-shaped MESA and WV-shaped MESA, the "U" curves become much wider. It can be concluded that the effect of pleat counts for the initial pressure drops of W-shaped MESA and WV-shaped MESA is not as obvious as that for V-shaped MESA's initial pressure drop. This observation is in a good agreement with the experimental results shown in Chapter 5. In Chapter 5, the experimental results on W-shaped MESA units loaded with 24" × 24" × 2" particle filters that have different pleat counts did not show obvious differences. The agreements with experimental results indicated that the MESA

pressure drop model has very good prediction capabilities, which can be used as a design tool to help optimize MFM MESA design.

### Effect of Filter Packing Structure (Model Result)

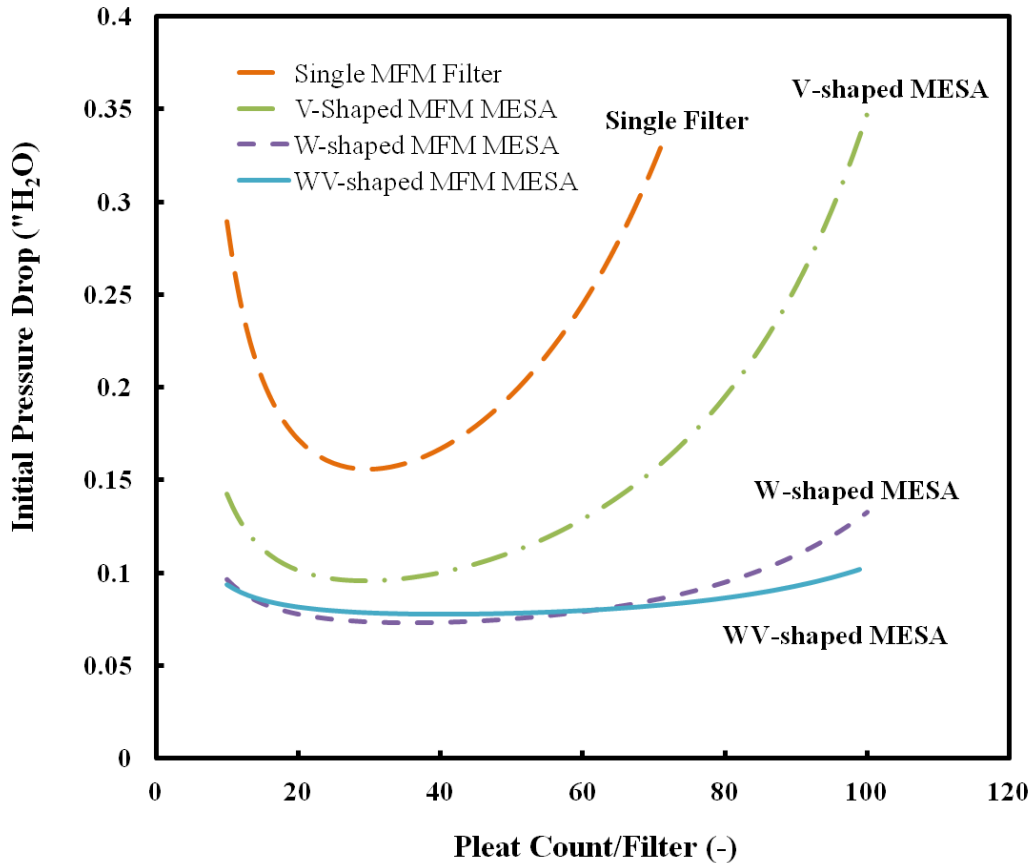


Figure 7.4 Comparison of initial pressure drop of different MFM filtration units

The optimal pleat number and its corresponding minimum initial pressure drop for each filter packing structure were summarized in Table 7.3. It can be seen that the optimal pleat number for each structure increases with the enlargement of element numbers in the MESA unit. However, the initial pressure drop reached its minimum value of 0.073" H<sub>2</sub>O when four MFM filters with 36 pleats form a W-shaped MESA, which is consisted with the simulated results shown in Section 7.3.1. The initial pressure drop of the same single filter (24" × 24" × 2" MFM filter with 36 pleats is about 0.160 "H<sub>2</sub>O, which is more than two times of that for W-

shaped MESA unit equipped with the same filter element. Therefore, W-shaped MESA is the optimal MESA design for 24" × 24" × 2" MFM filters with 36 pleats with regard to initial pressure drop.

Table 7.3 Optimal pleat count of different MFM filtration units

	<b>Optimal Pleat (-)</b>	<b>Minimum Initial Pressure (" H<sub>2</sub>O)</b>
Single Filter	28	0.156
V-shaped MESA	29	0.095
W-shaped MESA	36	0.073
WV-shaped MESA	44	0.078

### 7.3.3 Carbon loading capacity of MFM MESA units

For gas phase filters, aside from initial pressure drop, carbon loading capacity is also a very important parameter, since it is directly related to the gas life and changeout time of a filtration unit. The MESA pressure drop model was applied to investigate the effect of different MESA configurations on carbon loading capacity.

Figure 7.5 shows the relationship of initial pressure drop with carbon loading capacity for single MFM filter and different MFM MESA configurations. As shown in this figure, the W-shaped MFM MESA reaches the lowest minimal initial pressure drop (0.073" H<sub>2</sub>O) when carbon loading equals to 988 g per unit among the three different MESA configures. Similarly, the WV-shaped MFM MESA unit reaches its minimal initial pressure drop (0.078" H<sub>2</sub>O) when carbon loading equals 1646 g per unit. Table 7.4 summarizes the minimal initial pressure drop and corresponding carbon loading capacity for each filtration unit. Compared with single MFM filter, the W-shaped MFM MESA can reduce the initial pressure drop up to two times while increasing the carbon loading capacity by five times. It was found that the WV-shaped MFM



MESA has the similar minimal initial pressure drop to that of the W-shaped MFM MESA, however, the carbon loading of the WV-shaped MFM MESA is 1.67 times of that of the W-shaped MFM MESA. Considering the combined benefits of initial pressure drop and carbon loading, WV-shaped MESA should be the best design option.

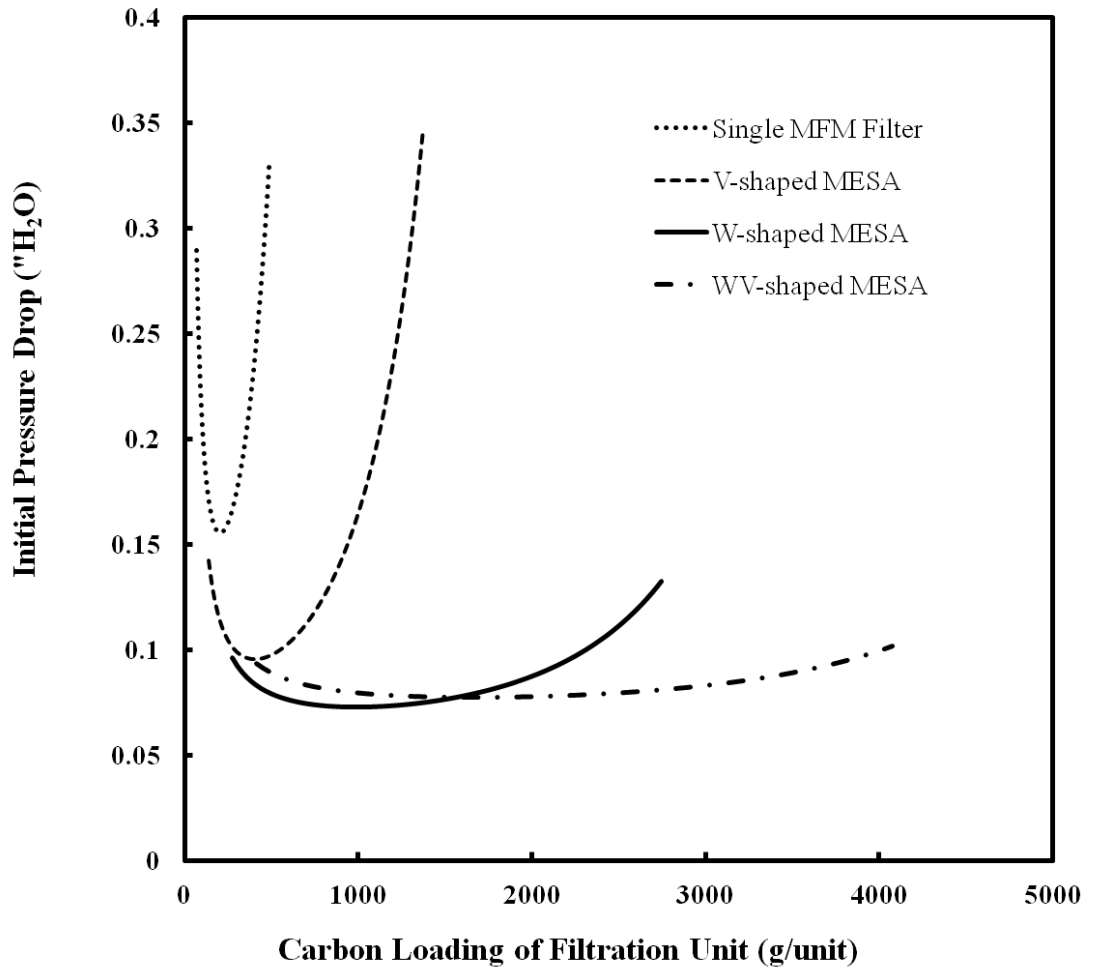


Figure 7.5 Effect of filtration unit structures on carbon loading capacity

Table 7.4 Effect of filtration unit structures on carbon loading capacity

	<b>Carbon loading (g/unit)</b>	<b>Minimum Initial Pressure Drop (" H<sub>2</sub>O)</b>
Single Filter	192	0.156
V-shaped MESA	398	0.095
W-shaped MESA	988	0.073
WV-shaped MESA	1646	0.078

### 7.3.4 Comparison of packed bed and MFM MESA units

Packed-bed absorbers are the most common absorbers used for gas removal (Figure 7.6). In this design, adsorbents such as granular activated carbon, zeolite pellets are packed randomly in a hollow tube, pipe, or other vessel. The primary purpose of the packing material is to provide a large surface area for mass transfer, then improve the contact between two phases (adsorbents and gas). Sorbent loading capacity is directly related to the gas life of a filtration unit. Higher sorbent loading capacity means longer service life of the unit. Therefore, from the design standpoint, sorbent loading capacity and pressure drop should be the primary parameters when designing a gas scrubber.

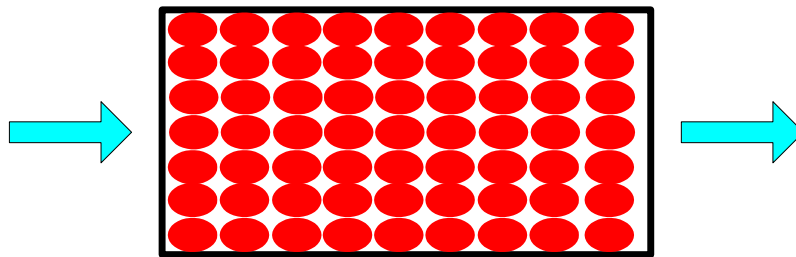


Figure 7.6 Schematic of packed bed

In air filtration, various carbon filters of packed-bed design are commercially available and widely used. Figure 7.7 is a photograph of a one inch deep honeycomb carbon filter (24" × 24" × 1") which was purchased from Grainger.



Figure 7.7 Picture of 1" deep commercial honeycomb carbon filter

The honeycomb carbon filter (HCF) can be employed in the MESA boxes to form different honeycomb carbon filter MESA units. Initial pressure drop tests on single honeycomb filter, V-shaped MESA unit and W-shaped MESA unit were carried out and the results are plotted in Figure 7.8. As expected, during the face velocity test range (0~700 fpm), the W-shaped MESA displays the lowest initial pressure drop compared with the other two filtration units. Initial pressure drop at 500 fpm and carbon loading of the three filtration units are listed in Table 7.5. As seen in the table, the W-shaped MESA can be loaded with four times more carbon at 1/7 of the initial resistance of single honeycomb carbon filter. These results further confirm the benefits of MESA structures for reducing pressure drop and increasing sorbent

loading capacity. Therefore, MESA structure can be used as a design platform for commercially available filters.

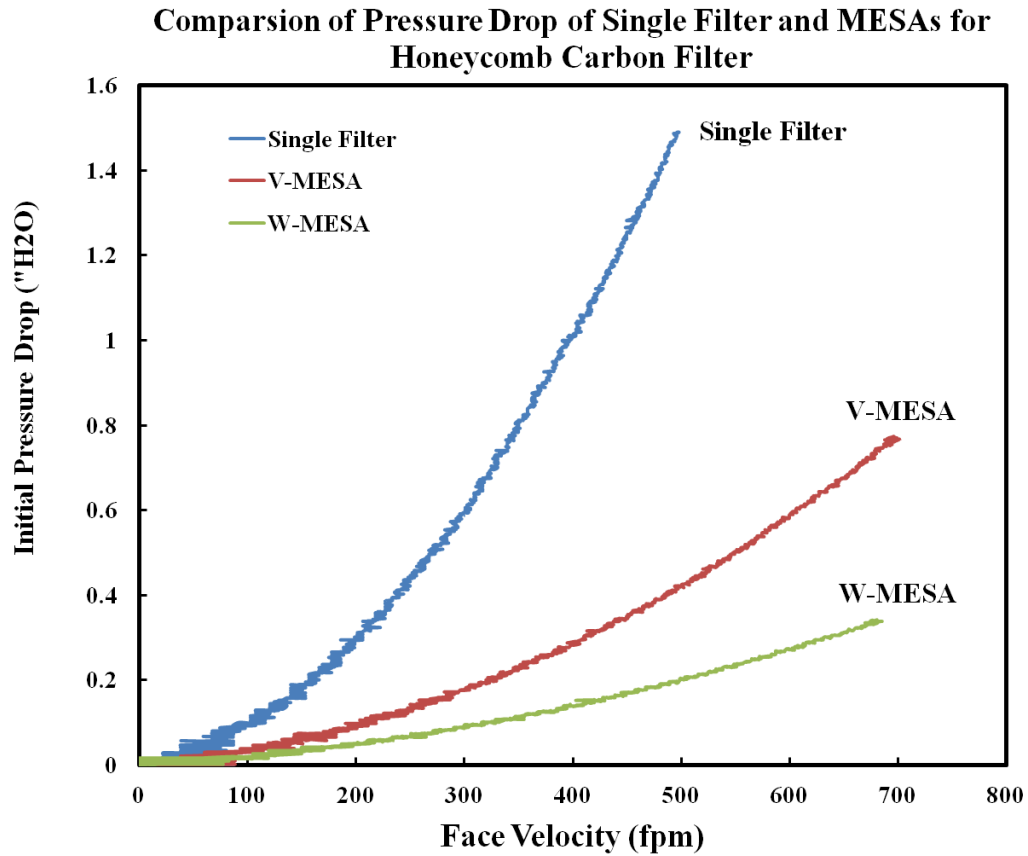


Figure 7.8 Comparison of initial pressure drop of various configurations of honeycomb carbon filter

Table 7.5 Comparison of various configurations of honeycomb carbon filter

<b>Filtration Unit</b>	<b>Initial Pressure Drop at 500 fpm (\" H<sub>2</sub>O)</b>	<b>Carbon Loading (g/unit)</b>
Single Filter	1.49	1270
V-shaped MESA	0.42	2540
W-shaped MESA	0.20	5080

Based on the simulated results in Section 7.3.2 and 7.3.3 and experimental results in Section 7.3.4, we compared the filtration performance of single MFM filter, single HCF filter and different MESA units containing either MFM filters or HCF filters. Table 7.6 summarizes

the initial pressure drop at 500 fpm, carbon loading capacity per unit and performance for each filtration unit. It can be seen that compared to the commercial 1" deep honeycomb carbon filter, the single MFM filter shows an obvious improvement in carbon loading to initial pressure drop ratio. Among all of the filtration units, W-shaped MESA contained HCF has the best performance. When loaded with a similar amount of activated carbon, MFM WV-MESA can be operated at 1/19 of the initial resistance of single HCF. From the energy efficiency standpoint, MFM single filters and MESA units have the huge potential for energy saving in some environments with low concentration of contaminant gases.

Table 7.6 Comparison of MFM MESA units and HCF MESA units

<b>Filtration Unit</b>	<b>Initial Pressure drop (" H<sub>2</sub>O)</b>	<b>Carbon Loading (g/unit)</b>	<b>Performance<sup>1</sup> (g/unit/" H<sub>2</sub>O)</b>
Single MFM	0.156	192	1231
MFM V-MESA	0.095	398	4189
MFM W-MESA	0.073	988	13534
MFM WV-MESA	0.078	1646	21103
Single HCF	1.49	1270	852
HCF V-MESA	0.42	2540	6048
HCF W-MESA	0.20	5080	25400

1-Performance represents carbon loading to initial pressure drop ratio

## 7.4 Conclusions

The developed semi-empirical pressure drop model for MESA structures was employed to design MFM MESA units. Model simulation results show that W-shaped MFM MESA displays the lowest initial pressure compared to single MFM filter, V-shaped MFM MESA and WV-shaped MESA, which is in good agreement with the experimental tests for various MESA configurations containing particulate filters. Considering both of carbon loading capacity and

initial pressure drop, WV-shaped MFM MESA should be the optimal design because it can load 1.67 times the carbon compared to the WV-shaped MFM MESA with slightly higher initial pressure drop.

In order to reduce the pressure drop and increase carbon loading capacity, commercially available honeycomb carbon filter can be loaded in MESA structures as well. Experimental results of initial pressure drop tests on single honeycomb carbon filters, V-shaped MESA and W-shaped MESA containing honeycomb carbon filters indicated that the W-shaped MESA can be loaded with four times more carbon at 1/7 the initial resistance of single honeycomb carbon filters. The performance index of carbon loading divided by pressure drop of the filtration unit at 500 fpm was demonstrated to be improved by a factor of 25 for a WV-shaped MFM MESA compared to the single honeycomb carbon filter.

## **Chapter 8 Conclusions and Future Work**

### **8.1 Conclusions**

The studies in this dissertation demonstrate, for the first time, the use of microfibrous entrapped sorbent materials for designing pleated single filter and MESA structures as a dual-functional filtration unit which can remove both of particle and gas phase contaminants simultaneously at typical face velocity setting for residential and commercial HVAC systems. Two developed semi-empirical pressure drop models for single filter and MESA structures were utilized to predict initial pressure drops of different single MFM filters and MESA configurations. Optimization of design parameters for single pleated filters (such as filter depth, pleat count and media thickness) and for MESA structures (such as element count, element depth, pleat count) were conducted through the application of these two models. The good agreement of model simulation and experimental results on pleated filters that can only remove particles indicated that these models can be used as a design tool for any filter media to optimize pleated filters design and MESA structures design.

The effects of design parameters such as element numbers, element depth, pleat numbers, element alignment and addition of fairings on flow resistance across various MESA configurations containing particle pleated filters were investigated experimentally on the full-scale ASHRAE standard 52.2 filter test rig. Experimental results indicated that a W-shaped MESA that contains four two inch deep pleated filters is the optimal MESA design with respect

to the initial pressure drop. Since the slot resistance serves as the primary contributor to the overall initial pressure drop of MESA units, the effect of pleat numbers of each element inside MESA units on the overall initial resistance across MESA units is not as significant as that of single pleated filters. In addition, the loading manner of filter elements inside MESA units does not affect the overall initial resistance across MESA units. However, the addition of fairings on the front and back of MESA unit can help to reduce initial pressure drop by 15% compared to the same MESA unit without fairings. Energy consumption on a single pleated filter and a V-shaped MESA unit based on the experimental results were estimated and compared. The analysis demonstrated that the employment of the V-shaped MESA unit instead of two single pleated filters can result in a significant energy saving and improve the energy efficiency of HVAC systems.

Dust loading behavior was first investigated on small scale flat media samples and full size pleated filters under high velocity ranges by applying ASHRAE standard test dirt which contains polydispersed particles. It was observed that the optimal pleat count corresponding the minimal initial pressure drop does not match with the optimal pleat count corresponding to the maximal dirt loading. The face velocity was found to impact the loading coefficient in this given particle-fiber system. Variations in deposition pattern during the dust loading process were verified by analyzing SEMs of media samples at different loading stages and face velocities. In addition, an empirical pressure drop model for pleated filters during dust loading process was developed for the given test system. The agreement of model results and experimental results show the model can be used to predict the transition region for pleated filters. It is meaningful for the engineering community since the transition point marks the time



that the filter needs to be changed. Once the filter transition to depth filtration region, more energy will be consumed but the removal efficiency does not be improved significantly.

## **8.2 Recommendations for Future Work**

### **8.2.1 Lab tests and field tests of MFM filtration units**

Based on the model simulation results and comparison with the experimental results of carbon filters, single pleated MFM filter and MFM MESA units show obvious improvements on filtration performance regarding pressure drop and sorbent loading capacity. Therefore, there is a need to make some full size MFM single filters and MFM MESA units. Lab tests including initial pressure drop, removal efficiency, dust loading capacity and gas life are necessary to conduct on the constructed MFM filtration units to verify the model simulation results. Furthermore, field tests in a real environment of the optimal MFM filtration unit would be the last step for the commercialization of this new dual-functional filtration unit.

### **8.2.2 Development of comprehensive filtration system**

Composite bed design in which a thin layer of microfibrinous entrapped small sorbent particles media is placed in series with packed beds of large particles was shown to have significant advantages in terms of adsorbent utilization and breakthrough times (Kalluri, 2008). This design has successfully combined the high capacity of packed beds and the high efficiency of the MFM layer. However, particle removal is beyond the function of the composite bed design.

A comprehensive filtration system which combines the composite bed design and MESA design can be developed to achieve the simultaneous particle removal and gaseous contaminants removal at low energy consumption. Figure 8.1 illustrates the structure of this

comprehensive filtration system, which is composed of three parts, particle removal filter, packed bed and microfibrinous entrapped sorbents filter.

Filtration performance tests such as initial pressure drop test, particle removal efficiency test and hexane adsorption breakthrough test should be carried out on the constructed comprehensive filtration. The effect of design parameters (depth of particle removal filter, packed bed depth, particle size in packed bed, depth of microfibrinous entrapped sorbents filter) on filtration performance can be investigated to determine the optimal design parameters for best filtration performance. Potential application areas of the comprehensive filtration unit are cathode air filters for solid oxide fuel cells or polymer electrolyte membrane fuel cells, air filtration masks for biological or fire personal protection, and air filtration in clean room or semiconductor environment.

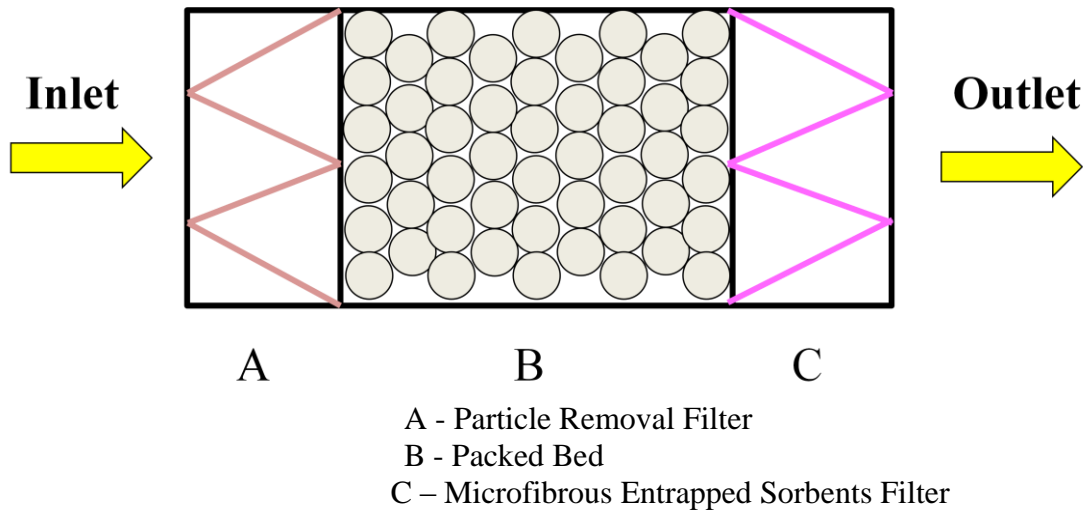


Figure 8.1 Schematic of comprehensive filtration system

### **8.2.3 CFD Analysis**

Although MFM filtration units show great benefits for removing particle and gas phase contaminants, the underlying mechanisms behind the enhanced performance of microfibrinous media are not fully understood. Computational fluid dynamics (CFD) simulations have been performed for air through microfibrinous materials entrapped activated carbon particles under the face velocities ranging between 8 fpm and 252 fpm (Duggirala et al., 2008). These simulations can provide insight into the detailed fluid mechanics as well as the global properties of microfibrinous flows. Therefore, CFD tools can be used in the high velocity filtration system for understanding the flow fields in single MFM pleated filter and MFM MESA units. Further, CFD simulations can be used for a mass transfer study aimed at improving the gas life of the single MFM pleated filter and MFM MESA filtration units.

## References

1. Abbey, D.E., Burchette, R.J., Knutsen, S.F., McDonnell, W.F., Lebowitz, M.D., Enright, P.L. (1998). Long-term particulate and other air pollutants and lung function in non-smokers. *American Journal of Respiratory Critical Care Medicine*, 158 (1), 289-298.
2. Agency for Toxic Substance and Disease Registry, Public Health Service, U.S. Department of Health and Human Services, Toxicological Profile for Formaldehyde, NTIS Accession No. PB99-166654, 1991, p. 451.
3. Álvarez-Galván, M.C., Pawelec, B., de la Peña O'Shea, V.A., Fierro, J.L.G., Arias, P.L. (2004). Formaldehyde/methanol combustion on alumina-supported manganese-palladium oxide catalyst. *Applied Catalysis B: Environmental*, 51, 83-91.
4. Arashidani, K., Yoshikawa, M., Kawamoto, T., Matsuno, K., Kayama, F., Kodama, Y. (1996). Indoor pollution from heating. *Industrial Health*, 34 (3), 205-215.
5. Armor, J. N. (1998). Important targets in environmental catalysis. *Res. Chem. Intermed.*, 24(2), 105-113.
6. Arnold, B.D, Matela, D., and Veeck, A. (2005). Life-cycle costing of air filtration. *ASHRAE Journal*, 47, 30-32.
7. ASHRAE Standard 52.1-1992. *Gravimetric and Dust Spot Procedures for Testing Air Cleaning Devices Used in General Ventilation for Removing Particulate Matter*. American Society of Heating, Refrigerating and Air-Conditioning Engineers, Inc., Atlanta, GA.
8. ASHRAE Standard 52.2-1999. *Method of Testing General Ventilation Air-Cleaning Devices for Removal Efficiency by Particle Size*. American Society of Heating, Refrigerating and Air-Conditioning Engineers, Inc., Atlanta, GA.
9. ASHRAE Standard 62-1989. *Ventilation for Acceptable Indoor Air Quality*. American Society of Heating, Refrigeration, and Air conditioning Engineers, Inc., Atlanta, GA.
10. ASHRAE Standard 62-1999. *Ventilation for Acceptable Indoor Air Quality*. American Society of Heating, Refrigerating and Air-Conditioning Engineers, Inc., Atlanta, GA, 1999, 10, 22-23.

11. ASTM Standard F 778-88. (2001). *Standard Methods of Gas Flow Resistance Testing of Filtration Media*. West Conshohocken, PA, 1-15.
12. Bergman, W., Taylor, R.D., & Miller, H.H. Biermann, A.H., Hebard, H.D., daRoza, R.A. and Lum, B.Y. (1978). Enhanced filtration program at LLNL. A progress report, 15<sup>th</sup> DOE Nuclear Air Cleaning Conference, Boston, 1058-1081.
13. Bigelow, B. 2008. Energy hogs: the scale of the nation's energy problem. American Indoor Greening Institute.
14. Brinke, J.T., Selvin, S., Hodgson, A. T., Fisk, W.J., Mendell, M.J., Koshland, C. P., and Daisey, J.M. (1998). Development of new volatile organic compound (VOC) exposure metrics and their relationship to "sick building syndrome" symptoms. *Indoor Air*, 8, 140-152.
15. Brooks, B.O., Utter, G.M., DeBroy, J.A., Schimke, R.D. (1991). Indoor air pollution: an edifice complex. *Clinical Toxicology*, 29(3), 315-374.
16. Brown, R.C. (1993). *Air filtration, an integrated approach to the theory and applications of fibrous filters*. Pergamon Press: Oxford.
17. Brunekreef, S., and Holgate, S.T. (2002). Air pollution and health. *The Lancet*, 360(9341), 1233-1242.
18. Bruce, N., Perez-Padilla, R., Albalak, R. (2000). Indoor air pollution in developing countries: a major environmental and public health challenge. *Bulletin of the World Health Organization*, 78 (9), 1078-1092.
19. Burge, P.S. (2004). Sick building syndrome. *Occup Environ Med*, 61,185-190.
20. Chan, C.C., Yanagisawa, Y., Spengler, J.D. (1990). Personal and indoor/outdoor nitrogen dioxide exposure assessments of 23 homes in Taiwan. *Toxicology and Industrial Health*, 6 (1), 173-182.
21. Chang, B. and Tatarchuk, B.J. (2006a) Microfibrous entrapment of small catalyst particulates for high contacting efficiency removal of trace CO from practical reformates for PEM H<sub>2</sub>-O<sub>2</sub> fuel cells. *Journal of Materials Engineering and Performances*, 15(4), 453-456.
22. Chang, B., Lu, Y. and Tatarchuk, B.J. (2006b). Microfibrous entrapment of small catalyst or sorbent particulates for high contacting-efficiency removal of trace contaminants including CO and H<sub>2</sub>S from practical reformates for PEM H<sub>2</sub>-O<sub>2</sub> fuel cells. *Chemical Engineering Journal*, 115, 195-202.
23. Centi, G., Ciambelli, P., Perathoner, S., Russo, P. (2002). Environmental catalysis: trends and outlook. *Catalysis Today*, 75, 3-15.

24. Clausen, G. (2004). Ventilation filters and indoor air quality: a review of research from the international centre for indoor environment and energy. *Indoor Air*, 14 (Suppl 7), 202-207.
25. Cohen, B.S. (1998). Deposition of charged particles on lung airways. *Health Physics*, 74 (5), 554-560.
26. Coultas, D.B., Lambert, W.E. (1991). Carbon monoxide. In: Sanet, J.M., Spengler, J.D. (Eds.), *Indoor Air Pollution: A Health Perspective*. Johns Hopkins University Press: Baltimore, pp. 187-208.
27. Craig, L., Brook, J.R., Chiotti, Q., Croes, B., Gower, S., Hedley, A., Krewski, D., et al. (2008). Air pollution and public health: a guidance document for risk managers. *Journal of Toxicology and Environmental Health, Part A*, 71(9-10), 588-698.
28. Daisey, J.M., Angell, W.J., Apte, M.G. (2003). Indoor air quality, ventilation and health symptoms in schools: an analysis of existing information. *Indoor Air*, 13(1), 53-64.
29. Davidson, C.I., Phalen, R.F., Solomon, P.A. (2005). Airborne particulate matter and human health: a review. *Aerosol Science and Technology*, 39, 737-749.
30. Davies, C.N. (1973). *Air Filtration*. Academic Press: New York.
31. Davis, W.T., Kim, G. (1999). Effects of Prefilters on the Performance of HEPA Filters. *Filtration & Separation*, 36(3), 51-56.
32. Duggirala, R.K., Roy, C.J., Saeidi, S.M., Khodadadi, J.M., Cahela, D.R., Tatarchuk, B.J. (2008). Pressured drop predictions in microfibrinous materials using computational fluid dynamics. *Journal of Fluids Engineering*, 130(7), 071302 (13 pages)
33. Ellis, W.D., and Tometz, P.V. (1972). Room-temperature catalytic decomposition of ozone. *Atmospheric Environment*, 6(10), 707-714.
34. Everaert, K., and Baeyens, J. (2004). Catalytic combustion of volatile organic compounds. *Journal of Hazardous Materials*, B109, 113-139.
35. Fisk, W.J., Faulkner, D., Palonen, Seppanen, J.O. (2002). Performance and costs of particle air filtration technologies. *Indoor Air*, 12, 223-234.
36. Garin, F. (2004). Environmental catalysis. *Catalysis Today*, 89, 255-268.
37. Graef, A., Stenhouse, J.T., Walsh, D.C. (1995). The Effect of solid aerosol on prefilter material performance. *Journal of Aerosol Science*, 26(S1), S741-S742.

38. Groes, L., Pejtersen, J., Valbjørn, O. (1996). Perceptions and symptoms as a function of indoor environmental factors and building characteristics in office buildings. In: Proceedings of the Sixth International Conference on Indoor Air Quality and Climate, Vol. 4. Nagoya, Japan, pp. 237-242.
39. Godish, T. (2001). *Indoor Environmental Quality*. Lewis Publishers: Boca Raton.
40. Gold, D.R. (1992). Indoor air pollution. *Clinics in Chest Medicine*, 13(2), 215-229.
41. Guneser, S., et al. (1994). Effects of indoor environmental factors on respiratory systems of children. *Journal of Tropical Pediatrics*, 40, 114-116.
42. Harris, D., Cahela, D., Tatarchuk, B. (2001). Wet layup and sintering of metal-containing microfibrous composites for chemical processing opportunities. *Composites Part A: Applied Science and Manufacturing*, 32(8), 1117-1126.
43. Harrison, J., Pickering, A.C., Finnegan, M.J., Austick, P.K.C. (1987). The sick building syndrome—further prevalence studies and investigations of possible causes. In: Proceedings of the Fourth International Conference on Indoor Air Quality and Climate. Institute for Water, Soil, and Air Hygiene, Berlin, pp. 487-491.
44. Hao, Z., Cheng, D., Guo, Y., Liang, Y. (2001). Supported gold catalysts used for ozone decomposition and simultaneous elimination of ozone and carbon monoxide at ambient temperature. *Applied Catalysis B: Environmental*, 33(3), 217-222.
45. Henning, K.D., and Schäfer, S. (1993). Impregnated activated carbon for environmental protection. *Gas Separation & Purification*, 7(4), 235-240.
46. Hinds, W.C. (1982). *Aerosol technology: properties, behavior, and measurement of airborne particles*. Wiley: New York.
47. Hodgson, M.J., Frohlinger, J., Permar, E., Tidwell, C., Traven, N.D., Olenchock, S.A., Karpf, M. (1991). Symptoms and micro-environmental measures in non-problem buildings. *Journal of Occupational Medicine*, 33 (4), 527-533.
48. Horvath, E.P. (1997). Building-related illness and sick building syndrome: from the specific to the vague. *Cleveland Clinical Journal of Medicine*, 64(6), 303-309.
49. Huang, H., Leung, D.Y.C. (2011). Complete elimination of indoor formaldehyde over supported Pt catalysts with extremely low Pt content at ambient temperature. *Journal of Catalysis*, 280(1), 60-67.
50. Idelchik, I.E. (1994). *Handbook of hydraulic resistance* (3<sup>rd</sup> Edition). CRC press: Boca Raton, FL.

51. IEH (Institute for Environment and Health). (1996). IEH assessment on indoor air quality in the home. Institute for Environment and Health, Leicester, UK.
52. Islam, M.S., Ulmer, W.T. (1979). Threshold concentrations of SO<sub>2</sub> for patients with oversensitivity of the bronchial system. *Wissenschaft und Umwelt, 1 (1)*, 41-47.
53. Japuntich, D.A., Stenhouse, J.I.T., & Liu, B.Y.H. (1994). Experimental results of solid monodisperse particle clogging of fibrous filters. *Journal of Aerosol Science, 25(2)*, 385-393.
54. Jones, A.P. (1999). Indoor air quality and health. *Atmospheric Environment, 33*, 4535-4564.
55. Kalluri, R.R., Cahela, D.R., and Tatarchuk, B.J. (2008). Microfibrous entrapped small particle adsorbents for high efficiency heterogeneous contacting. *Separation and Purification Technology, 62*, 304-316.
56. Kalluri, R.R., Cahela, D.R., and Tatarchuk, B.J. (2009). Comparative heterogeneous contacting efficiency in fixed bed reactors: opportunities for new microstructured systems. *Applied Catalysis B: environmental, 90*, 507-515.
57. Kalluri, R., 2008. Microfibrous entrapped catalyst and sorbents: microstructure heterogeneous contacting systems with enhanced efficiency. Doctoral Dissertation. Auburn University, Auburn, AL.
58. Kanaoka, C., & Hiragi, S. (1990). Pressure drop of air filter with dust load. *Journal of Aerosol Science, 21*, 127-137.
59. Karanjikar, M., 2005. Low temperature oxidation of carbon monoxide using microfibrous entrapped catalysts for fire escape mask application. Doctoral Dissertation. Auburn University, Auburn, AL.
60. Kennedy, D., 2007. Fuel cell cathode air filters: methodologies for design and optimization. Master Thesis. Auburn University, Auburn, AL.
61. Kjaergaard, S., Mølhave, L. and Pedersen, O.F. (1989). Human reactions to indoor air pollutants: n-decane, *Environment International, 15*, 473-482.
62. Koenig, J.Q., Larson, T.V., Hamley, Q.S., Rebolledo, V., Dumler, K., Checkoway, H., Wang, S.Z., Lin, D., Pierson, W.E. (1993). Pulmonary lung function in children associated with fine particulate matter. *Environmental Research, 63 (1)*, 26-38.
63. Lahtinen, M., Huuhtanen, P., Reijula, K. (1998). Sick building syndrome and psychosocial factors- a literature review. *Indoor Air, 8(S4)*, 71-80.



64. Lebedev, M.N., Kirsch, A.A. (1995). Pressure drop of loaded fibrous filters. *Journal of Aerosol Science*, 26 (S1), S735-S736.
65. Lee, K.W., Liu, B.Y.H. (1980). On the minimum efficiency and the most penetrating particle size for fibrous filters. *J Air Pollut Control Assoc*, 30, 377-381.
66. Lee, J., Kim, S. Liu, B.Y.H. (2001). Effect of bi-modal aerosol mass loading on the pressure drop for gas cleaning industrial filters. *Aerosol Science & Technology*, 35, 805-814.
67. Letourneau, P., Mulcey, Ph., & Vendel, J. (1990). Aerosol penetration inside HEPA filtration media. 21st DOE/NRC nuclear air cleaning conference, CONF-900813, San Diego.
68. Lin, H.K., Chiu, H.C., Tsai, H.C., Chien, S.H., and Wang, C.B. (2003). Synthesis, characterization and catalytic oxidation of carbon monoxide over cobalt oxide. *Catalysis Letters*, 88(3-4), 169-174.
69. Liotta, L.F. (2010). Catalytic oxidation of volatile organic compounds on supported noble metals. *Applied Catalysis B: Environmental*, 100, 403-412.
70. Liu, David H.F., and Lipták, Béla G. (2000). *Air Pollution*. Lewis Publishers: Boca Raton.
71. Luna, E.A. (2009). Improvement of indoor air quality through the development of polymeric microfibrinous material. Dissertation, Auburn University, Auburn, AL.
72. Maier, W.C., et al. (1997). Indoor risk factors for asthma and wheezing among Seattle school children. *Environmental Health Perspectives*, 105, 208-214.
73. Maroni, M., Seifert, B., Lindvall, T. (Eds) (1995). *Indoor Air Quality- a Comprehensive Reference Book*. Elsevier: Amsterdam.
74. Marrion, C.J., Cahela, D.R., Ahn, S., Tatarchuk, B.J. (1994). Composite fiber structures for catalysts and electrodes. *Journal of Power Sources*, 47, 297-302.
75. Mendell, M.J., Fisk, W.J., Deddens, J.A., Seavey, W.G., Smith, A.H., Smith, D.F., Hodgson, A.T., Daisey, J.M. and Goldman, L.R. (1996). Elevated symptom prevalence associated with ventilation type in office buildings. *Epidemiology*, 7(6), 583-589.
76. Miller, J.D. (2002). Defensive Filtration. *ASHRAE Journal*, 44, 18-23.
77. Morgan, K.T. (1997). A brief review of formaldehyde carcinogenesis in relation to rat nasal pathology and human health risk assessment. *Toxicologic Pathology*, 25 (3), 291-307.

78. Moriske, H.J., Drews, M., Ebert, G., Menk, G., Scheller, C., Schöndube, M., Konieczny, L. (1996). Indoor air pollution by different heating systems: coal burning, open fireplace and central heating. *Toxicology Letters*, 88 (1-3), 349-354.
79. Mølhave, L., Bach, B., Pedersen, O.F. (1986). Human reactions to low concentrations of volatile organic compounds. *Environment International*, 12 (1-4), 167-175.
80. Mølhave, L., Clausen, G., Berglund, B., De Ceaurriz, J., Kettrup, A., Lindvall, T., Maroni, M., Pickering, A. C., Risse, U., Rothweiler, H., Seifert, B. and Younes, M. (1997). Total volatile organic compounds (TVOC) in indoor air quality investigations. *Indoor Air*, 7, 225-240.
81. Murrell, L.L., Dautzenberg, F.M., Overbeek, R.A., Tatarchuk, B.J. (2000). Reactor including a mesh structure for supporting catalytic particles. EP Patent 1001844
82. Nishino, A. (1991). Household appliances using catalysis. *Catalysis Today*, 10(1), 107-118.
83. Novick, V.J., Higgins, P.J., Dierkschiede, B., Abrahamson, C., Richardson, W.B., Monson, P.R., & Ellison, P.G. (1990). Efficiency and mass loading characteristics of a typical HEPA filter media material. Proceedings of the 21st DOE/NRC *nuclear air cleaning conference*, San Diego (pp.782–798).
84. Novick, V.J., Monson, P.R., Ellison, P.E. (1992). The effect of solid particle mass loading on the pressure drop of HEPA filters. *Journal of Aerosol Science*, 23 (6), 657-665.
85. Ohtani, B., Zhang, S. W., Nishimoto, S. and Kagiya, T. (1992). Catalytic and photocatalytic decomposition of ozone at room temperature over titanium (IV) oxide. *Journal of Chemical Society, Faraday Transactions*, 88, 1049-1053.
86. Parson, R.A. (1991). ASHRAE Handbook: HVAC Applications. American Society of Heating, Refrigerating and Air-Conditioning Engineers, Inc., Atlanta, GA, 1991.
87. Payatakes, A.C., & Okuyama, K. (1982). Effects of aerosol particle deposition on the dynamic behavior of uniform or multilayer fibrous filter. *Journal of Colloid and Interface Science*, 88(1), 55–78.
88. Polpong, P., Bovornkitti, S. (1998). Indoor Radon. *Journal of the Medical Association of Thailand*, 81 (1), 47-57.
89. Qin, Y.H., Zhang, X.M., Jin, H.Z., Liu, Y.Q., Fan, D.L., Cao, Z.J. (1993). Effects of indoor air pollution on respiratory illness of school children. In: Jantunen, M., Kalliokoski, P., Kukkonen, E., Saarela, K., SeppäKnen, A., Vuorelma, H. (Eds.), Proceedings of the Sixth International Conference on Indoor Air Quality and Climate. Helsinki, Finland, pp. 477-482.

90. Queen, A.P. (2005). High efficiency adsorption filter via packed bed and polishing sorbent architectures for regenerable collective protection equipment. Masters Thesis. Auburn University, Auburn, AL.
91. Redlich, C.A., Sparer, J., Cullen, M.R. (1997). Sick-building syndrome. *Lancet*, 349, 1013-1016.
92. Ritz, B., Yu, F. (1999). The effect of ambient carbon monoxide on low birth weight among children born in southern California between 1989 and 1993. *Environmental Health Perspectives*, 107, 17-25.
93. Robinson, T.J., and Ouellet, A.E. (1999). Filters and filtration. *ASHRAE Journal*, 41, 65-70.
94. Rong, H., Liu, Z., Wu, Q., Pan, D., Zheng, J. (2010). Formaldehyde removal by Rayon-based activated carbon fibers modified by *P*-aminobenzoic acid. *Cellulose*, 17, 205-214.
95. Rong, H., Ryn, Z., Zheng, J., Zhang, Y. (2002). Effect of air oxidation of Rayon-based activated carbon fibers on the adsorption behavior for formaldehyde. *Carbon*, 40, 2291-2300.
96. Sandmeyer, E.E. (1982). Aromatic hydrocarbons. In: Clayton, G.D., Clayton, F.E. (Eds.), *Patty's Industrial Hygiene and Toxicology*, Vol. 2, 3rd Edition. Wiley, New York, pp. 3253-3431.
97. Schwarzberg, M.N. (1993). Carbon dioxide level as migraine threshold factor: hypothesis and possible solutions. *Medical Hypotheses*, 41 (1), 35-36.
98. Seigneur, C. (2005). Air Pollution: current challenges and future opportunities. *AIChE Journal*, 51 (2), 356-364.
99. Sekine, Y., Nishimura, A. (2001). Removal of formaldehyde from indoor air by passive type air-cleaning materials. *Atmospheric Environment*, 35, 2001-2007.
100. Sekine, Y. (2002). Oxidative decomposition of formaldehyde by metal oxides at room temperature. *Atmospheric Environment*, 36, 5543-5547.
101. Seppänen, O.A., Fisk, W.J., and Mendell, M.J. (1999). Association of ventilation rates and CO<sub>2</sub> concentrations with health and other responses in commercial and institutional buildings. *Indoor Air*, 9, 226-252.
102. Sonawane, R.S. and Dongare, M.K. (2006). Sol-gel synthesis of Au/TiO<sub>2</sub> thin films for photocatalytic degradation of phenol in sunlight. *Journal of Molecular Catalysis A: Chemical*, 243, 68-76.

103. Sonawane, R.S., Kale, B.B., and Dongare, M.K. (2004). Preparation and photo-catalytic activity of Fe-TiO<sub>2</sub> thin films prepared by sol-gel dip coating. *Materials Chemistry and Physics*, 85, 52-57.
104. Song, C.B., Park, H.S., and Lee, K.W. (2006). Experimental study of filter clogging with monodisperse PSL Particles. *Powder Technology*, 163,152-159.
105. Sothen, R.A., and Tatarchuk, B.J. (2008). A semi-empirical pressure drop model: Part I-pleated filters. *HVAC & R Research*, 14(6), 841-860.
106. Sothen, R.A, and Tatarchuk, B.J. (2009). A semi-empirical pressure drop model: Part II-Multi-element Pleated Filter Banks. *HVAC&R Research*, 15(2), 269–85.
107. Sothen, R.A. (2009). Novel packaging designs for improvements in air filter performance. Dissertation, Auburn University, Auburn, AL.
108. Spengler, J.D. (1993). Nitrogen dioxide and respiratory illnesses in infants. *American Review of Respiratory Disorders*, 148 (5), 1258-1265.
109. Spengler, J.D., Samet, J.M., and McCarthy, J.F. (2000). *Indoor Air Quality Handbook*. Chapter 31. Volatile organic compounds, Tucker W.G. (p.31.1-31.20), McGraw Hill: New York.
110. Stenhouse, J.I.T., Trottier, R. (1991). The Loading of fibrous filters with submicron particles. *Journal of Aerosol Science*, 22 (S1), S777-S780.
111. Subrahmanyam, C., Bulushev, D. A., Kiwi-Minsker, L. (2005). Dynamic behavior of activated carbon catalysts during ozone decomposition at room temperature. *Applied Catalysis B: Environmental*, 61(1-2), 98-106.
112. Sundell, J. (2004). On the history of indoor air quality and health. *Indoor air*, 14(S7), 51-58.
113. Thomas, D., Contal, P., Renaudin, V., Penicot, P., Leclerc, D., Vendel, J. (1999). Modelling pressure drop in HEPA filters during dynamic filtration. *Journal of Aerosol Science*, 30 (2), 235-246.
114. Thomas, D., Penicot, P., Contal, P., Leclerc, D., Vendel, J. (2001). Clogging of fibrous filters by solid aerosol particles experimental and modeling study. *Chemical Engineering Science*, 56, 3549-3561.
115. United States Environmental Protection Agency (1993). National Air Quality and Emissions Trends Report, 1992, EPA/454/R-93/031 (Office of Air and Radiation, Office of Air Quality Planning and Standards, USEPA, Research Triangle Park, NC, October 1993).

116. United States Environmental Protection Agency (1995). Characterizing Air Emissions from Indoor Sources, EPA report: EPA/600/F-95/005.
117. United States Environmental Protection Agency (1996). Radon: is your family at risk? Environmental Protection Agency, Washington, DC.
118. United States Environmental Protection Agency (1997). Revisions to the National Ambient Air Quality Standards for Particles Matter. Federal Register, July 18 1997, 62: 38651-38701.
119. United States Environmental Protection Agency (1998). Zeolite- a versatile air pollutant adsorber. Research Triangle Park, NC: U.S. Environmental Protection Agency, p.10.
120. United States Environmental Protection Agency (1999). Choosing an adsorption system for VOC: carbon, zeolite, or polymers? Research Triangle Park, NC: U.S. Environmental Protection Agency, p.24.
121. United States Environmental Protection Agency (2004a). Air Quality Criteria for Particulate Matter. Fourth External Review Draft, EPA Report, EPA/600/P-99/002., Office of Research and Development, Research Triangle Park, NC.
122. United States Environmental Protection Agency (2004b). Part II, Environmental Protection Agency, 40 CFR Part 50, National Ambient Air Quality Standards for Particles Matter; Final Rule. In Federal Register, 62 (138), July 18, 1997, 40 CFR 50. Available at <http://www.epa.gov/ttnamti/files/cfr/recent/pmnaaqs.pdf>
123. United States Environmental Protection Agency (2010a). Part III, Environmental Protection Agency, 40 CFR Parts 50 and 58, Primary National Ambient Air Quality Standards for Nitrogen Dioxide; Final Rule. Federal Register, Feb 9, 2010, 75(26):6474-6537.
124. United States Environmental Protection Agency (2010b). Part II, Environmental Protection Agency, 40 CFR Parts 50, 53, and 58, Primary National Ambient Air Quality Standards for Sulfur Dioxide; Final Rule. Federal Register, June 22, 2010, 75(119):35520-35603.
125. U.S. Energy Information Administration website, ([www.eia.doe.gov/cneaf/electricity/epm/table56a.html](http://www.eia.doe.gov/cneaf/electricity/epm/table56a.html), accessed on 3/22/2011)
126. Valmari, T., Lehtimaki, M. Taiple, A. (2006). Filter clogging by bimodal aerosol. *Aerosol Science & Technology*, 40, 255-260.
127. Vaughan, T.L., Strader, C., Davis, S., Daling, J.R. (1986). Formaldehyde and cancers of the pharynx, sinus, and nasal cavity: II. Residential exposures. *International Journal of Cancer*, 38(5), 685-688.

128. Vendel, J., Letourneau, P., & Renaudin, V. (1992). Effects of the particle penetration inside the filter medium on the HEPA filter pressure drop. Proceedings of the 22nd DOE/NRC nuclear air cleaning conference, CONF-920823, Denvers.
129. Vincent, D., Annesi, I., Festy, B., Lambrozo, J. (1997). Ventilation system, indoor air quality, and health outcomes in Parisian modern office workers. *Environmental Research*, 75 (2), 100-112.
130. Visco, A. M., Donato, A., Milone, C., and Galvagno, S. (1997). Catalytic oxidation of carbon monoxide over Au/Fe<sub>2</sub>O<sub>3</sub> preparations. *Reaction Kinetics and Catalysis Letters*, 61(2), 219-226.
131. Wallace, L.A. (1997). Sick building syndrome. In: Bardana, E.J., Montanaro, A. (Eds.), *Indoor Air Pollution and Health*. Marcel Dekker: New York, pp. 81-103.
132. Wang, L., Sakurai, M., Kameyama, H. (2009). Study of catalytic decomposition of formaldehyde on Pt/TiO<sub>2</sub> alumite catalyst as ambient temperature. *Journal of Hazardous Materials*, 167, 399-405.
133. Weschler, C.J. (2000). Ozone in indoor environments: concentrations and chemistry. *Indoor Air*, 10(4), 269-288.
134. Weschler, C.J. (2001). Reactions among indoor air pollutants. *Sci World*, 1, 443-457.
135. Weschler, C.J. (2004). Chemical reactions among indoor pollutants: what we've learned in the new millennium. *Indoor Air*, 14(Supplement 7), 184-201.
136. Zhang, C., He, H., Tanaka, K. (2005). Perfect catalytic oxidation of formaldehyde over a Pt/TiO<sub>2</sub> catalyst at room temperature. *Catalysis Communications*, 6, 211-214.
137. Zhang, C., He, H., Tanaka, K. (2006). Catalytic performance and mechanism of a Pt/TiO<sub>2</sub> catalyst for the oxidation of formaldehyde at room temperature. *Applied Catalysis B: Environmental*, 65, 37-43.
138. Zhang, C. and He, H. (2007). A comparative study of TiO<sub>2</sub> supported noble metal catalysts for the oxidation of formaldehyde at room temperature. *Catalysis Today*, 126, 345-350.
139. Zhang, J., Jin, Y., Li, C., Shen, Y., Han, L., Hu, Z., Di, X., Liu, Z. (2009). Creation of three-dimensionally ordered macroporous Au/CeO<sub>2</sub> catalysts with controlled pore sizes and their enhanced catalytic performance for formaldehyde oxidation. *Applied Catalysis B: Environmental*, 91, 11-20.
140. Zhang, J. and Smith, K.R. (2003). Indoor air pollution: a global health concern. *British Medical Bulletin*, 68(1), 209-225.

141. Zhang, Y. (2005). *Indoor Air Quality Engineering*. CRC Press: Boca Raton.
142. Zweers, T., Preller, L., Brunekreef, B., and Boleij, J.S.M. (1992). Health and indoor climate complaints of 7043 office workers in 61 buildings in the Netherlands. *Indoor Air*, 2, 127-136.